Title

Investigation of Ultrafast Photothermal Surface Expansion and Diffusivity in GaAs via Laser-Induced Dynamic Gratings

Author

Pennington, D.M.

Publication Date

1992-04-01

LBL-32383
UC-401

Lawrence Berkeley Laboratory
UNIVERSITY OF CALIFORNIA

CHEMICAL SCIENCES DIVISION

Investigation of Ultrafast Photothermal Surface Expansion and Diffusivity in GaAs via Laser-Induced Dynamic Gratings

D.M. Pennington
(Ph.D. Thesis)

April 1992

Prepared for the U.S. Department of Energy under Contract Number DE-AC03-76SF00098

LBL-32383

Investigation of Ultrafast Photothermal Surface Expansion and Diffusivity in GaAs via Laser-Induced Dynamic Gratings

by

Deanna Marie Pennington

Ph.D. Thesis

Department of Chemistry
University of California

and

Chemical Sciences Division
Lawrence Berkeley Laboratory
University of California
Berkeley, CA 94720

April, 1992

This work was supported by the Director, Office of Energy Research, Office of Basic Energy Sciences, Chemical Sciences Division of the U. S. Department of Energy, under Contract No. DE-AC03-76SF00098.

Investigation of Ultrafast Photothermal Surface Expansion and Diffusivity in GaAs via Laser-Induced Dynamic Gratings

by

Deanna Marie Pennington

Investigation of Ultrafast Photothermal Surface Expansion and Diffusivity in GaAs via Laser-Induced Dynamic Gratings

by

Deanna Marie Pennington

ABSTRACT

This thesis details the first direct ultrafast measurements of the dynamic thermal expansion of a surface and the temperature dependent surface thermal diffusivity using a two-color reflection transient grating technique. Studies were performed on p-type, n-type, and undoped GaAs(100) samples over a wide range of temperatures. By utilizing a 90 fs ultraviolet probe with visible excitation beams, the effects of interband saturation and carrier dynamics become negligible; thus lattice expansion due to heating and subsequent contraction caused by cooling provided the dominant influence on the probe. At room temperature a rise due to thermal expansion was observed, corresponding to a maximum net displacement of ≈ 1 Å at 32 ps. The diffracted signal was composed of two components, thermal expansion of the surface and heat flow away from the surface, thus allowing a determination of the rate of expansion as well as the surface thermal diffusivity, D_S. By varying the fringe spacing of the grating, this technique has the potential to separate the signal contributions to the expansion of the lattice in the perpendicular and parallel directions. In the data presented here a large fringe spacing was used, thus the dominant contribution to the rising edge of the signal was expansion perpendicular to the surface. Comparison of the results with a straightforward thermal model yields good agreement over a range of temperatures (20-300 °K). Values for D_S in GaAs were measured and found to be in reasonable agreement with bulk values above 50 °K. Below 50 °K, D_S was determined to be up to an order of magnitude slower than the bulk diffusivity due to increased phonon boundary scattering. The applicability and

advantages of the TG technique for studying photothermal and photoacoustic phenomena are discussed.

Dedicated to my parents,

who never once doubted my ability to do anything

TABLE OF CONTENTS

LIST OF FIGURES

LIST OF TABLES

ACKNOWLEDGMENTS

I would like to thank the friends, colleagues, and family members who have made this work possible. In particular, I thank my advisor Professor Charles B. Harris, who had enough confidence in my abilities to give me independence in the laboratory. He provided the ideal environment to develop my self-confidence and scientific maturity. My thanks also to Professors Raymond Chiao and A. Paul Alivisatos for reading and commenting on this thesis. And special thanks to the Harris group members, who were always willing to discuss problems and new ideas, or to lend a hand when needed. I couldn't have asked for a better group of people to work with.

My thanks to my family for putting up with this perennial student. In particular to my father for his love and unwavering faith in me. But above all to my husband, Christopher David Marshall. I would never have pursued my Ph.D. without his constant encouragement and belief in me. From our animated scientific debates, to a spare pair of hands in the lab when I needed them, he has always been there for me. Our interaction both scientifically and personally has been my guiding light. I especially appreciated his patience in assisting me with the computer codes in the Appendix, which include a portion of his transient grating diffraction code.

My thanks also to the members of the Laser Program at Lawrence Livermore National Laboratory who supported me personally, scientifically, and financially during the pursuit of my degree (DOE Contract No. W-7405-Eng-48 and an Institutional Research and Development Award from the Director's Office at LLNL). This work was also supported by a grant from the Office of Naval Research. In addition, much of the specialized equipment used in these experiments was provided by the U. S. Dept. of Energy, Office of Basic Energy Sciences, Chemical Sciences Division under Contract No. DE-AC03-76SF00098.

CURRICULUM VITAE

DEANNA M. PFNNINGTON

EDUCATION

Ph.D., Chemical Physics, University of California, Berkeley, CA, May, 1992

M.S., Physics, kensselaer Polytechnic Institute, Troy, N. Y., December, 1984

B.S., Physics, University of California, Davis, CA, June, 1981

EXPERIENCE

Physicist, Inertial Confinement Fusion Group, Laser Program, Lawrence Livermore National Laboratory, Livermore, CA, 5/85-present

Research/Teaching Assistant, Dept. of Chemistry, University of California, Berkeley, CA, 8/87- 5/92

Research/Teaching Assistant, Rensselaer Polytechnic Institute, Troy, NY, 8/83-5/85

Chemist, Health Research, Inc., Albany, NY, 2/82-4/83

Research Fellow, Crocker Nuclear Laboratory, Davis CA, 8/80-12/80

Biochemical Research Assistant, Syntex Corporation, Palo Alto, CA 4/79-7/79

AWARDS

Institutional Research and Development Grant, Lawrence Livermore National Laboratory, 1988

Associated Western Universities Fellowship, 1980

Society of Sigma Xi, 1992

PROFESSIONAL MEMBERSHIPS

American Physical Society

Optical Society of America

GENERAL RESEARCH INTERESTS

Applied Physics, Nonlinear Optical Phenomena and Spectroscopy, Laser Science

PERSONAL

Citizenship: U.S.

Spouse: Christopher D. Marshall

PUBLICATIONS AND OTHER PAPERS

18. "Dynamics of photothermal surface expansion using laser-induced holographic gratings", D. M. Pennington and C. B. Harris, Submitted to IEEE J. Quantum Electron., February, 1992.

17. "Direct measurement of the thermal expansion of a surface using transient gratings", D. M. Pennington and C. B. Harris, Submitted to Opt. Lett., January, 1992.

16. "Ultrafast measurement of the thermal expansion of a GaAs surface, D. M. Pennington and C. B. Harris, *Technical Digest* (Annual Meeting of the Optical Society of America, San Jose, CA, 1991) paper ThDD2.

15. "Diffraction properties of laser speckle generated by stimulated rotational Raman scattering in long air paths", M. A. Henesian and D. M. Pennington, in *Selected Papers on High Power Lasers*, SPIE Milestone Series, Vol. MS43, ed. by John M. Soures (SPIE, Bellingham, MA, 1991)

14. "Indices governing optical self-focusing and self-induced changes in the state of polarization in N_2, O_2, H_2, and Ar gases", R. W. Hellwarth, D. M. Pennington, and M. A. Henesian, Phys. Rev. A **41**, 2766 (1990).

13. "The nonlinear index of air at 1.053 mm", D. M. Pennington, M. A. Henesian, and R. W. Hellwarth, Phys. Rev. A **39**, 3003 (1989).

12. "Ultrafast dynamics of laser-surface interactions", D. M. Pennington and C. B. Harris, *Institutional Research and Development Annual Report* (Lawrence Livermore National Laboratory, Livermore CA, UCRL-53689-89, 1990) pg. 164.

11. "Stimulated rotational Raman scattering in long air paths", M. A. Henesian and D. M. Pennington, *Laser Program Annual Report-1987* (Lawrence Livermore National Laboratory, Livermore, CA, UCRL-50021-87, 1988) sec.3.2.8.9.

10. "Time-dependent behavior of stimulated rotational Raman scattering in air", D. M. Pennington, M. A. Henesian, and R. J. Hawkins, *Technical Digest* (Annual Meeting of the Optical Society of America, Santa Clara, CA, 1988) paper TUS2.

9. "Observation of anomalous low J-value Stokes and anti-Stokes lines in stimulated rotational Raman scattering over long air paths", D. M. Pennington and M. A. Henesian, *Technical Digest, Conference on Lasers and Electro-Optics* (Optical Society of America, Anaheim, CA, 1988) paper WN2.

8. "Observation of parametric gain suppression in stimulated rotational Raman scattering over long air paths", M. A. Henesian and D. M. Pennington, *Technical Digest, Conference on Lasers and Electro-Optics* (Optical Society of America, Anaheim, CA, 1988) paper WN1.

7. "Diffraction properties of laser speckle generated by stimulated rotational Raman scattering in long air paths", M. A. Henesian and D. M. Pennington, Invited talk, Proc Soc. Photo-Opt. Instrum. Eng. **874**, 1 (1988).

6. "Nonlinear refractive index measurements of air and argon gases at 1 atm", D. M. Pennington, M. A. Henesian, R. W. Hellwarth, and C. D. Swift, *Technical Digest*, (Annual Meeting of the Optical Society of America, Rochester, NY, 1987) pg. 28.

5. "Stimulated rotational Raman scattering experiments using the LLNL Nova laser", D. M. Pennington, C. D. Swift, M. A. Henesian, and J. R. Murray, *Technical Digest; Conference on Lasers and Electro-Optics* (Optical Society of America, Baltimore, MD, 1987) paper WM4.

4. "Measurements of stimulated rotational Raman scattering in air", D. M. Pennington, C. D. Swift, M. A. Henesian, and J. R. Murray, *Laser Program Annual Report- 1986* (Lawrence Livermore National Laboratory, Livermore, CA, UCRL-50021-86, 1987) sec.4.3.9.

3. "Measurement of the nonlinear refractive index coefficient, n_2, of air and argon", M. A. Henesian, D. M. Pennington, C. D. Swift, and R. W. Hellwarth, *Laser Program Annual Report- 1986* (Lawrence Livermore National Laboratory, Livermore, CA, UCRL-50021-86, 1987) sec. 4.3.8.

2. **"Laser Diagnostics"**, J. Richards, D. M. Pennington, C. Thompson, and P. J. Wegner, *Laser Program Annual Report- 1986* (Lawrence Livermore National Laboratory, Livermore, CA, UCRL-50021-86, 1987) sec. 3.5.2.1.

1. **"The effect of molecular adsorbates on second harmonic generation at a silver surface"**, D. M. Templeton (Pennington), Master's Thesis, Rensselaer Polytechnic Institute, Troy, NY, 1984.

GENERAL INTRODUCTION

Surfaces play an important role in a large range of phenomena, extending from the catalysis of chemical reactions to the most complex life functions. A considerable amount of effort has been devoted to the study of these phenomena, spanning the fields of both science and technology. Progress in our understanding of the many fundamental processes is slow, however, and our knowledge of interfaces is far less extensive than of the bulk. This is due in large part to the fact that the physical and chemical processes at the surface are inherently more difficult to study. Consider for example a single crystal medium. The bulk, which consists of those regions of the crystal sufficiently removed from the surface so as not to be affected by it, may be treated as a uniform, infinite periodic structure. As such, the bulk is readily amenable to theoretical treatment. At the surface, however, the forces acting on the atoms are no longer symmetric. The surface atoms are usually displaced from their ideal lattice positions, giving rise to a rather complex two-dimensional structure. Moreover, the fact that the surface constitutes an abrupt termination of the crystal results in the deformation of the crystal potential; thus its periodic nature is lost at the surface. This has far reaching consequences on the electronic properties in the region of the crystal close to the surface. At the same time, the unsaturated bonds of the surface atoms make them highly reactive towards the various species outside the crystal. Thus, except when produced and maintained in ultrahigh vacuum, the surface is covered by one or more layers of foreign matter. All of these characteristics make the surface a totally different entity from the bulk, requiring a high degree of sophistication for its study.

It has become common to distinguish between two types of surfaces, real and clean. The former refers to surfaces obtained by ordinary laboratory procedures, the latter to surfaces prepared under carefully controlled conditions so as to ensure the absence of foreign matter. A real surface is usually prepared by mechanical polishing

followed by chemical etching to remove the outer damaged layers. Such a surface is covered by a chemisorbed material, generally an oxide, and by molecules adsorbed from the surrounding environment. Real surfaces have been studied extensively because they are easily prepared and handled and because they are readily amenable to many types of measurements. Also, it is the real surface that is encountered in most practical applications. Clean surfaces are much more difficult to produce. They can be prepared by cleavage, ion bombardment, or by heating at elevated temperatures. Once obtained, a clean surface must be maintained in ultra-high vacuum (UHV), typically 10^{-9} to 10^{-12} torr, to prevent recontamination. Surfaces produced in this manner are generally free of foreign adsorbed matter to better than a few percent of an atomic monolayer. The interest in clean surfaces stems from the fact that they constitute the closest approximation to the true crystal surface, and thus should exhibit the fundamental features of the surface. Also, the clean surface, with its absence of impurities, is a much more tractable system to model theoretically.

Surfaces are studied by a wide variety of methods. Structural parameters, such as the lattice constant and long range surface ordering, can be determined by low energy electron diffraction (LEED) or X-ray scattering methods, among others. In LEED a beam of monoenergetic electrons (20-500 meV) is directed at the surface in UHV, and a diffraction pattern is produced. The geometry of the diffraction pattern is determined by the translational symmetry and periodicity of the surface only (penetration depth typically < 1 nm) so the size and shape of the surface unit cell can be deduced by simple arguments. The high atomic cross sections for electrons in this energy range makes LEED extremely sensitive to surface atomic arrangements. Surface composition can be determined by Auger electron spectroscopy (AES) or thermal desorption spectroscopy. In AES, surface atoms are ionized by incident electrons of energies ranging from 500 to 5000 eV. The ion may then lose some of it's excess potential energy by filling the core hole with an electron from a shallower level and emitting another shallower bound

electron. The energies of the emitted electrons are characteristic of the atom from which they originate, so their detection outside the sample provides a surface-sensitive probe of chemical composition. Another spectroscopic technique is photoelectron spectroscopy, in which the surface is exposed to photons of sufficient energy to ionize an electronic shell so that an electron is ejected into the vacuum. The emission energies are characteristic of the surface atoms, and the angular dependence provides information about the surface structure.

The above techniques, along with other methods such as electron microscopy, are mainly used to study the static properties of surfaces. A knowledge of the dynamics of particles is also important in the analysis of processes taking place at the surface (e.g., adsorption of particles), and also for the determination of surface properties (e.g., thermodynamic functions). The dynamic behavior of a surface is most commonly studied by optical methods. Raman and Brillouin scattering of light by dense media were first demonstrated in the 1920s and 1930s. Here the inelastically back scattered light provided information on the vibrational properties of surfaces. The more recent application of lasers to surface studies has opened up a new area of research in surface science. Laser annealing, for example, has aroused a great deal of interest for both scientific and technical reasons.[1] Lasers have been used to probe molecule-surface interactions by detecting and analyzing molecules desorbed or scattered from surfaces,[2,3] and to yield vibrational spectra of adsorbed molecules by laser-desorption[4] or to perform photoacoustic spectroscopy[5]. By monitoring the propagation of surface acoustic waves, the thickness of a surface adsorbate layer can be determined.[6] Also, by combining laser pump-probe spectroscopy with photoelectron spectroscopy, the lifetimes of electronic surface states can be measured.[7,8]

Nonlinear optical effects, such as second harmonic generation, have also been exploited for surface studies. Unlike conventional surface probes which rely on emission, absorption, or scattering of particles, nonlinear optical techniques are

applicable to interfaces between two dense media and therefore offer some unique and intriguing possibilities. In particular, this thesis discusses the use of the reflection transient grating technique to measure the rate of transient thermal expansion and the thermal diffusivity of a surface.

Two categories of recent research activities in the investigation of surfaces are apparent. One involves the study of the lattice structure or mechanics of the surface, while the other involves the various electronic phenomena taking place at and near the surface. Combined, these lead to the "chemistry" of a surface. Considerable progress has been achieved within each category, but a systematic correlation between the two types of observations remains somewhat fragmentary. While this thesis is concerned with demonstrating the ability of femtosecond optical techniques to study the dynamic mechanical properties of the surface, the transient grating technique has also proven useful in the study of electronic properties. Thus this technique has the ability to help bridge the gap between these two complex fields.

1. ULTRAFAST SURFACE EXPANSION AND THERMAL DIFFUSIVITY

1.1 Introduction

Understanding the dynamics of the basic processes associated with the interaction of ultrafast ($\leq$ 10 ps) laser pulses with matter is of great importance to optical damage investigations, opto-electronics, and laser processing of materials. The goal of our research is to gain a basic understanding of the ultrafast response of a condensed phase surface to light. The response of a solid medium to light can be separated into two categories:

1) The electronic response, which generally occurs in less than a few picoseconds.

2) The thermomechanical response of the lattice to the ultrafast deposition of heat and the stress and strain derived from the electronic relaxation, which occurs from picosecond to second time scales.

The interaction of laser radiation with matter is an extensively studied field, in particular, the response of a medium to the impulsive deposition of heat.[9,10] The short penetration depth of laser light into absorbing materials results in extremely high surface temperatures with low energy requirements. Also, due to the focusing characteristics of laser light, localized heating of specific areas of the sample is achievable with relative ease. There are several additional advantages to heating with ultrafast laser pulses, i.e. when the laser pulse duration approaches the characteristic times for relaxation of the photoexcited electron gas to the lattice. First, the heat is being deposited in such a short time that heat conduction out of the light-absorbing volume does not occur within the laser pulse duration. Extremely high temperatures are thus generated in a shallow layer. Second, due to short excitation times, matter is being heated while still in a quiescent

state and may be observed and probed before it escapes out of the irradiated area by evaporation or ablation.

Systematic investigations of the nonequilibrium thermodynamic properties measured during ultrafast irradiation are not currently available, however a number of experiments have demonstrated the importance of this field. Several studies have investigated the nonequilibrium heating of a solid that results when the deposition time is shorter than the time required to transfer the heat from the electrons to the lattice.[11,12] A necessary consequence of the deposition of heat is thermal expansion of the surface and the simultaneous propagation of acoustic waves throughout the lattice. The generation and propagation of acoustic waves has also been well studied over the past few years.[6,13] There is little published, however, on dynamic thermal expansion at the surface of a material.

Understanding the dynamics of transient thermal expansion is of technological importance in fields such as heteroepitaxial semiconductor structures, optical coating design, and laser processing of materials. For example, the biaxial stress due to different rates of thermal expansion between two semiconductor layers (e.g. GaAs/Si) can alter the band structure of the materials, leading to a change in energy relaxation rates. Furthermore, the lattice mismatch between the layers can generate dislocations that shorten carrier lifetime and influence carrier relaxation processes. Recently, the transient expansion of a heated surface was indirectly observed using picosecond photothermal deflection spectroscopy. There the thermal expansion of an absorbing silicon surface was measured by time resolving the surface deformation after a short heating pulse.[14] This technique measured the expansion perpendicular to the surface only. Using a two-color transient grating technique in the reflection grating geometry, we have directly observed the expansion perpendicular to the surface. However, while photothermal deflection spectroscopy can only measure expansion perpendicular to the surface, the transient grating method has the potential for measurement of expansion both in and out

of the plane of the surface. This requires that the thermal diffusivity of the material be long relative to the rate of expansion in order to isolate the two signal components. The transient grating technique also allows simultaneous determination of the surface thermal diffusivity. The dissipation of thermal energy at a surface is relevant to two major problems in chemistry at surfaces, adsorption and chemical reactions, in that the back reaction is quenched by the dissipation of heat.

This thesis describes in detail the use of a two-color reflection transient grating method to measure the ultrafast thermal expansion rate and thermal diffusivity of a GaAs(100) surface. As a direct band gap semiconductor, GaAs lends itself to optical investigation. In addition, since GaAs is a typical III-V semiconductor, we expect that any understanding of this material will be applicable to a wide range of materials. The ultrafast electronic response of GaAs has been extensively studied due to its technological importance in microelectronics. The transient thermomechanical response of the system, however, has been explored to a much lesser extent. We have therefore concentrated our investigations on the thermomechanical response of the GaAs(100) surface.

1.2 Transient Grating Spectroscopy

When two intense light waves are crossed at an angle in a material, its optical properties (i.e. refractive index and coefficient of absorption) become spatially modulated in the interference region as shown in Fig. 1.1. Permanent gratings have been produced in this way by photographic processes for many years.[15,16] In contrast, dynamic, or transient, gratings disappear after the light source has been switched off. Lasers are ideally suited as a light source as their coherence, collimation, and intensity provide strong interference patterns. Also their wavelength tunability and short-pulse capability allow a particular type of laser-matter interaction to be selectively addressed. Transient gratings have been induced in all material phases and in many materials, and are detected by diffraction of a third beam (probe) off the grating, or by the self-diffraction of the light waves inducing the grating. The process is equivalent to four-wave mixing in nonlinear optics, and is the basis of real time holography and optical phase conjugation.

In general, transient grating signals result from any changes in the real or imaginary parts of the index of refraction caused by the presence of the grating excitation beams. For example, the absorption of light causes excited states in a medium. These excited states are created with the same spatial distribution as the induced grating, thus creating a population density grating. In the case of an excited state population grating, a scattered signal can be generated by the index change resulting from the ground state depletion and relaxation of excited carriers throughout the material. Following decay of the initially prepared excited states, various lower energy electronic and vibrational states are populated, forming secondary gratings. Finally the excitations thermalize, forming a temperature grating which is accompanied by stress, strain, and density variations with the periodicity of the original induced grating. The probe diffracts off the optically

Figure 1.1: Interference of two light waves of wavelength λ_{exc} and wave vectors k'_{exc} and k''_{exc} at an angle θ produces a transient grating with a periodic fringe spacing $f = \lambda_{exc}/2 \sin(\theta/2)$. This creates a spatial modulation of the dielectric constant ε of the material, which varies as a function of the grating periodicity, as well as the absorption depth into the sample.

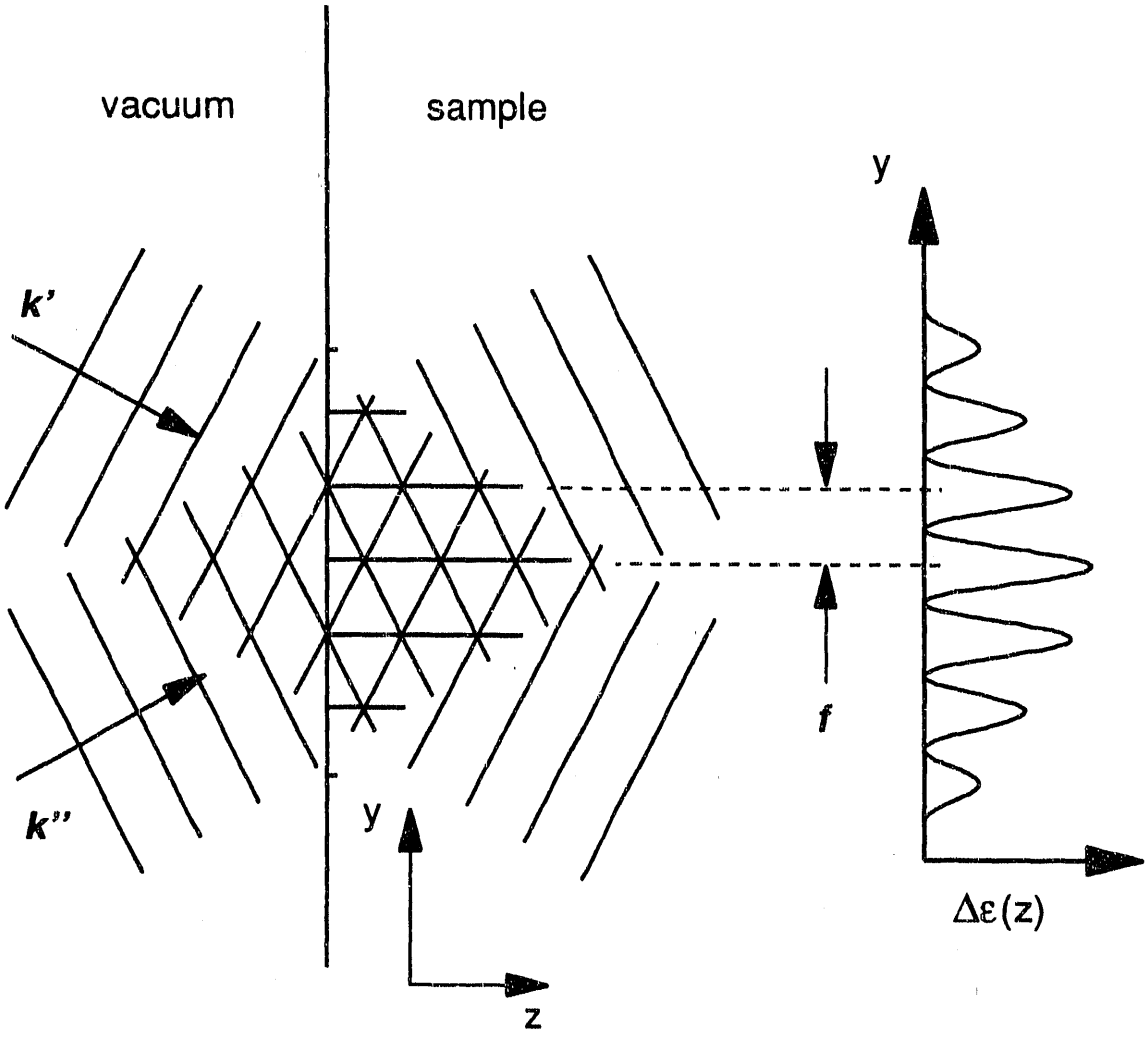
vacuum
sample
y
k'
k''
f
y
z
Δε(z)

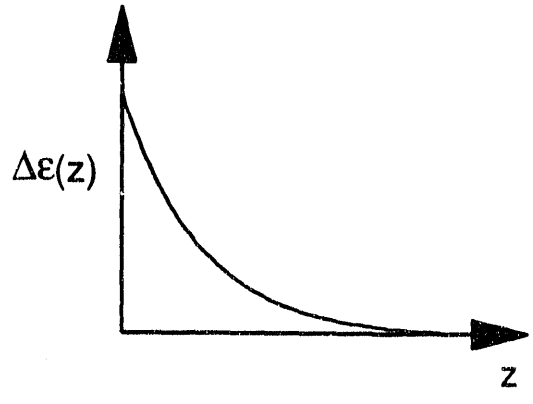
Δε(z)
z

induced density modulations, producing a signal which reflects their magnitude and time dependence.

There are many reasons for the usefulness and sensitivity of the transient grating (TG) technique:

1) Because the transient grating technique creates variations in the macroscopic properties of a material by strong coherent excitation, the resulting signal is orders of magnitude larger than for spontaneous light scattering experiments.

2) Spatially modulated excitations can be detected optically with greater sensitivity than spatially homogeneous modulations. In fact, transport phenomena such as diffusion require a modulated excitation in order to be detectable at all. The sinusoidal modulation of the refractive index created by the grating is well-defined, and is thus easier to evaluate. In addition, one can distinguish properties along different axes in an anisotropic material by varying the periodicity of the sinusoidal modulation in a controlled manner.

3) The diffracted signal is produced at a uniquely defined direction, making the technique background-free. This enables one to look at perturbations that range from one part in 10^2 to 10^{16} in magnitude.

4) Monitoring the decay of the grating allows one to distinguish between different decay mechanisms, based on the time scales of the processes responsible for the signal.

For many years transient gratings have been used to study a variety of ultrafast processes in condensed phase materials.[17] The first dynamic grating was produced not by light, but by ultrasonic waves, and was detected by the diffraction of an optical probe.[18,19] The transient grating technique as we know it today, (i.e. creating a transient grating by two pulsed laser beams, and probing it by a third), was first used by Eichler et. al. to determine the bulk thermal diffusivity in ruby and glycerol.[20,21] The method was extended a step further when Phillion et al. combined it with picosecond

laser techniques to resolve the short lifetimes of electronic excitations.[22] Since then it has been used to determine energy deposition quantum yields resulting from the deposition of a thermal grating[23], and to detect ground state[24] and excited state-excited state absorption[25] in condensed phase solutions. Rotational reorientation rates from Kerr effect gratings in liquid crystals[26] have been determined, as well as the diffusivity of radical ions in concentration gratings in flames[27]. A particularly important application has been to the study of acoustic propagation in anisotropic media.[28,29] And in semiconductors, excited state gratings have provided a means of observing electronic processes such as anisotropic state filling.[30]

More recently, the TG technique has proven quite successful for studying thermal flow[31] and acoustic propagation[13] in thin films as it has the advantage of non contact generation and detection of a well-defined heat source at the surface or in the bulk of a sample.[32] Like the photothermal deflection method, the TG technique is sensitive to minute displacements of the surface, and can be used to determine the surface temperature profiles and expansion dynamics[33]. Unlike other photothermal methods, however, transient gratings have the ability to discriminate between signals arising from each of the three crystallographic axes of a sample simply by varying the periodicity of the grating. The experiments presented in this thesis were performed with a large fringe spacing, i.e., fringe spacing >> optical absorption depth. Under these conditions, the resulting signal is primarily due to expansion and contraction perpendicular to the surface region and can be modeled reasonably well with one-dimensional solutions. For small fringe spacing however, this technique is sensitive to the component of expansion in the plane of the surface, provided the thermal diffusivity is long relative to the rate of expansion.

While transient grating experiments have traditionally been performed in transmission, a recent paper by Fishman, et. al. has demonstrated that this method is sensitive to surface properties when performed in the reflection grating geometry, while

transmission studies are dominated by bulk properties.[34] This was experimentally demonstrated by using the technique to measure thermal flow and ultrasonic propagation in thin films.[31] In the case of a weakly absorbing material, the excite beams are primarily transmitted. As a result, absorption can be treated as uniform throughout the depth of the material. The transmitted diffracted signal is proportional to the change in the dielectric constant $\Delta\varepsilon$, created by the grating. This leads to a equal spatial weighting of the signal contributions throughout the material. The reflected signal, however, is proportional to $\frac{d\Delta\varepsilon}{dz}$ to first order in $\Delta\varepsilon$. Thus the reflection signal is only generated from the spatial regions where an abrupt change of the dielectric constant exists, i.e., the surface or interfacial regions of the sample. Similar considerations apply for even order nonlinear processes, such as second harmonic generation at a surface in a centrosymmetric medium. For an even order process, a signal is generated only where a break in the symmetry exists, i.e., at a surface or interface. In general this occurs on an atomic distance scale. Reflection transient gratings, however, are essentially odd order nonlinear experiments. In this case the maximum depth from which signal can be effectively be generated is $\frac{\lambda}{4\pi n}$, which corresponds to a material with no absorption.[35] This depth is on the order of 25 nm for most materials (n = 1.5) at visible wavelengths. As the material becomes more optically dense (i.e., absorption depth << optical wavelength), absorption becomes increasingly shallow, thus both the reflected signal and the transmitted signal are generated progressively closer to the surface. The transmitted signal contributions become exponentially less as a function of depth into the sample, comparable to the absorption depth. The reflected signal is generated from a depth into the sample comparable to one half the Beer's absorption depth. Thus while the net effect of high optical absorption is to localize all signal generation nearer to the surface, the difference between the regions probed in transmission versus reflection becomes less.

By varying the laser wavelength, one can control the optical sampling depth. The surface can selectively be studied by using a probe wavelength far down the edge of an intense absorption band where the optical density is low, thus creating a large difference between the spatial regions from which the transmitted and reflected signals are generated. As the probe wavelength approaches the absorption band, the difference in the spatial region sampled in reflection and transmission decreases. Finally, predominantly bulk properties can be studied by probing the grating in transmission. Thus by varying the laser wavelength and experimental grating geometry one can selectively probe to different depths in the sample, allowing the investigation of surface, interface, and bulk phenomena. Here we report the extension of this technique to the study of transient thermal expansion at a surface, as well as a determination of the surface thermal diffusivity.

1.3 Thermal Expansion

The expansion of a solid when heated is a direct consequence of the anharmonic nature of the interatomic forces in the solid. If the forces were purely harmonic, the mean position of the atoms would not change even though the atoms would vibrate with larger and larger amplitudes as the temperature increased. To account for thermal expansion one has to take into account the anharmonicity of the lattice vibrations. The anharmonic terms contribute to the free energy of the crystal, which is not necessarily a minimum for vibrations around the assumed equilibrium configuration in which the net displacement is zero. The whole crystal thus expands (or contracts) until it finds the volume where the total free energy is a minimum. Grüneisen's theory provides a general explanation of the phenomena using a quasi harmonic approximation of the lattice potential.[36] Thus the condition for the minimum free energy, $\mathcal{A}(T)$, is:

$$\frac{\Delta V}{V} = \chi\zeta\varepsilon(T)\,, \tag{1.1}$$

where V is the volume, ΔV is the change in volume, χ is the bulk compressibility, and ζ is the Grüneisen parameter. This is related to the linear thermal expansion coefficient, γ, by

$$\zeta = \frac{3V\gamma}{\chi C_v}\,, \tag{1.2}$$

where C_v is the specific heat at constant volume. Grüneisen parameters exist for each mode of the solid separately, and they can in general be very different from mode to mode. The linear thermal expansion coefficient is defined as the increase in length suffered per unit length of the solid when the temperature is raised by one degree Celsius. The volume expansion coefficient, γ_v is related to the linear coefficient, and to first approximation is the sum of the linear expansion coefficients in three mutually perpendicular directions in the solid. Rigorously, the thermal expansion coefficient γ_{ik} is a second rank tensor relating the temperature T (a scalar) and the second-rank strain tensor Σ_{ik} by

$$\Sigma_{ik} = \gamma_{ik} \cdot \mathrm{T}\,, \tag{1.3}$$

where

$$\gamma_{ik} = \begin{pmatrix} \gamma_{11} & \gamma_{12} & \gamma_{13} \\ \gamma_{21} & \gamma_{22} & \gamma_{23} \\ \gamma_{31} & \gamma_{32} & \gamma_{33} \end{pmatrix}. \tag{1.4}$$

The measurement of thermal expansion of crystals is important for the following reasons:

1) The expansion of a crystal is intimately related to the normal modes of vibration of the lattice and hence a study of it might be expected to throw some light on the nature of binding between the different units in the lattice.

2) The expansion coefficient is a structure sensitive property and reflects any transitions in crystal structure.

3) Expansion coefficients are needed to convert the specific heat at constant pressure, C_p, to the specific heat at constant volume, C_v. This is done through the thermodynamic relation:

$$C_p - C_v = \gamma_v V T / \chi J, \tag{1.5}$$

where J is the mechanical equivalent of heat.

4) Precise measurement of the expansion coefficient at very low temperatures provides information on the molar volume of a substance at $T = 0$. It is also useful for distinguishing the electronic and nuclear hyperfine contributions to the Grüneisen parameter from the lattice contributions.

5) Thermal expansion data enables the evaluation of the Grüneisen parameter, as well as the second Grüneisen constant,

$$\psi = \frac{\mathrm{d} \ln \gamma}{\mathrm{d} \ln V}\Big|_T, \tag{1.6}$$

both of which are fundamental to the study of many basic phenomena in solids and to the prediction of a variety of physical properties such as the equation of state.

6) A knowledge of lattice thermal expansion of a material is essential in investigations involving epitaxy and thin film growth, as well as in industrial thin film deposition.

1.4 Thermal Diffusivity and Conductivity

Heat flow across a surface is generally described by the thermal conductivity coefficient κ. This is defined with respect to the steady-state flow of heat down a long rod with a temperature gradient $\frac{dT}{dx}$ by the expression:

$$j = -\kappa \frac{dT}{dx} \ , \tag{1.7}$$

where j is the energy transmitted across a unit area per unit time. The form of this equation implies that the process of thermal energy transfer is a random process. That energy does not simply enter one end and flow in a straight path to the other end, but rather the energy diffuses through the sample, suffering frequent collisions. The random nature of the thermal conductivity process introduces the temperature gradient and the mean free path of the phonons between collisions. While κ represents the experimental observable commonly measured in thermal experiments, it is actually composed of the three basic parameters ρ, C, and D. Here ρ is the material density. The specific heat at constant pressure, C, is a measure of the number of accessible electronic and phonon modes in the solid. The final parameter D is the thermal diffusivity, which is related to the mean free path of the phonons. The thermal conductivity can be written in terms of these fundamental parameters by the relation

$$\kappa = \rho C D \ . \tag{1.8}$$

One way to understand the mechanism of heat conduction is to think in terms of the collective vibrations of the whole system rather than those of individual atoms. In a solid any displacement of a particular atom does not remain localized, but propagates through the lattice giving rise to a lattice wave. Thermal diffusion can then be described

as the propagation of energy through the crystal by these lattice waves. The waves can be quantized, and the resulting quantum is known as a phonon.

Many thermal properties of solids can be described in terms of phonon behavior. In a perfect crystal and in the harmonic approximation, the phonon modes are referred to as normal modes. However, a certain amount of anharmonicity is always present and this leads to the scattering of phonons by other phonons. In imperfect crystals, phonons may be scattered by other mechanisms, such as impurities, lattice imperfections, boundaries, etc. In heavily doped semiconductors the scattering of phonons by electrons and holes may also contribute to the total phonon scattering. We can relate the mean free path of the phonon l_{ph} to the thermal diffusivity of the lattice by the relation

$$D = \frac{1}{3} v_S l_{ph} \ , \tag{1.9}$$

where v_S is the velocity of sound. As the scattering increases, the phonon mean free path decreases. The variation of κ with temperature will thus depend mainly on the temperature dependence of C and l_{ph}, as ρ and v_S vary only slightly with temperature. Above the Debye temperature, the temperature dependence of κ is proportional to T^{-1}. As the temperature is lowered, κ rises and reaches a maximum at a temperature well below the Debye temperature. As the temperature approaches absolute zero, κ decreases rapidly, vanishing at absolute zero. A simple explanation goes as follows. As the temperature decreases the phonon mean free path increases rapidly, resulting in an increase in κ until l_{ph} becomes comparable to the crystal dimensions, or, more realistically, to the distance between crystal defects, e.g., impurities or lattice dislocations. The boundaries of crystals are usually poor reflectors of phonons, consequently their mean free paths cannot increase any further. In this temperature range the thermal conductivity of the lattice decreases with temperature at a rate proportional to T^3, which is due to the loss of heat capacity C in the material.

1.5 Ultrafast Processes in Gallium Arsenide

Gallium arsenide (GaAs) has an face centered cubic zincblend lattice structure. For the purposes of interpreting the electronic band structure and vibration spectrum of GaAs, the most important paths through the Brillouin zone are those from the zone center Γ to the high symmetry points X, L, and K on the zone boundary. Figure 1.2 shows a schematic of a portion of the calculated band structure of GaAs after Chelikowski and Cohen.[37] The top of the valence band, at $k = 0$ (Γ-point) and $E = 0$, is 4-fold degenerate. Away from the Γ-point the degeneracy is lifted and there are two 2-fold degenerate bands, the upper designated as the heavy-hole (hh) band and the lower as the light-hole (lh) band. About 340 meV below the top of the valence band at $k = 0$ lies a 2-fold degenerate band called the spin-orbital split-off (so) band.[38] The minimum of the conduction band in GaAs also lies at $k = 0$, making it a direct-gap semiconductor. The energy gap E_g, is approximately 1.43 eV at room temperature. There are two sets of satellite conduction band valleys in GaAs. The L-valleys have minima at the boundary of the Brillouin zone in the (111) direction about 310 meV above the central Γ-valley.[39] The X-valleys have minima at the zone edges in the (100) direction, about 460 meV above the central valley.[40]

Using optical methods it is possible to examine the carrier dynamics in a GaAs lattice. We are primarily interested in electronic transitions with energies near the band gap, i.e., visible excitation. These photons have wavelengths much longer than the lattice constant of the solid (5.65 Å), and thus have a wave vector that is negligible on the scale of the Brillouin zone. As a result, optical transitions must leave the wave vector of an electron essentially unchanged (dipole approximation). Thus, only vertical transitions are allowed, and for the photon energies of interest (2 eV) only states near $\Delta k = 0$ can be involved. A significant difference in the curvature of the conduction and valence bands

Figure 1.2: Schematic of a portion of the calculated band structure of GaAs (after Chelikowski and Cohen[37]). The zero of energy is taken to be at the valence band maximum.

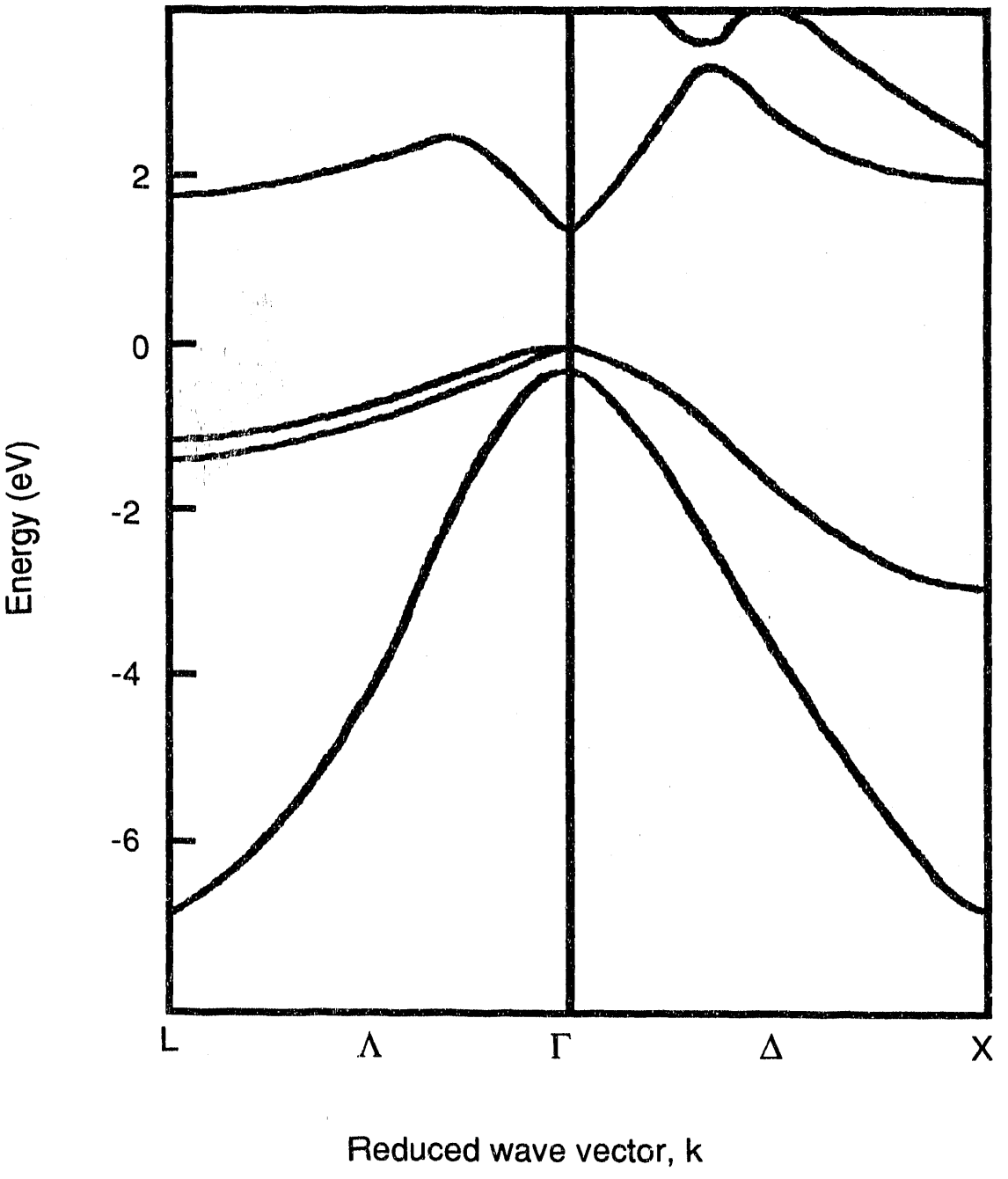
Energy (eV)
2
0
-2
-4
-6
L
Λ
Γ
Δ
X
Reduced wave vector, k

determines that most of the excess energy resides initially in the electrons rather than the holes.[41] Different densities of states in the two bands further implies that electrons in the conduction band have a much stronger influence on changes in absorption produced by the excitation. Thus optical pump-probe spectroscopy is primarily sensitive to electronic state filling in the conduction band.

Fig. 1.3 illustrates the pertinent band structure for our experiments in GaAs. For photon energies of about 2 eV linearly polarized along the (100) direction, three vertical transitions are allowed. Electrons can be excited from the split-off valence band, with about 150 meV of excess energy in the Γ-valley of the conduction band, and from both the heavy and light hole bands, with about 500 meV of excess energy. The relative strengths of the so-hh-lh transitions are about 0.15-0.42-0.42 respectively.[42,43] Carriers with energies of more than 500 meV above the Γ-valley minimum can scatter via large wave vector phonons into the X-valley, while those with more than 300 meV can scatter into the L-valley (Fig. 1.4). These scattering processes are extremely rapid and are of special importance to electronic devices since the rapid accumulation of excited carriers in the high effective mass satellite valleys leads to the reduced carrier mobility observed in hot carrier transport. These carriers only contribute to optical absorption changes when they return to the Γ-valley. Carriers that remain in or return to the Γ-valley redistribute in energy by carrier-carrier scattering and lose energy by coupling to the lattice.

Under the dipole approximation, if excitation is sufficiently far from the band edge, the optical absorption is essentially constant over the frequency bandwidth of even an ultra short optical pulse. Excitation then occurs over a continuum of states in the valence band that is at least as broad as the frequency bandwidth of the pulse. The coherent polarization associated with such a superposition of states simply follows the electric field amplitude of the excitation. As a result of the excitation of electrons and filling of states in the conduction band, the absorption spectrum of the medium is

Figure 1.3 Schematic of the GaAs(100) band structure pertinent to experiments in this thesis. For a 2 eV excitation, transitions from the heavy hole (hh), light hole (lh), and split-off (so) valence bands to the conduction band Γ-valley are allowed. Because the 4 eV probe beam looks at a set of ground states further down the valence band edge than were initially excited by the 2 eV grating, electronic effects have a negligible effect on the diffracted signal. The signal therefore arises solely from density changes at the surface created by heat transfer from the carriers to the lattice phonons and their subsequent equilibration.

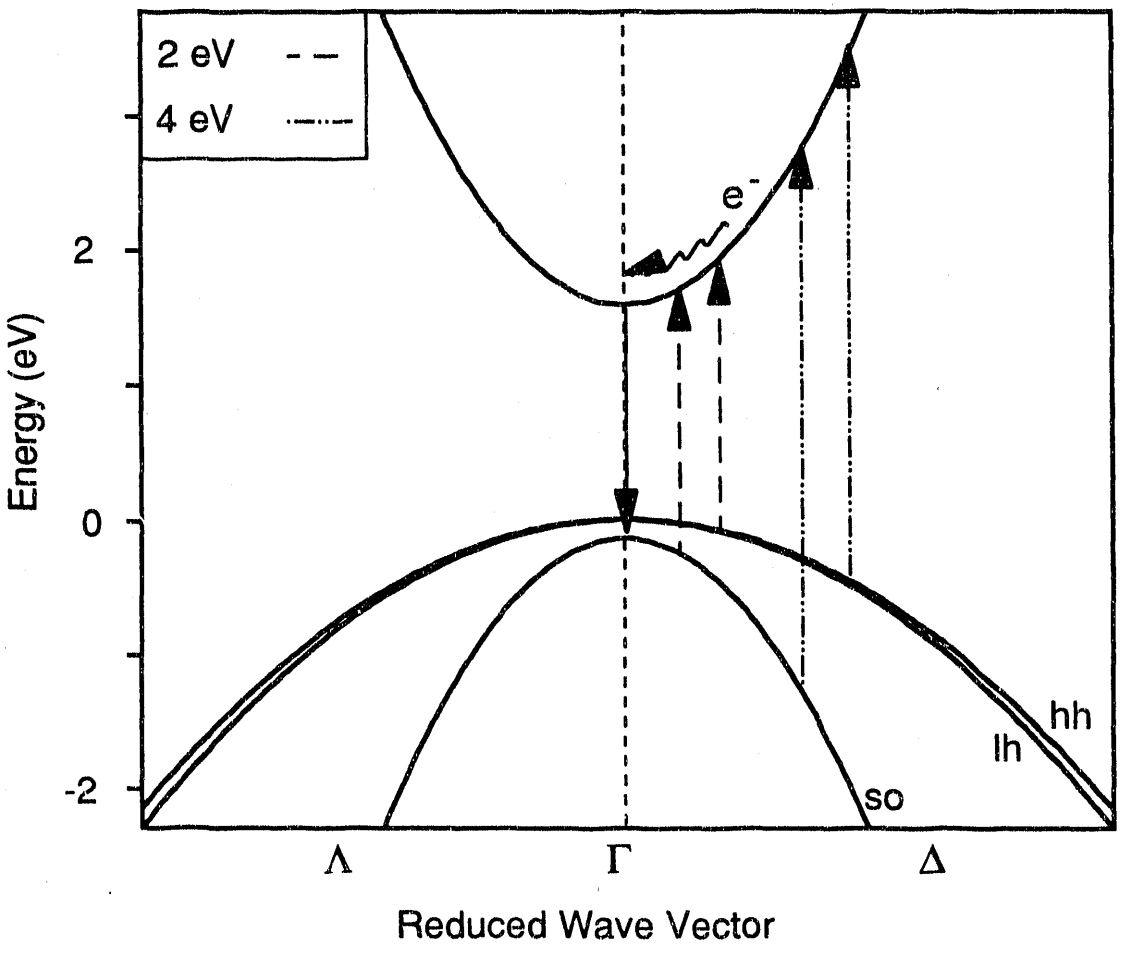
2 eV
4 eV
e⁻
2
0
-2
Energy (eV)
hh
lh
so
Λ
Γ
Δ
Reduced Wave Vector

Figure 1.4: Schematic illustration of electron and hole excitation and decay mechanisms in GaAs(100). Electrons are excited out of the valence band with energy $h\upsilon_{exc}$ leaving behind a hole (circle). Excited electrons in the Γ-valley can scatter with other electrons (e-e) or intervalley scatter to the adjacent X and L valleys, from which they may or may not return to the Γ-valley. The primary cooling mechanism of hot electrons is through emission of longitudinal optical phonons (e-p). The decay proceeds through a cascade of carrier-phonon interactions terminating in the creation of an electron-hole plasma at the minimum of the conduction band Γ-valley. Electrons then decay back to the valence band through luminescence ($h\upsilon_{lum}$), and radiatively recombine with holes in the valence band.

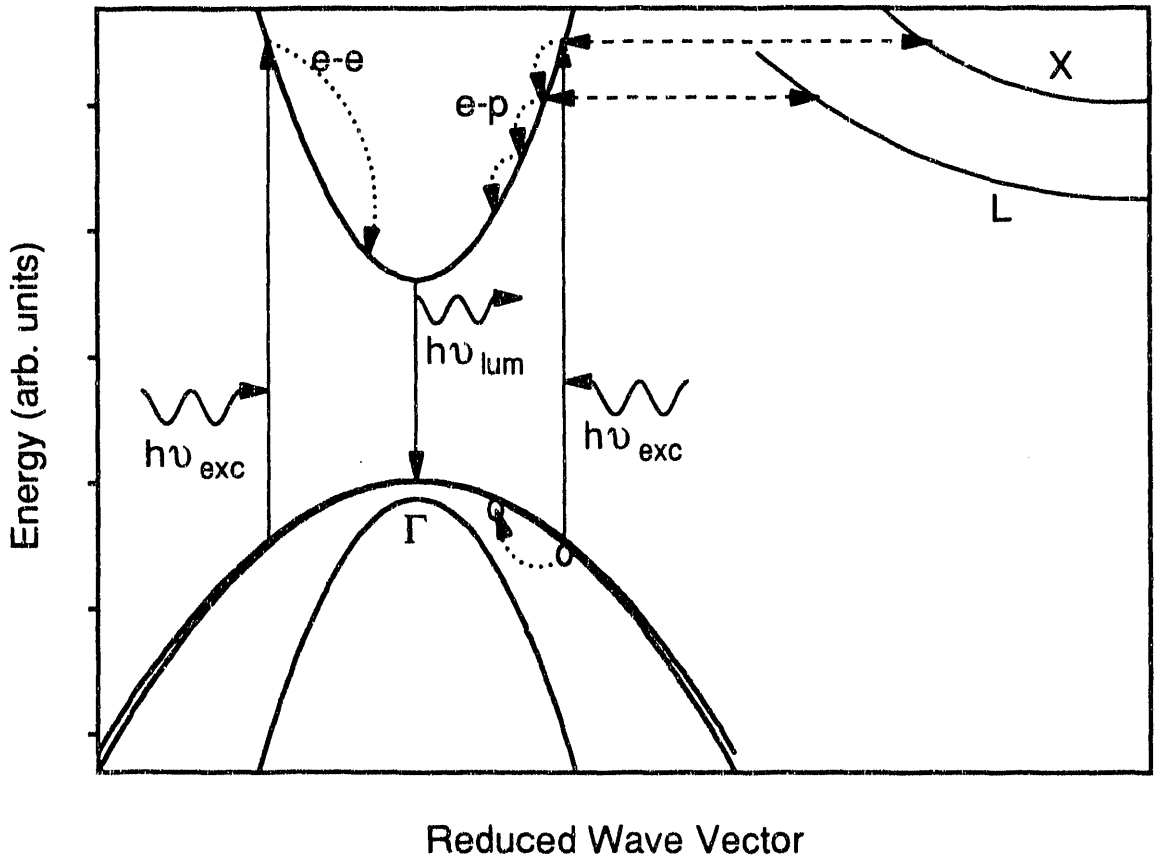
e-e
e-p
X
L
hυ lum
hυ exc
hυ exc
Γ
δ
Energy (arb. units)
Reduced Wave Vector

changed. At wavelengths near the excitation, a local decrease, or hole, appears. Disappearance of the hole corresponds to the time it takes electrons to scatter out of their initially excited states either by carrier-carrier scattering or by carrier-phonon scattering, and return to the valence band via radiative decay (Fig. 1.4).

Because the lh and hh bands are anisotropic in k-space, the carriers excited into the conduction band fill the available states anisotropically. This was first observed experimentally using hot luminescence spectroscopy,[44,45] and has been shown to depend upon the orientation of the polarization of the laser relative to the crystallographic axes[46]. Using orthogonally polarized excitation pulses, the anisotropic state filling in semiconductors has been observed via the transient grating technique, though the anisotropy is generally weak.[30] Subsequent relaxation of this anisotropic carrier distribution provides a means of measuring the momentum redistribution of the system.[47]

Emission of phonons is the mechanism by which hot carriers give up their energy to the lattice. We are mainly concerned with carriers near $k = 0$, which will interact with phonons near $k = 0$. The modes near $k = 0$ consist of the longitudinal acoustic (LA) and transverse acoustic (TA) modes, and the longitudinal optical (LO) and transverse optical (TO) modes. While both types of modes play a role in the relaxation of hot carriers, the dominant cooling mechanism for hot carriers with temperatures above about 30 °K in GaAs is the emission of optical phonons. Acoustic phonons have rather small energies ($\approx$ 3 meV) for the k-vectors of interest, thus they are not very efficient at cooling the electrons. The energies of the optical phonons are 33.8 meV for the TO and 36.7 meV for the LO modes, thus only a few optical phonons must be emitted in order to thermalize the carriers.[48] However, this process is only possible for relatively energetic electrons. An equilibrium distribution will never be reached by optical phonon scattering alone; the distribution will be depleted of all high energy carriers, while those with energies below the optical phonon energy will be unaffected. Further equilibration

requires the emission of acoustic phonons. Below about 20-30 °K, the electrons and holes have insufficient energy to emit the more energetic optical phonons, and cooling must proceed via the acoustic phonons. The decay proceeds through a cascade of carrier-phonon interactions terminating in the creation of an electron-hole plasma at some minimum of the conduction band.[49] Figure 1.4 shows a schematic illustration of some of the decay mechanisms described above.

An intuitive understanding of hot phonon effects can be gained by considering what happens after a carrier emits a phonon. The group velocity of the optical phonons is negligible ($\leq 10^3$ cm/s), implying that the phonons cannot move significantly during their lifetime.[50] These high frequency ($\approx 10^5$ cm^{-1}) optical phonons decay through the creation of two lower frequency acoustic phonons.[51] This occurs within approximately 3 ps in GaAs at 300 °K.[52] If the carrier density is large enough, the optical phonon can be reabsorbed before it has a chance to decay. If the reabsorption time is one fifth of the lifetime, for example, up to five phonons will have to be emitted before any energy is actually lost to the carriers. Thus the carrier cooling time would be increased by a factor of 5. It is assumed that once the optical phonon decays, the energy is lost to the carriers, as the acoustic decay products have far too large a wave vector to interact directly with the carriers. The resulting phonon distribution can thus be described by a Boltzmann distribution.[53]

The rates of all these processes may depend upon both the excess energy and the excitation density. It is often possible to separate the overall dynamic behavior into two regimes:

1) A period of rapid scattering out of the initial states into a transient, hot distribution of carriers.

2) A slower cooling of this distribution to the lattice.

This type of behavior is observed for the conditions used in our experiments which have been performed at room temperature and with carrier densities greater than 10^{17} cm^{-3}.

We discriminate between these two regimes experimentally by varying the probe wavelength. By selecting a probe wavelength near the excitation wavelength, the dominant influence on the probe in electronic, while probe wavelengths far from the excitation wavelength exhibit trends due to the thermomechanical response of the lattice.

2. THEORY

In the transient grating experiment, two laser pulses with wave vectors k'_{exc} and k''_{exc} are temporally and spatially overlapped on the surface of a sample as shown in Fig. 1.1. The interference between the two pulses forms a sinusoidal grating pattern on the sample surface with a fringe spacing, f, related to the angle between the two beams, θ, by the relation

$$f = \lambda_{exc}/2 \sin(\theta/2) , \qquad (2.1)$$

where λ_{exc} is the excitation wavelength in vacuum. The optical energy absorbed in the material results in local heating and thermal expansion, which simultaneously launches acoustic waves with a wavelength determined by the fringe spacing. This produces a time-dependent modulation of the sample density, resulting in a time-dependent oscillation of the real and imaginary indices of refraction with the same periodicity as the interference pattern. A variably time delayed probe pulse diffracts off the optically induced density modulations, producing a signal that reflects their periodicity, magnitude, and time-dependence.

A complete theoretical treatment of the transient grating signal from highly absorbing materials in the reflection geometry has recently been published, providing the formalism for analyzing the data herein.[34] This formalism includes the spatial distribution of the grating-induced dielectric constant profile perpendicular to the sample surface which had not previously been treated. If we consider a semi-infinite plane of absorbing material with a complex dielectric constant, ε, the reflected diffraction efficiency, η, is proportional to the square modulus of the grating peak-to-null difference in the complex dielectric constant. For a sample with weak absorption, the reflected diffracted signal arises from a maximum depth of $\frac{\lambda}{4\pi n}$, while the signal from a strongly absorbing sample is generated in a region within half an absorption depth from the

surface or interface. A general expression for the one-dimensional reflected diffraction efficiency of the probe is given by[34]

$$\eta(z,t) = \frac{\omega^2}{c^2} \frac{\cos^2\theta}{|\cos\theta + \sqrt{\varepsilon - \sin^2\theta}|^4} \left| \int_0^\infty e^{2i\frac{\omega}{c}\sqrt{\varepsilon - \sin^2\theta}\, z} \, \Delta\varepsilon(z,t)\, dz \right|^2 , \quad (2.2)$$

where ε, c, ω, and $\Delta\varepsilon(z,t)$ are the unperturbed dielectric constant of the sample, speed of light, probe beam angular frequency, and grating peak-to-null modulation of the dielectric constant, respectively. The complex index of refraction,

$$\tilde{n} = (n + ik) = (\varepsilon)^{1/2}, \quad (2.3)$$

is modulated with the grating periodicity, resulting in

$$\tilde{n}'(y,z,t) = \tilde{n} + \Delta\tilde{n}(y,z,t) = \tilde{n} + \cos(\beta y)\, \{\Delta n(z,t) + i\Delta k(z,t)\} , \quad (2.4)$$

where

$$\beta = 4\pi \sin(\theta/\lambda_{exc}) , \quad (2.5)$$

is the magnitude of the grating wave vector. Ignoring second order terms in Δ leads to a dielectric constant modulation with a grating peak-to-null amplitude of

$$\Delta\varepsilon(z,t) = 2\tilde{n}\{\Delta n(z,t) + i\Delta k(z,t)\} = 2\tilde{n}\, \Delta\tilde{n}(z,t). \quad (2.6)$$

Thus in the small angle limit, i.e. $|\varepsilon| >> \sin^2\theta$, Eqn. 2.2 can be reduced to

$$\eta(z,t) = \frac{(4\pi\tilde{n})^2}{|1 + \tilde{n}|^4} \left| \int_0^\infty e^{2ik_z z}\, \Delta\tilde{n}(z,t)\, dz \right|^2 . \quad (2.7)$$

Here $\Delta\tilde{n}(z,t)$ is the grating peak-to-null modulation of the complex index of refraction, and

$$k_z = \frac{2\pi}{\lambda}(n + ik)\,, \tag{2.8}$$

is the magnitude of the complex probe wave vector, where n and k are the real and imaginary indices of refraction respectively.

The driving force for the transient grating signal in our experiment is the impulsive deposition of an amount of heat q in the lattice by nonradiative relaxation following optical absorption. This leads to a spatially varying temperature distribution in the lattice given by

$$\Delta T(x,y,z,t=0) = \frac{\Delta T_O}{2} e^{-\alpha_{exc} z} (1 + \cos(\beta y)) e^{-(x^2 + y^2)/2a^2}\,. \tag{2.9}$$

Here

$$\Delta T_O = q\,(1 - e^{-\alpha_{exc} z})/\rho C \tag{2.10}$$

is the initial temperature rise at a grating peak a distance z into the surface, α_{exc} is the optical absorption coefficient at the excite wavelength, ρ is the unperturbed density, C is the heat capacity at constant volume, and a is the excitation beam radius.

At time $t = 0$, the sample has been excited by the driving force, but there are as yet no displacements. Thus the total strain and the resulting stress must be zero at $t = 0$. As the surface thermally expands, the grating peaks are displaced towards the grating nulls and perpendicular to the plane of the surface, and counter propagating acoustic waves are simultaneously launched. This creates a strain Σ in the medium, which in turn induces an isotropic thermal stress given by

$$3B\gamma\Delta T_O, \tag{2.11}$$

where B is the bulk modulus and γ is the coefficient of thermal expansion.

Application of external stress has a profound influence on the material band structure. Isotropic stress causes a shift of the energy states, while uniaxial stress in

general lowers the symmetry of the lattice. Thus at a more general level, we should consider that the light pulse changes the electron and phonon distribution function $n_e(\boldsymbol{k})$ and $n_p(\boldsymbol{k})$ by $\delta n_e(\boldsymbol{k})$ and $\delta n_p(\boldsymbol{k})$ respectively. These changes produce a stress in the sample which can be written as

$$\sigma_{ij} = \sum_k \delta n_e(k) \frac{\partial E_k}{\partial \Sigma_{ij}} + \sum_k \delta n_p(k) \hbar \frac{\partial \omega_k}{\partial \Sigma_{ij}} \tag{2.12}$$

where E_k and ω_k are the electron energy and frequency of a phonon of wave vector $\boldsymbol{k}$ respectively. The first term in Eqn. 2.12 is the electron-hole contribution to the strain associated with the deformation potential $\frac{\partial E_k}{\partial \Sigma_{ij}}$. Assuming the material is isotropic, the electronic stress is equal to

$$\frac{\partial E_g}{\partial \Sigma_{ij}} \delta n_e = - B \frac{dE_g}{dP} \delta_{ij} \delta n_e , \tag{2.13}$$

where δn_e is the total number of electrons (equal to the number of holes), E_g is the band gap, and P denotes pressure. The excited carriers couple to the phonons through their deformation potential in the excited state, and may diffuse a significant distance before losing all their energy. Thus the spatial dependence of δn_e, and hence of the electronic component of the stress can be modified by diffusion. For each photon of energy E absorbed, thermal phonons of total energy $(E - E_g)$ are produced. The second term in Eqn. 2.12 is the phonon contribution to the strain. If the phonons have a well defined thermal distribution, then their contribution to the stress is equal to

$$- \frac{3B\beta}{C} (E - E_g) \delta_{ij} \delta n_e . \tag{2.14}$$

If the electrons and phonons are in thermal equilibrium then Eqn. 2.12 reduces to the isotropic thermal stress in Eqn. 2.11. In GaAs, the electrons and phonons are known to

reach a local thermal equilibrium within 3 ps at room temperature. Because this is short relative to the time scale of the phenomena we measure, the expression in Eqn. 2.11 is sufficiently accurate for our purposes.

Because excited states have a negligible effect on the time scale of our signal, only strain-induced contributions to $\Delta\tilde{n}$ need to be considered. The grating peak-to-null variations in the real and imaginary indices of refraction due to the presence of strain, respectively, are:

$$\Delta n(z,t) = -\Sigma(z,t)\,\frac{(n^2 - 1)}{2n}\ , \tag{2.15}$$

and

$$\Delta k(z,t) = -\Sigma(z,t)\,k\ . \tag{2.16}$$

The contributions to Δn and Δk have been discussed in detail previously.[29] The strain can be related to the grating peak to null temperature difference ΔT by the relation $\Sigma = \gamma\Delta\mathbf{T}$, where γ is the 3×3 tensor representing the expansion coefficient. This expression assumes the resulting thermal expansion is instantaneous. Because GaAs is a cubic, isotropic medium, γ is diagonal and has the same magnitude along all three axes. The strain is also related to local changes in the material density by the relation

$$\Delta\rho(z,t) = -\rho_o\,\Sigma(z,t)\ . \tag{2.17}$$

The density change $\Delta\rho$ in one dimension is proportional to first order to the displacement, Δu, of the grating in that dimension.[54] Thus

$$\Delta\tilde{n}(z,t) \propto \Delta\rho(z,t) \propto \Delta u(z,t)\ . \tag{2.18}$$

The displacement of the surface due to thermal expansion provides a real experimental observable which we can use in place of $\Delta\tilde{n}$ in Eqn. 2.7 to calculate the diffraction efficiency of the reflected probe beam in the z-direction.

In order to find the time-dependent expansion in the z-direction, the acoustic field equations must be solved. For an isotropic cubic medium such as GaAs, they need only be solved in one dimension. Thus the relevant equations are:

$$\Sigma_{zz} = \frac{\partial u_z}{\partial z} \ , \tag{2.19}$$

$$\rho \frac{\partial^2 u_z}{\partial t^2} = \frac{\partial \sigma_{zz}}{\partial z} \ , \text{ and} \tag{2.20}$$

$$\sigma_{zz} = \rho v_S B \Sigma_{zz} - 3B\gamma\Delta T_O \ . \tag{2.21}$$

Here u_z is the material displacement in the z-direction resulting from the strain, Σ_{zz}, and v_S is the velocity of sound in the material. Using a Green's function solution, these equations have been solved to find the temporal evolution of the strain field.[6] With an initial condition of zero strain everywhere and the boundary condition of zero stress at the free surface, i.e. $\sigma_{zz}(z = 0) = 0$, at all times, the solution is:

$$\Sigma(z,t) \propto \{e^{-\alpha_{exc} z} (1 - \tfrac{1}{2} e^{-\alpha_{exc} v_S t})\} - \{A_{ac} e^{-\alpha_{exc} | z - v_S t |} \text{ sgn } (z - vt)\} \ . \tag{2.22}$$

Here

$$\alpha_{exc} = \frac{4\pi k_{exc}}{\lambda_{exc}} , \tag{2.23}$$

is the absorption coefficient at the excite wavelength, corresponding to an absorption depth $\delta = 1/\alpha_{exc}$. This solution assumes no flow of heat away from the surface. The first bracketed term in this equation represents the strain due to thermal expansion in the region near $z = 0$, assuming an instantaneous temperature rise of the lattice. To be completely rigorous, our calculation should take into account the rise in temperature as the nonequilibrium phonons equilibrate. However, since the phonons reach equilibrium within the first 3 ps of the signal rise the temperature rise can be treated as instantaneous

without significant impact.[52] The second term in Eqn. 2.22 describes the acoustic pulse generated by thermal expansion propagating into the bulk at the speed of sound. The magnitude of this term is determined by the acoustic amplitude parameter

$$A_{ac} = \frac{(1-R)q\gamma}{2\alpha_{exc}\pi a^2 C}. \tag{2.24}$$

where R is the reflectivity of the surface at the excite wavelength.

The change in the displacement of the surface region due to expansion only is obtained by integrating Eqn. 2.22 from z to ∞ over dz'. To first order in $\alpha_{exc}z$, the integral is proportional to

$$(1 - e^{-\alpha_{exc} v_s t}) . \tag{2.25}$$

This is valid in the near field region where $\alpha_{exc}z << 1$, corresponding to a probe depth which is shallow compared to the depth of excitation in the sample. This is a reasonable assumption for the experimental results presented here as the probe depth is $\approx$ 15% of the excite depth. We also assume that the thermally induced expansion of the surface is fast on the time scale required for the diffusion of heat out of the surface region, hence contraction of the surface is limited by thermal diffusion. The displacement of the surface region a distance z into the surface at time t is thus given by

$$\Delta u(z,t) = (1- e^{-\alpha_{exc} v_s t})\, T(z,t), \tag{2.26}$$

where $T(z,t)$ is the temperature profile due to thermal diffusion. Only diffusional flow will be considered, i.e. the mean free path of the phonons is short compared to the sample thickness.

The temperature profile as a function of time and distance into the surface can be determined by solving the heat conduction equation for a point source of unit strength and an infinitely thick absorbing material[55]:

$$\mathbf{D}\,\nabla^2\mathbf{T}(\mathbf{r},t) = \frac{\partial \mathbf{T}(\mathbf{r},t)}{\partial t} \quad . \tag{2.27}$$

The thermal diffusion constant is given by,

$$\mathbf{D} = \kappa\rho C \,, \tag{2.28}$$

where κ is the thermal conductivity tensor. The initial condition used to solve Eqn. 2.27 is given in Eqn. 2.9. The three dimensional problem is simplified by separation of variables with the appropriate boundary conditions to

$$\mathbf{T}(\mathbf{r},t) = \Delta T(x,y,z,t=0)\; T(x,t)\; T(y,t)\; T(z,t). \tag{2.29}$$

On our experimental time scale the radial diffusion of heat is small compared to the Gaussian excitation spot size, thus the x and y Gaussian profiles can be treated as constants across the excitation spot. However, the dielectric constant is also modulated in the y-direction by the grating heat profile. This cannot be neglected and leads to a solution of the form

$$T(y,t) = \frac{1}{2}\left(1 + e^{-D_y \beta 2t} \cos(\beta y)\right), \tag{2.30}$$

where D_y is the diffusion constant in the y-direction.[56] In the z-direction we apply the boundary conditions

$$\left.\frac{dT}{dx}\right|_{z=0} = 0 \tag{2.31}$$

and

$$T(z \to \infty, t) = T(t=0) \;, \tag{2.32}$$

to obtain the following 1-dimensional analytic solution to Eqn. 2.27[9]:

$$T(z,t) \propto \left\{ e^{(-\alpha_{exc}z + D(\alpha_{exc})^2 t)} \operatorname{erfc}(-z + \frac{2D\alpha_{exc}t}{2\sqrt{Dt}}) \right.$$
$$\left. + e^{(\alpha_{exc}z + D(\alpha_{exc})^2 t)} \operatorname{erfc}(z + \frac{2D\alpha_{exc}t}{2\sqrt{Dt}}) \right\} . \qquad (2.33)$$

The temperature profile used in our calculations is thus the product of equations 2.30 and 2.33. This product is substituted into Eqn. 2.26 to find the net displacement of the surface, which in turn replaces the variable $\Delta\tilde{n}$ in Eqn. 2.7. Equation 2.7 is then solved numerically to find the reflected diffracted signal efficiency, η, using the computer codes presented in the Appendix of this thesis.

Again, at a more general level, carrier diffusion can influence the shape of the phonon pulse. Although thermalization occurs extremely fast, excited carriers may diffuse a significant distance before they transfer all their energy through phonon emission to the lattice. This nonequilibrium diffusion results in a phonon pulse broader than the initial distribution of the sample. The problem of a nonequilibrium electron gas in a lattice has been treated theoretically[57] and extensively studied since the advent of subpicosecond lasers[11,12]. In describing nonequilibrium electron heating, the material may be treated as two coupled thermal systems composed of the electrons and the crystal lattice. When an ultra short laser pulse deposits energy in the conduction electrons, they rapidly thermalize via electron-electron scattering. Energy is then transferred to the lattice through electron-phonon scattering. If the incident pulse duration is sufficiently short relative to the electron-phonon energy transfer time, a nonequilibrium temperature difference will exist between the electrons and the lattice. Since the electronic heat capacity is much less than the lattice heat capacity, it is possible to produce transient electron temperatures far in excess of the lattice temperature. Furthermore, the dynamics of this process are nonlinear since the electronic specific heat is temperature-dependent.

The temporal evolution of the electron and lattice temperatures, T_e and T_ℓ respectively, can be modeled by a set of coupled differential equations.[57] These are:

$$\rho C_e \frac{\partial T_e}{\partial t} = \kappa \nabla^2 T_e - g(T_e - T_\ell) + A(r,t) \tag{2.34}$$

and

$$\rho C_\ell \frac{\partial T_\ell}{\partial t} = g(T_e - T_\ell) \tag{2.35}$$

where C_e and C_ℓ are the electronic and lattice heat capacities respectively, ρ is the density, and κ is the thermal conductivity. Heating due to the incident optical pulse is accounted for by the source term $A(r,t)$, and electron diffusion is accounted for by the diffusion term $\kappa\nabla^2 T_e$. The electron and lattice temperatures are coupled through the electron-phonon coupling constant g, which is independent of temperature.[58] Since the electronic heat capacity is linearly proportional to the electron temperature, the effect of an increased electronic temperature is an increased thermal relaxation time. Hot electrons also have a much larger thermal diffusivity ($\kappa/\rho C_e$) than in the case of equilibrium thermal transport ($\kappa/\rho C_\ell$). However, the nonequilibrium thermal distribution typically equilibrates within 1 ps, thus we have not included the influence of carrier diffusion in our calculations.

3. EXPERIMENT

3.1 Laser System

The dispersion compensated colliding pulse mode-locked ring dye laser (CPM) used for these experiments was based on a variation of an original design by Fork et al.[59,60] The layout of the laser system currently used in our laboratory is shown in Figure 3.1. The dye laser was pumped with a cw argon ion laser tuned to a wavelength of 514.5 nm with a single line output power of 3-6 watts. The gain medium used in the ring dye laser was a solution of rhodamine 6-G organic dye in ethylene glycol with the concentration set to absorb ≈ 90% of the pump beam. The stimulated emission was collected by concave mirrors around the gain jet, resulting in two counter-propagating pulses in the cavity at any given time. A saturable absorber jet was positioned one quarter of the cavity length away from the gain jet so that the pulses met in the saturable absorber and reached the gain jet at one half the round trip cavity time, resulting in optimum gain for both pulses. The interaction between the two pulses as they met in the saturable absorber resulted in the production of mode-locked pulses.[61-65] The saturable absorber medium was 3,3'-diethyloxadicarbocyanine iodide (DODCI) dissolved in ethylene glycol with a small signal loss of 20%. The internal cavity repetition rate of 85 MHz of the laser was determined by the cavity length. Pulses were extracted from the cavity at 8 kHz using an acousto-optic cavity dumper. The dye lase typically produced 90 fs pulses with a bandwidth of 4 nm centered at 620 nm and pulse energies of approximately 800 pJ/pulse.

The output of the CPM was amplified using a six-pass configuration in an optically flat jet of rhodamine 640 laser dye in ethylene glycol.[66] The dye was pumped by a copper vapor laser (CVL), which produced 25 ns pulses in two lines (510 and 578 nm) with an average output of 25 W at 8 kHz. Timing of the CVL pulses was

Figure 3.1: Layout of the amplified dispersion compensated colliding pulse mode-locked ring dye (CPM) laser system used for the work in this thesis. The dye laser was pumped with a cw argon ion laser. The gain medium used in the ring dye laser was a solution of rhodamine 6-G organic dye in ethylene glycol in a jet. A saturable absorber jet of 3,3'-diethyloxadicarbocyanine iodide dissolved in ethylene glycol, was positioned one quarter of the cavity length away from the gain jet. The internal cavity repetition rate of 85 MHz was determined by the cavity length of the laser. Pulses were extracted from the cavity at 8 kHz using an acousto-optic cavity dumper. The output of the CPM was amplified using a six-pass configuration in an optically flat jet of rhodamine 640 laser dye in ethylene glycol. The dye was pumped by a copper vapor laser at 8 kHz. Timing of CVL pulses was synchronized with the output of the cavity dumper using a optical trigger from the CPM. A saturable absorber jet between the fourth and fifth passes through the gain jet suppressed amplified spontaneous emission and sharpened the leading edge of the pulse, resulting in an average pulse length of 90 fs.

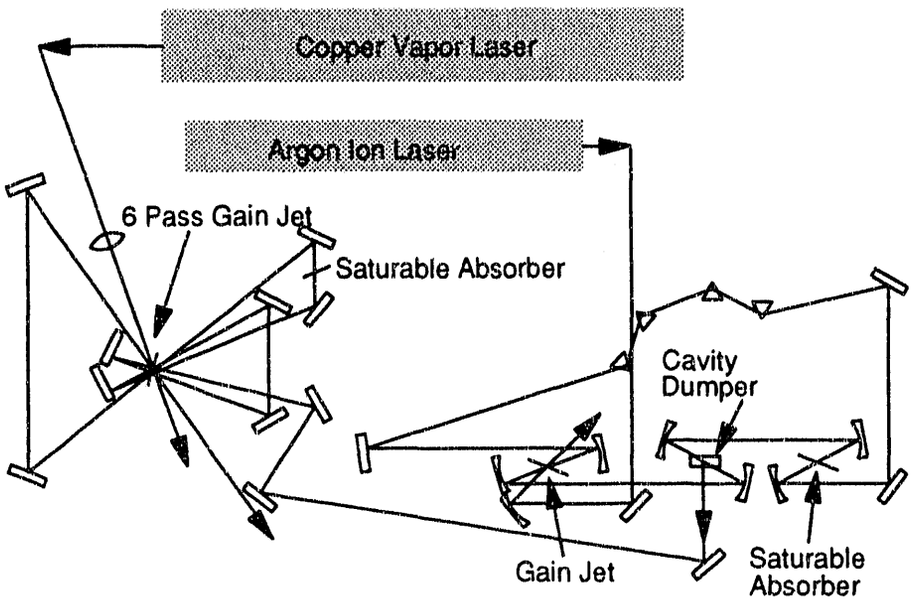
Copper Vapor Laser
Argon Ion Laser
6 Pass Gain Jet
Saturable Absorber
Cavity
Dumper
Gain Jet
Saturable
Absorber

synchronized with the output of the cavity dumper using a optical trigger from the CPM. A saturable absorber jet between the fourth and fifth passes through the gain jet suppressed amplified spontaneous emission and sharpened the leading edge of the pulse. The saturable absorber consisted of a solution of malachite green dye in a methanol solution. The resultant amplified pulses had a typical energy of 3 μJ/pulse. To improve the beam quality, a spatial filter was installed at the output of the amplifier, reducing the pulse energy by approximately 25%.

3.2 Transient Grating Experimental Setup

The optical setup used in our two-color reflection transient grating experiments is shown in Fig. 3.2. The s-polarized 2.0 eV (red) light was frequency doubled to 4.0 eV (UV) using a bare 300 μm thick KDP crystal. The residual 2 eV light was separated by a beam splitter, then rotated to p-polarization, making all the beams of like polarization. The 2 eV beam was split into two excitation beams of equal energy, with a maximum of 180 nJ each. One of the beams was directed into a computer-controlled delay stage, providing control of the temporal overlap of the two excitation beams. The two beams were beams focused to a 85 μm spot size, and were temporally and spatially overlapped on the sample.

Temporal overlap between the two red beams was obtained by maximizing the self-diffraction signal intensity generated from the sample. Self-diffraction only occurred when the two beams were temporally and spatially overlapped. This phenomena also provided an autocorrelation of the laser pulse length, which is shown in Figure 3.3. The autocorrelation was performed at the sample by scanning the temporal delay between the two excite beams and monitoring the resulting self-diffraction signal. The autocorrelation was performed both outside and inside the vacuum chamber in order

Figure 3.2 Transient grating experimental setup. A 90 fs laser pulse at 620 nm was frequency doubled to 310 nm using a 300 μm thick KDP crystal. The residual 620 nm light was split into two excite beams that were spatially and temporally overlapped on the GaAs(100) surface at an angle θ to create a periodic modulation of the dielectric constant. The sample was located inside a UHV chamber to reduce surface damage due to surface contamination. The variably time delayed 310 nm probe was diffracted off the laser-induced modulations to monitor the grating signal. The diffracted signal (DS) was detected with a photomultiplier tube (PMT) and processed via computer controlled lock-in amplification techniques.

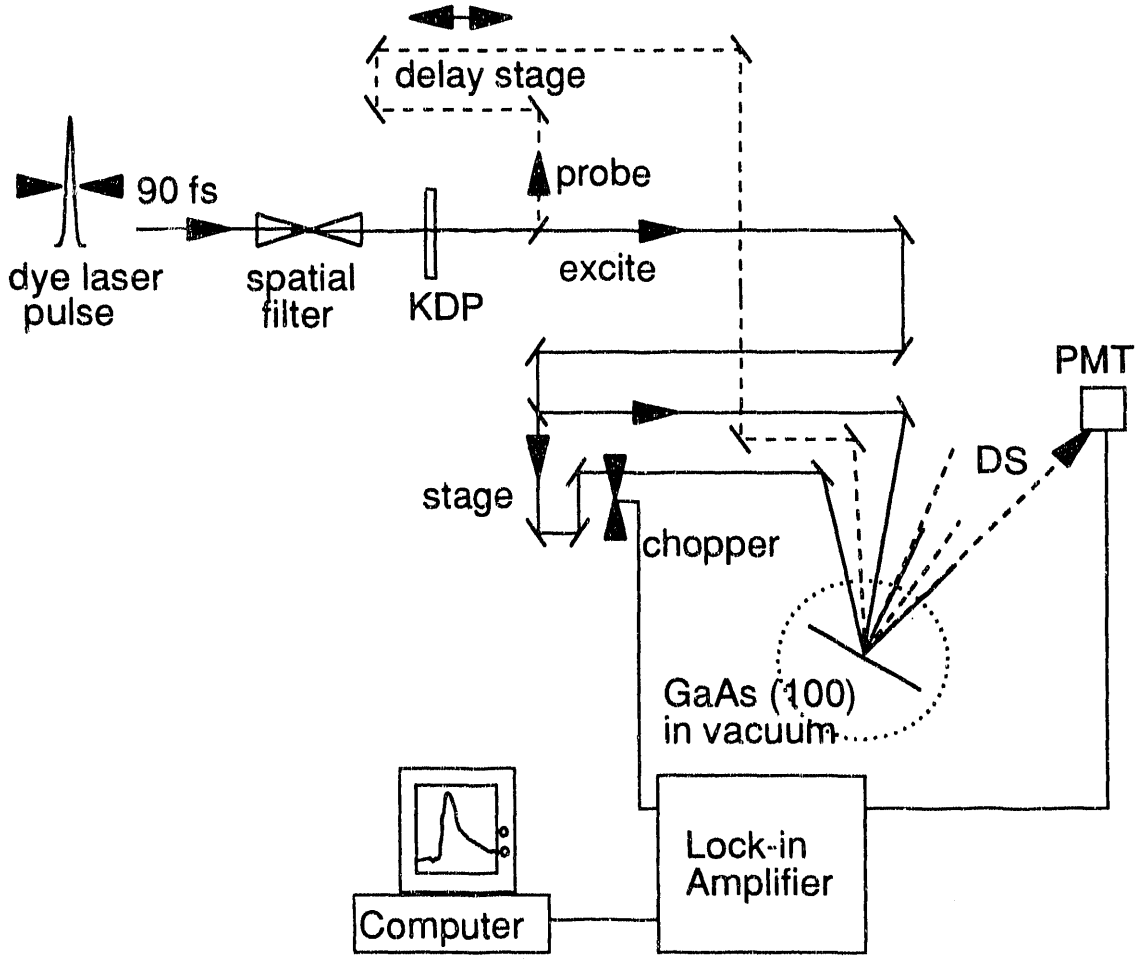
delay stage
probe
90 fs
dye laser
pulse
spatial
filter
KDP
excite
PMT
DS
stage
chopper
GaAs (100)
in vacuum
Lock-in
Amplifier
Computer

Figure 3.3: Temporal overlap between the two red beams was obtained by maximizing the self-diffraction signal intensity (squares) generated from the sample inside the UHV chamber. This phenomena also provided an autocorrelation of the laser pulse length at the sample. The pulse shape was somewhat asymmetric due to dispersion induced by the quartz window of the vacuum chamber. The net effect was to steepen the rising edge to a 65 fs rise Gaussian, while the falling edge was best fit with an 80 fs Gaussian (solid line). This produced a net pulse length of approximately 75 fs.

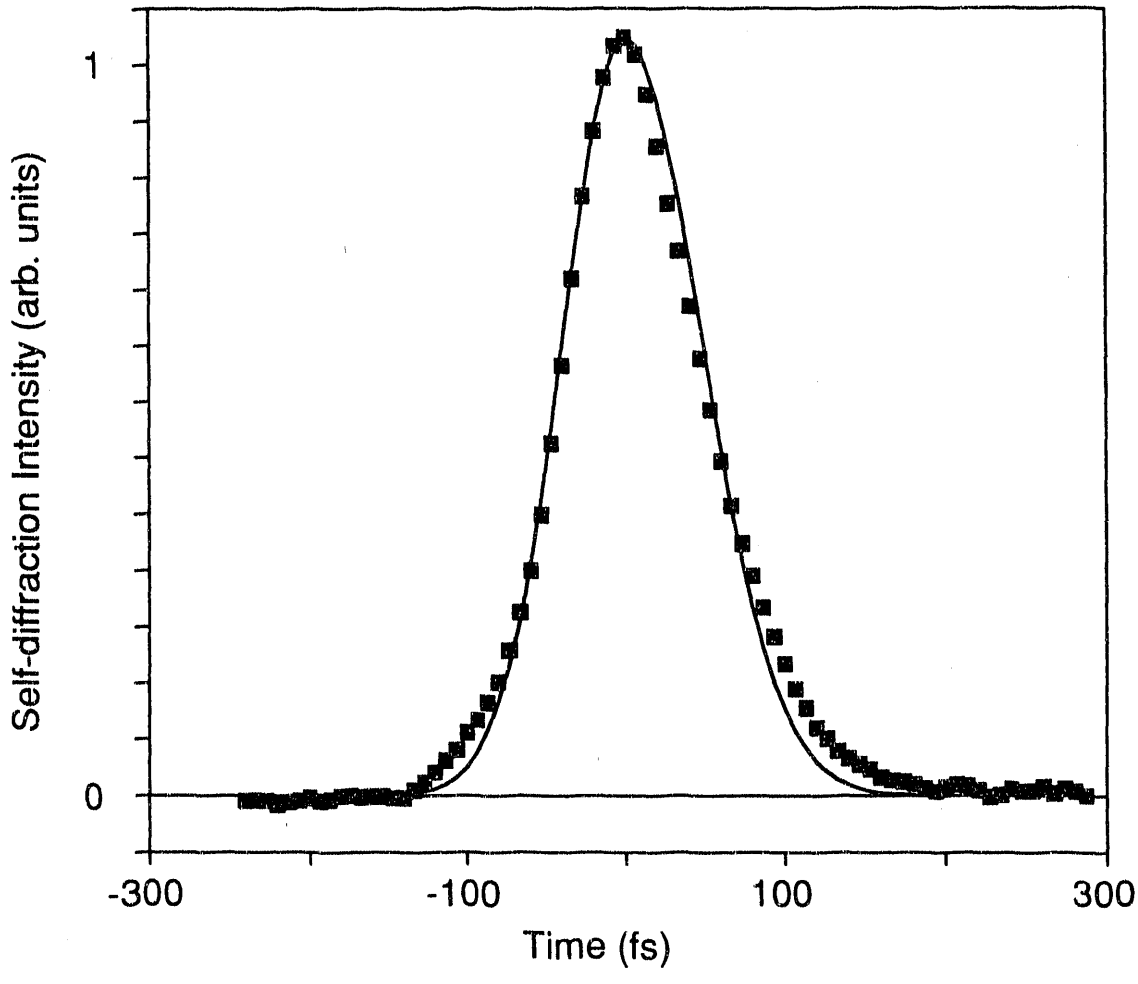
Self-diffraction Intensity (arb. units)
1
0
-300
-100
100
300
Time (fs)

to correct the pulse length for dispersion induced by the quartz chamber windows. The typical autocorrelation shown in Fig. 3.3 is best fit with a Gaussian pulse shape, i.e.,

$$I(t)^{-1/2} \propto \exp(-2(\ln 2)t^2/\tau_p^2) \ , \tag{3.1}$$

where $I(t)$ is the square root of the average intensity and τ_p^2 is the full width at half maximum.[67] The pulse shape was somewhat asymmetric due to dispersion induced by the quartz window of the vacuum chamber. The net effect was to steepen the rising edge to a 65 fs Gaussian rise, and broaden the falling edge , which was best fit by an 80 fs Gaussian. This produced a net pulse length of approximately 75 fs at full width half maximum (FWHM). The pulse length varied between 75 and 100 fs from day to day.

The 4 eV light was carefully recollimated after frequency conversion using a 2:1 up-collimating telescope. This allowed independent collimation and adjustment of the red and UV spot sizes. The UV light was then directed into an aluminum coated retroreflector mounted on a computer-controlled delay stage (1 μm step size) for use as the probe beam. The stage was aligned to better than 100 μrad deviation in pointing over the length of the stage to prevent anomalies in the measured signal decay. Alignment and collimation of the beam were verified by scanning over the length of the stage with a 50 μm pinhole in place of the sample. Less than 2% variation in the transmitted intensity through the pinhole was observed. The UV probe beam was strongly attenuated to obtain an energy of ≈ 15 pJ/pulse. It was then focused to a 65 μm diameter on the sample. The probe beam was incident at an angle bisecting the two excitation beams as shown in Fig. 3.4.

The timing between the red and UV beams was set outside the vacuum chamber using a kinematic mirror and pinhole to reproduce the sample location inside the vacuum chamber. A spare quartz window, equivalent to that used on the vacuum chamber, was added to the beam path to account for the difference in optical path lengths encountered by the red and UV beams. Temporal overlap between the red and UV beams was set by

Figure 3.4. Two-color reflection transient grating geometry. The two 620 nm grating excitation beams, with wave vectors k'_{exc} and k''_{exc}, cross at an angle θ at the surface. The time delayed 310 nm probe beam bisects the angle between the excitation beams, giving rise to a diffracted signal collinear with both of the specularly reflected excitation beams.

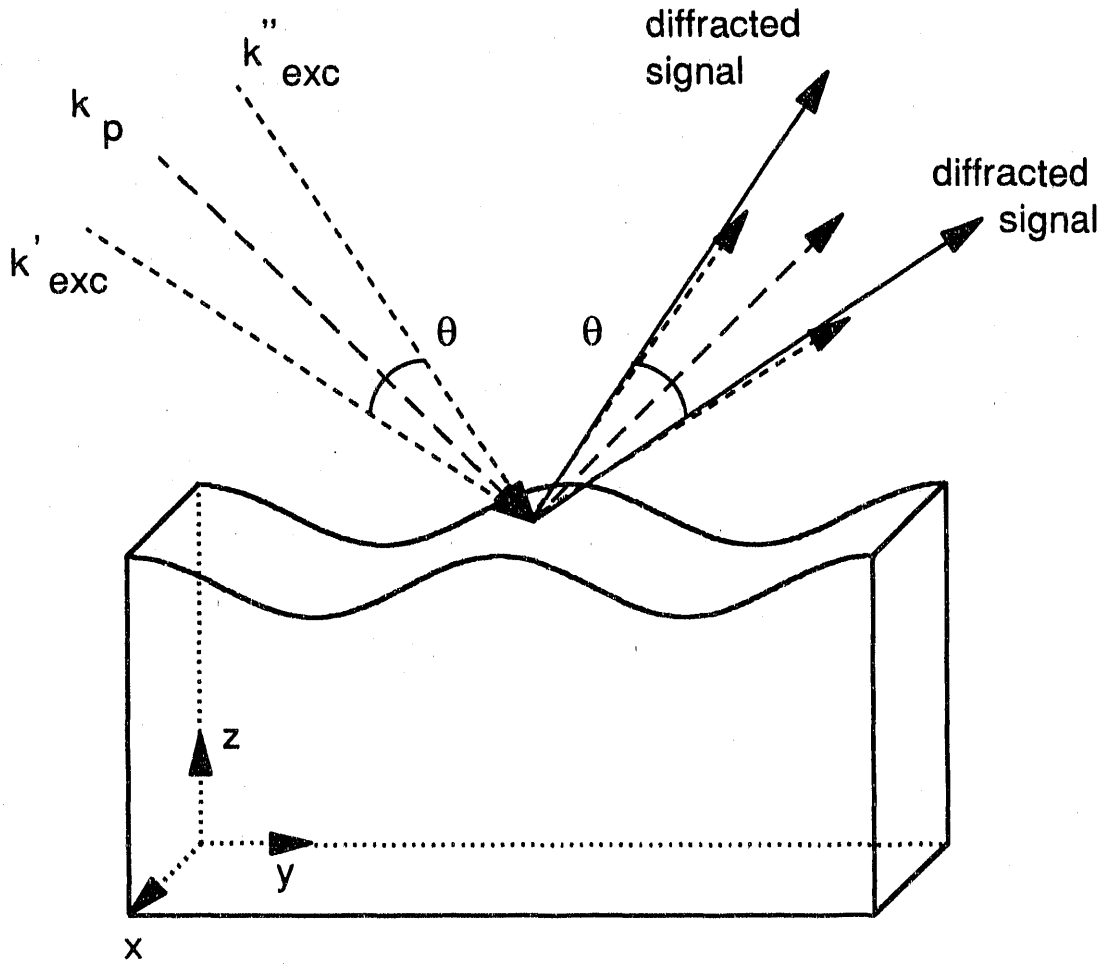
k"exc
kp
k'exc
diffracted signal
diffracted signal
θ
θ
z
y
x

performing optical pump-probe spectroscopy to monitor the transient absorption of the UV beam in trans-1,4-diphenyl-1,3-butadiene (DPB). A 7.8×10^{-5} molar solution of DPB in hexane in a 1 cm quartz cell was pumped with the 310 nm beam focused to a 90 μm spot size. One attenuated red beam, focused to a 65 μm spot size, served as a probe of the transient absorption. The UV beam was temporally delayed with respect to the red beam by scanning the UV delay stage. The UV pump beam was chopped at a rate of 395 Hz. The change in the transmitted probe intensity with and without the pump beam present was detected by a photodiode and lock-in amplifier whose output was digitized by a computer using the detection electronics described below.

When the DPB molecule is initially excited, its transition dipole moment lies along the direction of the polarization of the exciting laser beam. If the probe also lies along that direction, the molecule can immediately begin to absorb the probe. The first photon excites the molecule to the $^1B_{1u}$ state, from which transient absorption takes place.[68] The transient absorption then decays with a time constant characteristic of the fluorescence time of the DPB molecule. For spectra where the UV and red beams are polarized parallel to one another, a pulse width limited rise time followed by a single exponential decay with a 460 ps decay constant is observed (Fig. 3.5). This is characteristic of a molecular diffusion process. Because the rise time of the electronic transition is virtually instantaneous when the two beams are temporally coincident, it provides an excellent means of setting the temporal overlap.

Transient grating experiments were performed for several fringe spacings ranging from 3 to 10 μm. For the data presented here, the angle between the two excitation beams was 7.2° as denoted by θ in Fig. 3.4, which led to a fringe spacing of 5 μm. The excite pulses interacted with the sample to create a spatially modulated distribution of free carriers, or population grating, as well as a thermal grating at the surface. In order to determine the resulting angle of the grating signal one must consider the grating wave vector matching conditions for the beams involved. Because the grating depth was so

Figure 3.5 Transient absorption signal in trans-1,4-diphenyl-1,3-butadiene used for setting the temporal overlap (T = 0) between the red and UV beams.

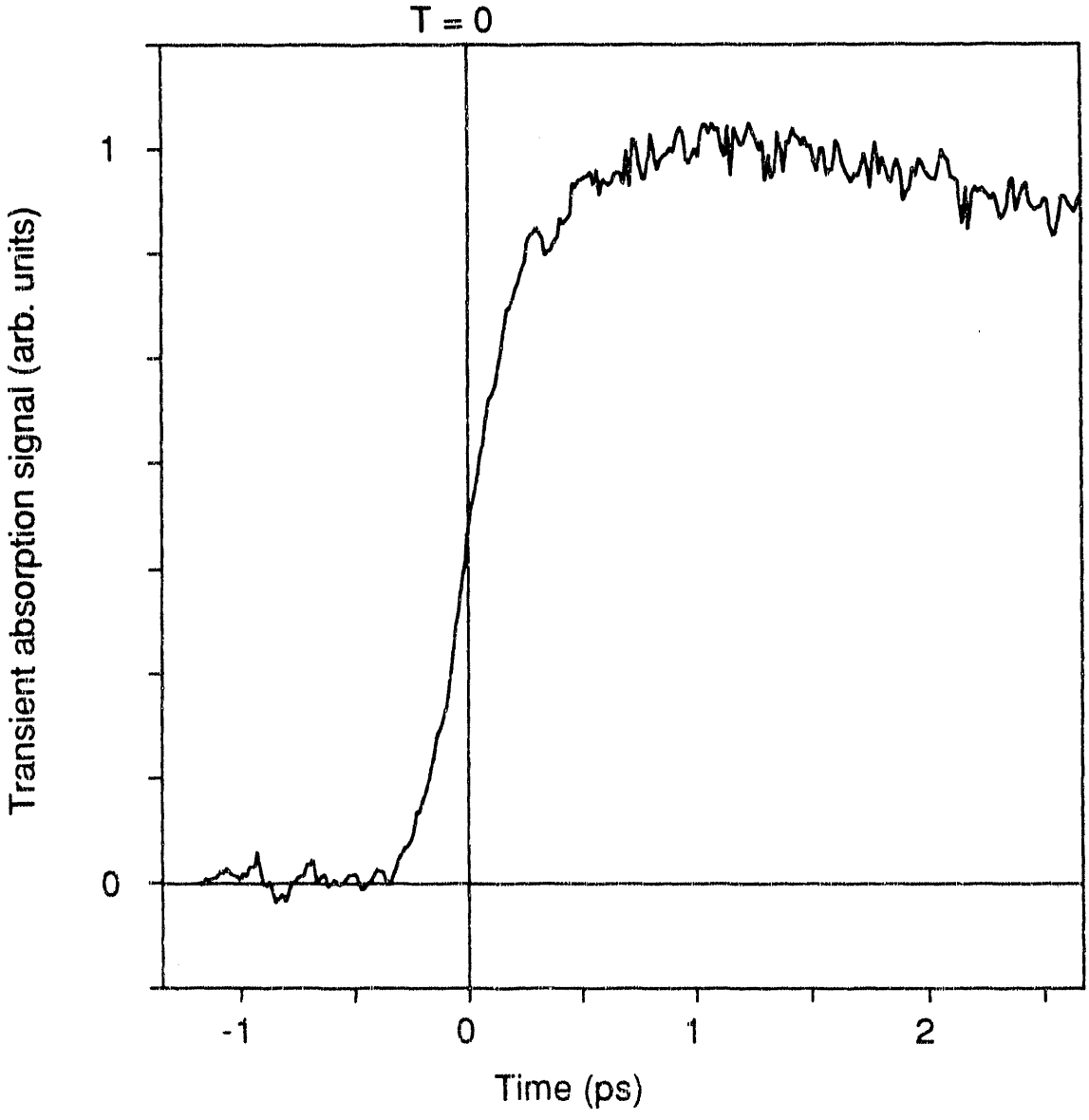
T = 0
Transient absorption signal (arb. units)
1
0
-1
0
1
2
Time (ps)

shallow (i.e., $1/\alpha_{exc} << \lambda_{exc}$), the Bragg condition for diffraction was relaxed. This led to significant diffraction in both the ±1 orders of diffraction. Hence the wave vector matching conditions for the signal were

$$k_S = k_p \pm \beta, \tag{3.2}$$

where

$$\beta = \pm (k_T' - k_T''), \tag{3.3}$$

as is shown in Fig. 3.6. The resulting diffracted signal appeared in reflection, collinear with both of the specularly reflected excitation beams.

Excitation beam k_{exc}' was optically chopped at a rate of 395 Hz, and the diffracted signal collinear with the reflected excitation beam k_{exc}'' was detected by an R1784 Hamamatsu photomultiplier tube in a Thorn EMI R1527 pulsed base. A block diagram of the detection electronics is shown in Fig. 3.7. The data collection software used for these experiments, FSDATA, was graciously provided by the Fayer group at Stanford University. The software, written by Todd Guion and upgraded by Scott Greenfield, contains both data collection routines and a sophisticated collection of data analysis programs. The data collection aspect of the program was designed to work with a Data Translation analog-to-digital converter (A/D) card and an IBM compatible computer. The software works with either lock-in amplifier detection methods or by using two gated integrators and normalizing the signal with respect to the laser intensity. Because the noise on our laser system had large peak to average intensity variations, but did not have periodic dropouts, we chose to use lock-in amplification techniques. The signal was isolated by lock-in amplification methods, then sent to the analog-to-digital converter card. This program has the capability to normalize laser intensity fluctuations, however, this feature is unnecessary for lock-in amplification methods.

Figure 3.6: Wave vector matching diagram for transient grating experiments. The wave vectors are defined as follows:

k'_{exc} and k''_{exc} are the excitation wave vectors

k'_T and k''_T are the transmitted excitation wave vectors

k_p is the probe wave vector

k_s is the diffracted signal wave vector

β is the grating wave vector

(a) Grating Excitation

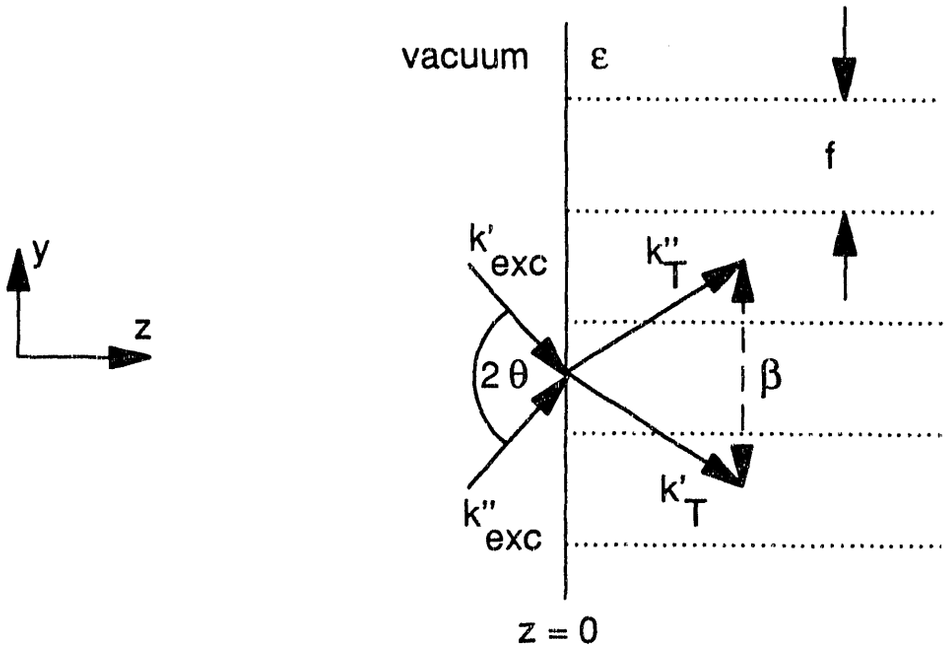

(b) Probe Diffraction

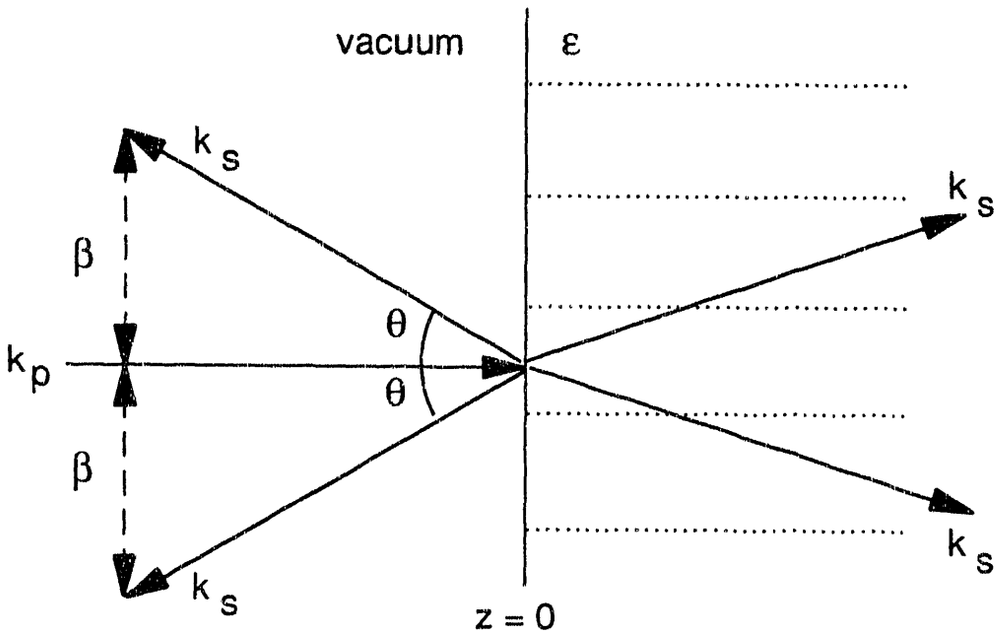

Figure 3.7: Block diagram of the detection electronics used for experiments in this thesis. The signal was isolated by lock-in amplification methods, then sent to an analog-to-digital (A/D) converter card. A 4.5 V power supply served as a substitute reference signal to provide a signal baseline for the A/D card. A TTL 2-pulse box was used to provide the A/D card with a signal to coordinate the timing for data collection on each shot. This box also provided the computer with an interactive clock pulse to initialize the A/D card for each laser shot.

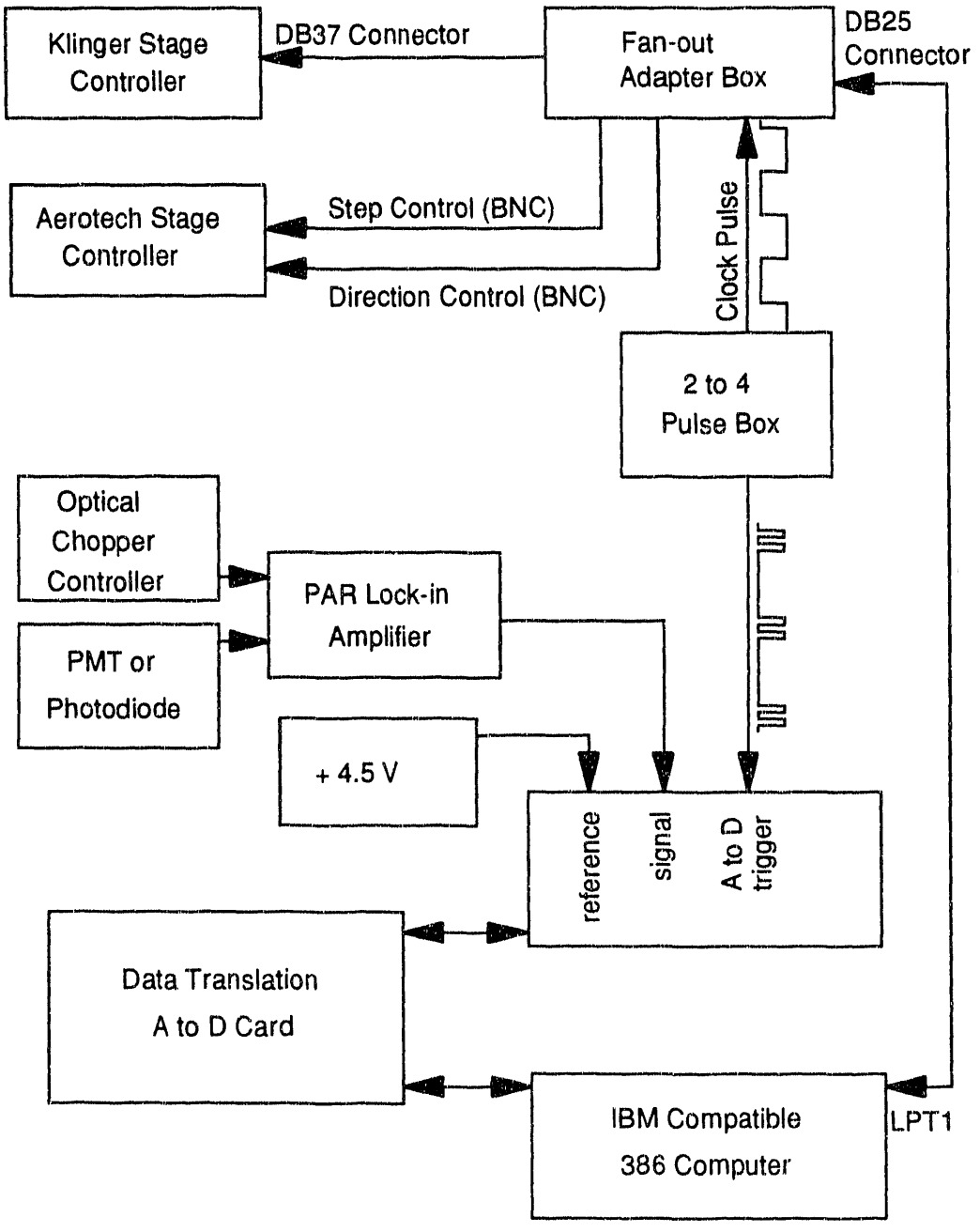
Klinger Stage Controller
DB37 Connector
Fan-out Adapter Box
DB25 Connector
Aerotech Stage Controller
Step Control (BNC)
Direction Control (BNC)
Clock Pulse
2 to 4 Pulse Box
Optical Chopper Controller
PAR Lock-in Amplifier
PMT or Photodiode
+ 4.5 V
reference
signal
A to D trigger
Data Translation A to D Card
IBM Compatible 386 Computer
LPT1

Thus a 4.5 V power supply served as a substitute reference signal to provide a signal baseline for the A/D card. A TTL 2-pulse box was used to provide the A/D card with a signal to coordinate the timing for data collection on each shot. This box also provided the computer with an interactive clock pulse to initialize the A/D card for each laser shot. The stage remained stationary for 10-1000 data points before moving to the next delay position. A typical scan took 300 shots at each delay time, requiring approximately 15 minutes per scan. Several scans were averaged to improve signal to noise for each data set. When using the full delay available (850 ps), the minimum step size was 10 μm, corresponding to a time resolution of 66 fs/step. Shorter scans provided a maximum cavity length of the laser resolution of 6.6 fs/step.

3.3 GaAs Experiments

Experiments were performed on p-type, n-type, and undoped single crystal GaAs(100) samples, nominally 300-500 μm thick, with a variety of dopant concentrations. Samples were prepared by mechanical polishing and chemical etching in order to obtain the high quality optical surface required for transient grating experiments (i.e., better than $\lambda/2$ over the excitation spot size). The samples were placed in an ultrahigh vacuum chamber, maintained at 10^{-9} torr, to reduce damage due to surface contamination and condensation during low temperature experiments. Because gallium arsenide segregates when annealed, it was not possible to sputter and anneal the surface for cleaning purposes. As a result, all samples had a thin surface oxide layer (2-3 nm), verified by Auger spectroscopy, which resulted in a slight increase in the absorption coefficient of the materials. However, because the oxide layer was much thinner than the optical absorption depth, it both expands much less and has little direct effect on the optical properties.

In order to perform the experiments in this thesis, the UHV system used was designed and constructed from the ground up. Schematic drawings and specifications of the vacuum chamber are shown in Figure 3.8 and Table 3.1. Two 6-inch quartz vacuum windows allowed optical access to the sample in order to vary the grating fringe spacing over a wide range. Other ports were arranged to allow standard UHV diagnostics to be mounted in convenient locations. These included LEED, Auger, and mass spectrometers. The chamber was designed with an on-axis manipulator in order to perform angle-resolved experiments easily. A Vacuum Generator sample mount allowed rotation of the sample about the axis perpendicular to the crystal face. This was mounted to a Varian flange allowing x,y, and z translation of the sample, as well as rotation about the manipulator axis. The temperature was controllable over a range of 120-1000 °C using a Vacuum Generator temperature controller. The pressure was maintained below 10^{-9} torr by a 400 l/s Varian ion pump and a titanium sublimation pump, as well a CTI cryopump for use in experiments requiring a magnetic field-free environment.

In order to perform the low temperature (< 120 °C) experiments in this thesis, the sample manipulator described above was replaced by the custom designed low temperature manipulator shown in Fig. 3.9. A UHV liquid helium cooled cryostat was mounted to the chamber through a Varian x-y-z translation flange, allowing access to multiple samples and precise adjustment of the spatial beam overlap. Up to seven samples were mounted on an oxygen free high conductivity (OFHC) copper sample block attached to the end of an OFHC copper rod. The dimensions of the rod were chosen to maximize thermal conduction to the sample. Because surface oxidation dramatically reduces the thermal conductivity of copper at low temperatures, all copper pieces were acid etched to remove oxide buildup. They were then gold electroplated to prevent further oxidation of the copper. The rod was attached to the tip of the cryostat, using indium washers between all surfaces to provide good thermal contact. The sample temperature was monitored at each end of the sample rod by Lakeshore Cryogenics

Figure 3.8 Schematics of the UHV chamber designed for the experiments in this thesis. Specifications are given in Table 3.1. Parts (a) - (d) show views of the chamber from different angles.

(a)

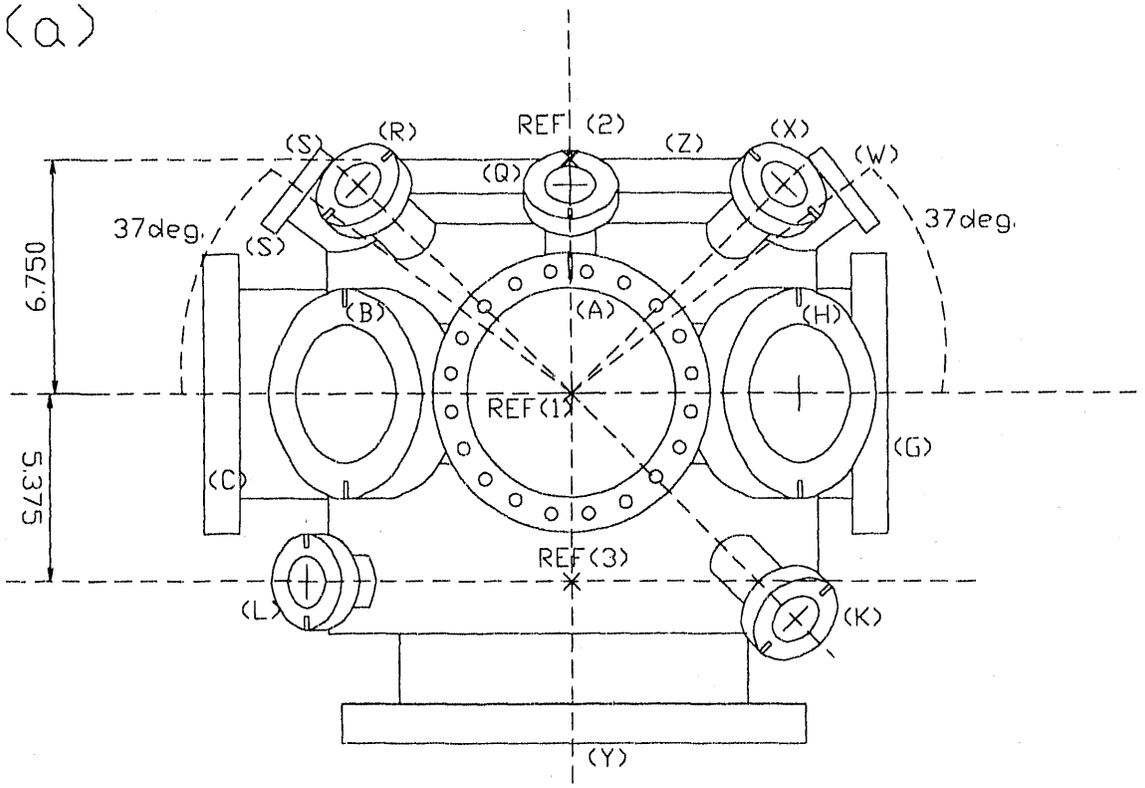
REF (2)
(S)
(R)
(Q)
(Z)
(X)
(W)
37deg.
37deg.
(S)
6.750
5.375
(B)
(A)
(H)
REF (1)
(G)
(C)
REF (3)
(L)
(K)
(Y)

(b)

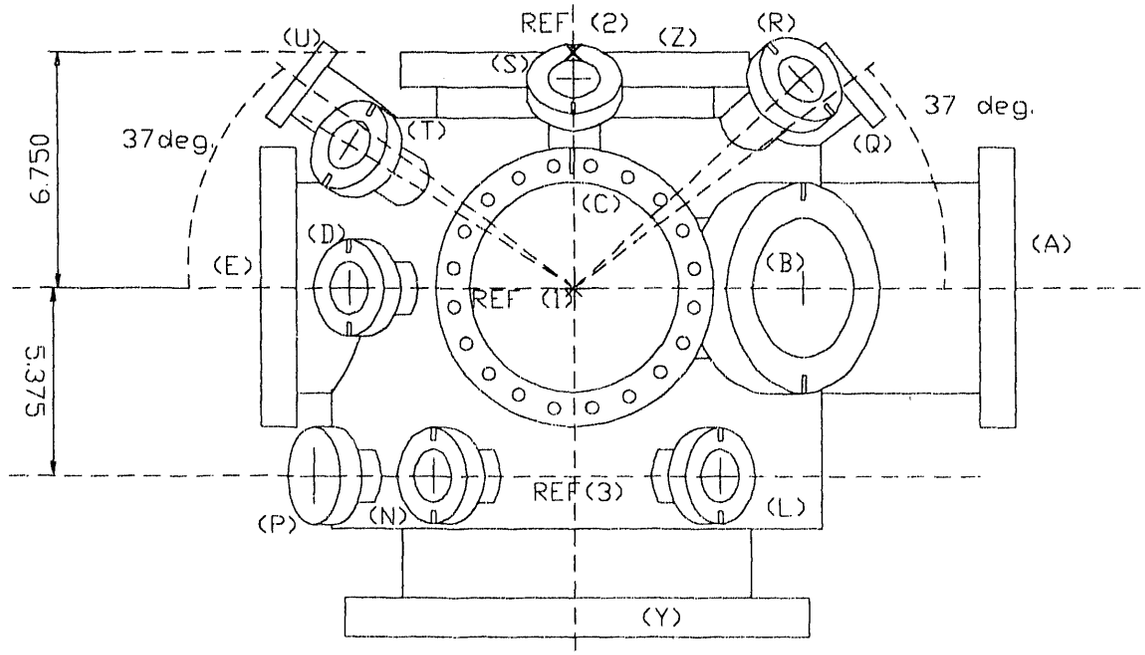
REF (2)
(U)
(Z)
(R)
(S)
37 deg.
37deg.
(T)
(Q)
6.750
(C)
(D)
(A)
(E)
(B)
REF (1)
5.375
REF (3)
(P)
(N)
(L)
(Y)

(c)

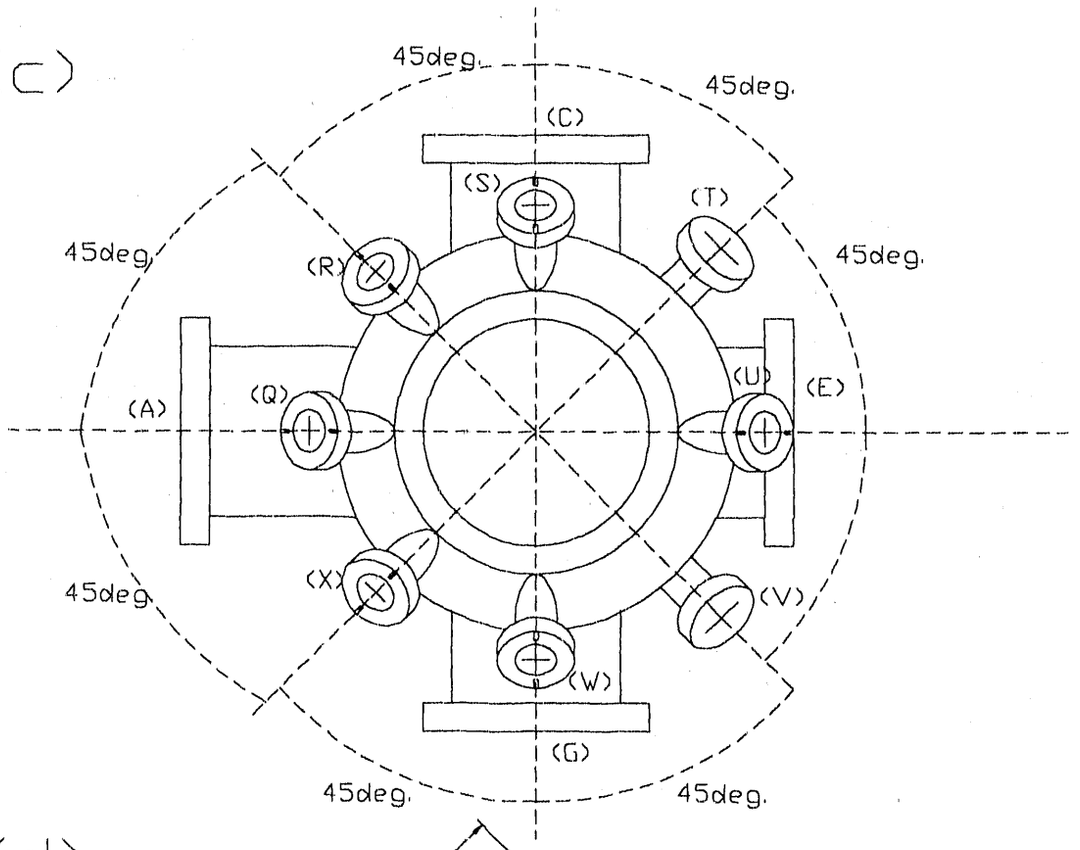
45deg.
45deg.
45deg.
45deg.
45deg.
45deg.
45deg.
(C)
(S)
(T)
(R)
(A)
(Q)
(U)
(E)
(X)
(V)
(W)
(G)

(d)

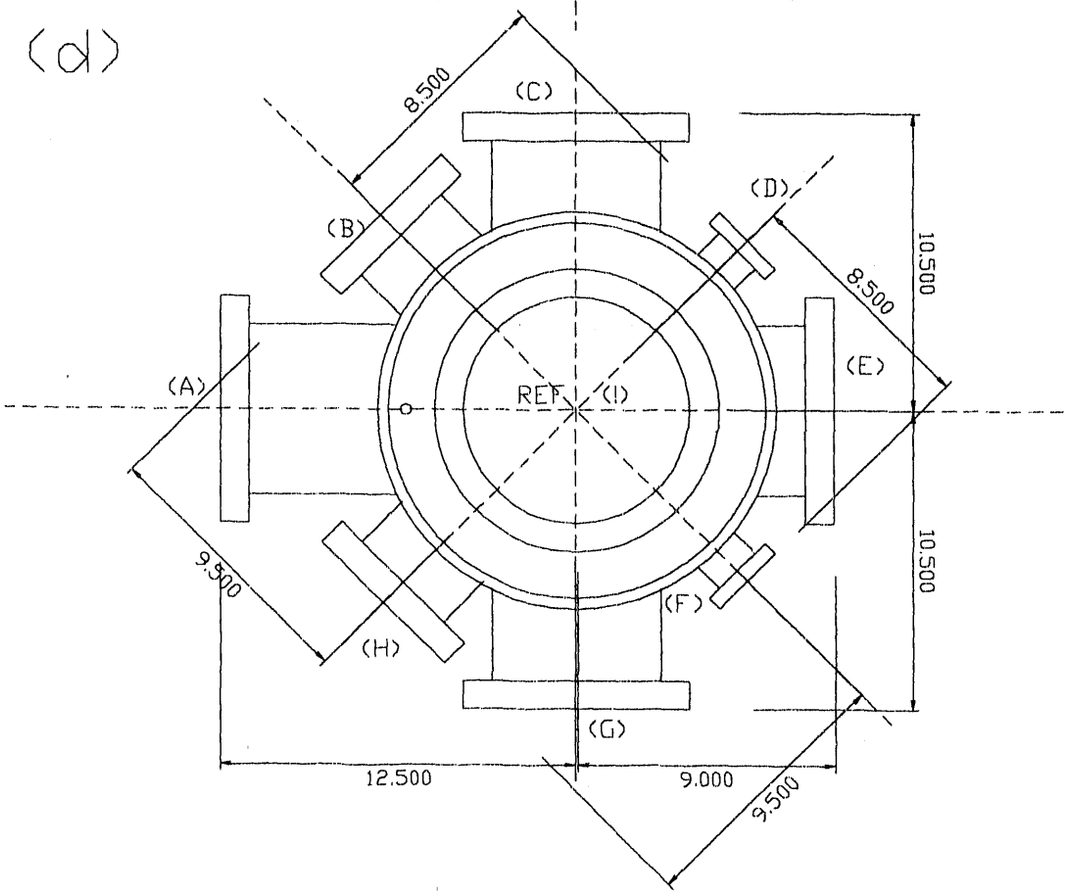
8.500
(C)
(D)
(B)
10.500
8.500
(A)
REF
(I)
(E)
9.500
10.500
(F)
(H)
(G)
12.500
9.000
9.500

Table 3.1: Specifications for UHV chamber shown in Fig. 3.8. The chamber was made of type 304 non magnetic stainless steel, then chemically etched and helium leak tested for 10^{-11} torr use. The overall height of the chamber was 16.625 inches. Port specifications refer to individual ports in Fig. 3.8. There are three levels of flanges on the chamber as indicated by REF. 1, 2, and 3 on the figure. The distances and angles specified for each flange are given with respect to one of these reference points. The distance, (in inches, $\pm$ 0.02"), from each flange face to the chamber center(CC) reference point listed in column 3, is denoted "dist. to CC". Angle 1 represents the angle of each flange with respect to the plane of flanges A-C-E-G. Angle 2 represents the angle of each flange with respect to the plane of flanges A-E-Y-Z. Flange type indicates whether the flange is rotatable (R) or nonrotatable (N). Diagnostic type indicates the type of instrument or flange associated with each port. Windows were non-magnetic with the exception of the quartz windows (Q) used for UV optical experiments.

• port	fl. diam. (in.)	C.C. ref. pt	dist. to CC (in.)	angle 1 (deg)	angle 2 (deg)	flange type	diagnostic type
A	8.00	REF 1	12.50	0.0	0.0	N	time of flight
B	6.00	REF 1	9.50	0.0	45.0	N	window (Q)
C	8.00	REF 1	10.50	0.0	90.0	N	L.T. manip.
D	2.75	REF 1	8.50	0.0	135.0	N	window
E	8.00	REF 1	9.0	0.0	180.0	R	LEED/Auger
F	2.75	REF 1	8.50	0.0	225.0	N	window
G	8.00	REF 1	10.50	0.0	270.0	N	Mass spec.
H	6.00	REF 1	9.50	0.0	315.0	N	window (Q)
J	2.75	REF 3	8.50	0.0	225.0	N	leak valve
K	2.75	REF 1	11.25	-37.0	315.0	R	window (Q)
L	2.75	REF 3	8.50	0.0	60.0	N	blank
N	2.75	REF 3	8.50	0.0	120.0	N	gate valve
P	2.75	REF 3	8.50	0.0	150.0	N	ion gauge
Q	2.75	REF 1	10.00	37.0	0.0	N	blank
R	2.75	REF 1	10.00	37.0	45.0	N	ion gauge
S	2.75	REF 1	10.00	37.0	90.0	R	cold tip/blank
T	2.75	REF 1	10.00	24.0	135.0	N	window
U	2.75	REF 1	10.00	37.0	180.0	N	blank
V	2.75	REF 1	10.00	24.0	225.0	N	window
W	2.75	REF 1	10.00	27.0	270.0	N	ion gun
X	2.75	REF 1	10.00	37.0	315.0	N	window (Q)
Y	13.25	REF 1	9.875	-90.0	0.0	N	pump stack
Z	10.00	REF 1	6.75	90.0	0.0	N	R.T. manip.

Figure 3.9 The low temperature manipulator designed for the experiments in this thesis is shown. The sample mount was attached to a liquid helium cryostat equipped with an x-y-z translation flange for ease of alignment. The mount accommodated up to seven samples, and was temperature controlled using a Lakeshore Cryogenics feedback temperature controller . A fiberglass sheathed nichrome wire wrapped around the sample rod served as a heater. A minimum temperature of 12 °K was obtained with temperature fluctuations of approximately 0.2 °K over the length of a grating scan. The temperature was monitored by two silicon thermometers using a four-lead resistance measurement.

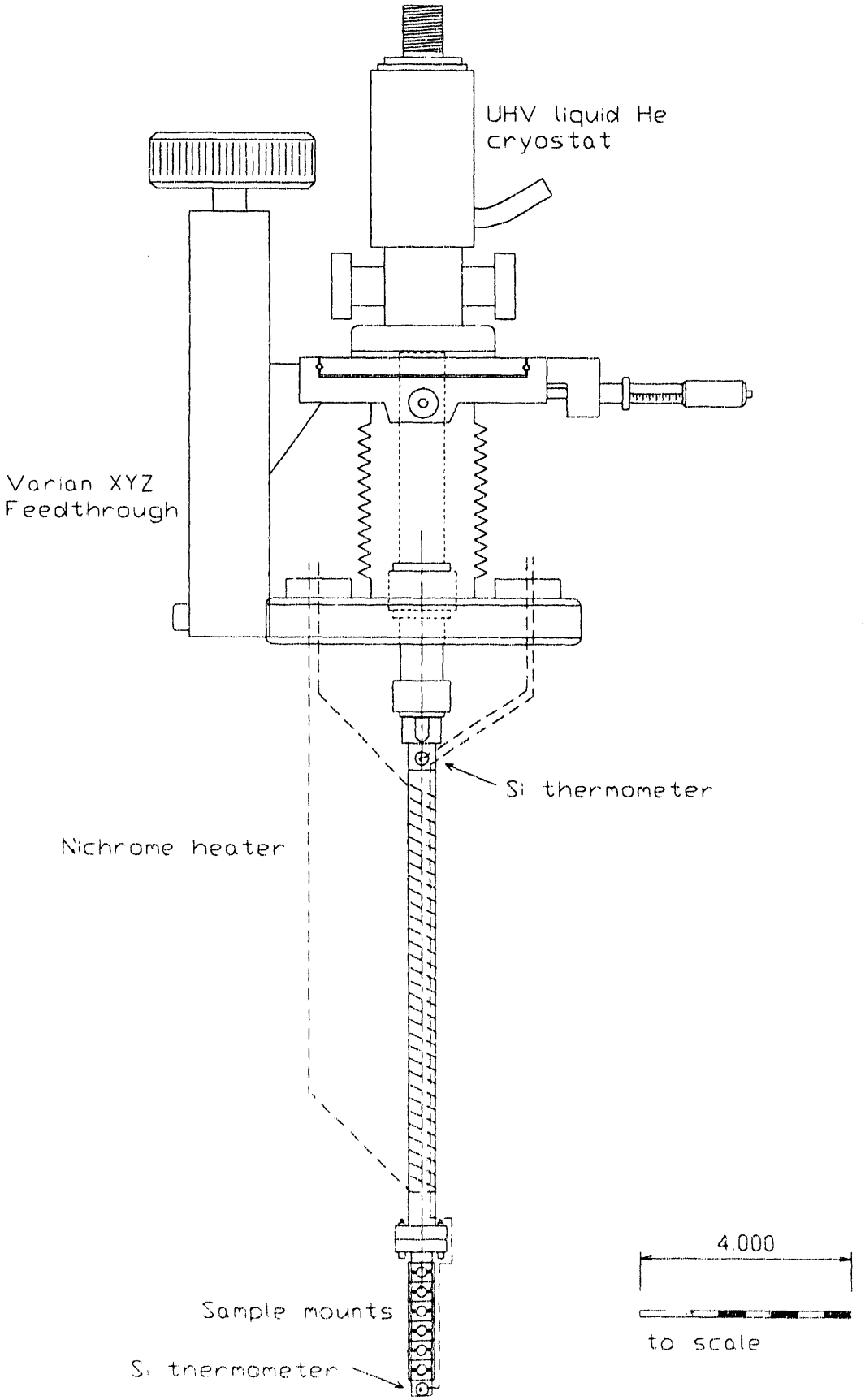
UHV liquid He
cryostat
Varian XYZ
Feedthrough
Si thermometer
Nichrome heater
4.000
Sample mounts
Si thermometer
to scale

silicon diodes (thermometers) using a four-lead resistance temperature measurement method. There was less than a 0.5 °K drop in temperature between either end of the 13 inch rod at 20 °K. The temperature was maintained using a Lakeshore Cryogenics feedback temperature controller to vary the temperature. A fiberglass sheathed nichrome wire wrapped around the sample rod served as a heater. A minimum temperature of 12 ° K was obtained with temperature fluctuations of approximately 0.2 °K over the length of a grating scan.

Data was taken over a range of temperatures from 12 to 300 °K. Multiple scans of the delay line were averaged to improve signal to noise. The same baseline was obtained after each scan, demonstrating that no irreversible damage had occurred. In addition, a power-dependence study showed the diffracted signal to be linear in the intensity of each of the excitation and probe beams by over one and a half orders of magnitude in signal intensity.

4. RESULTS AND DISCUSSION

4.1 Confirmation of a Thermomechanical Signal

When GaAs is excited by photons with energies greater than the band gap energy (1.43 eV), electrons are excited out of the conduction band and into the valence band. The three transitions allowed for a 2.00 eV pump pulse on the GaAs(100) surface are shown in Fig. 1.3. Electrons can be excited from the heavy hole, light hole and split-off valence bands into the conduction band Γ-valley. The creation of electron-hole pairs produces a change in the dielectric function ε, which can be described at low intensities by the Drude model since the excitation wavelength is relatively near the band edge. Single color pump-probe measurements at 2 eV show a rapid absorption saturation transient on the order of 100 fs due to electronic carriers scattering out of their initial excited state and assuming a broad energy distribution.[69] Experiments performed with a UV pump and visible probe (exactly the opposite of the experiments presented here), exhibited similar electronic effects.[70,71] This excited distribution relaxes to the conduction band minimum via carrier-carrier scattering on a 1-2 ps time scale, or if the electrons have greater than 500 meV of excess energy they can interband scatter to the adjacent X and L valleys. The relaxation of these carriers results in the transfer of heat from the carrier distribution to the lattice phonons. This creates a nonequilibrium phonon distribution which equilibrates within approximately 3 ps at 300 °K and 10 ps at 10 °K.[52] Radiative recombination brings the electrons back to the valence band within 1 ns to 1 μs, depending on the carrier density excited in the medium.[72]

Our 2 eV excite/4 eV probe data shows no evidence of the electronic effects discussed above; instead we see a 30-33 ps rise time which we attribute to the thermal expansion of the GaAs perpendicular to the plane of the surface. The signal decays to

the 1/e point within 150-160 ps due to conduction of heat away from the surface as shown in Fig. 4.1. Since the 4 eV light probes a set of ground states further down the valence band edge than were initially excited by the 2 eV grating (Fig. 1.3), electronic effects, such as interband saturation and intervalley scattering, have a negligible effect on the probe beam. Thus the diffracted signal arises solely from density changes at the surface created by heat transfer from the carriers to the lattice phonons and their subsequent equilibration. These results and the technique used are fundamentally different from the electronic experiments previously reported in the literature.

Figure 4.1 shows representative data taken on n-type (Si, 1×10^{18} cm^{-3}) and p-type (Zn, 6×10^{18} cm^{-3}) samples at 300 °K. As can be seen, the differences in the rising edge and decay of the data are within the experimental noise. The signal from the n-type sample rises to a maximum within 31 ps, and decays to the 1/e point within 156 ps, while the signal from the p-type sample rises in 33 ps and decays in 150 ps. Only two curves are displayed for ease of viewing, however similar results were also obtained for undoped samples and different dopant concentrations (i.e., Si, 1×10^{17} cm^{-3} and Zn, 3×10^{19} cm^{-3}).

If the signal observed were due to electronic effects, a change in the optically induced carrier density, dopant type (i.e. electrons vs. holes), or dopant concentration would affect the carrier transport and thus the temporal nature of the signal. Kash and Tsang have verified this by measuring the rise and decay rate of the hot phonon population in GaAs as a function of these parameters.[52] They found that the nonequilibrium decay rate in GaAs decreased as the carrier density increased, going from 8 ps to 4 ps, as the carrier density increased from 10^{16} cm^{-3} to 10^{17} cm^{-3}. The nonequilibrium phonon population was also found to be much smaller in the p-type sample, because the cold (doped) holes provided an additional mechanism for the initial cooling of the injected electrons by electron-hole scattering. This reduced the phonon lifetime to approximately 2 ps. Transient absorption studies of the effect of variations in

Figure 4.1 Transient grating (TG) diffraction intensity versus probe delay time is plotted for data taken on n-type (Si, 1×10^{18} cm^{-3}) and p-type (Zn, 6×10^{18} cm^{-3}) GaAs(100) samples at 300 °K. Part (a) shows a high resolution scan of the diffracted signal rising edge dominated by transient thermal expansion. The signal from the n-type sample rises to a maximum within 31 ps, while the signal from the p-type sample rises in 33 ps. Part (b) shows the signal decay due to thermal diffusion into the bulk. The signal decays to the 1/e point within 156 ps for the n-type sample and within 150 ps for the p-type sample. Differences in the rising edge and decay of the data are within the experimental noise, verifying that the phenomena is truly thermomechanical in nature.

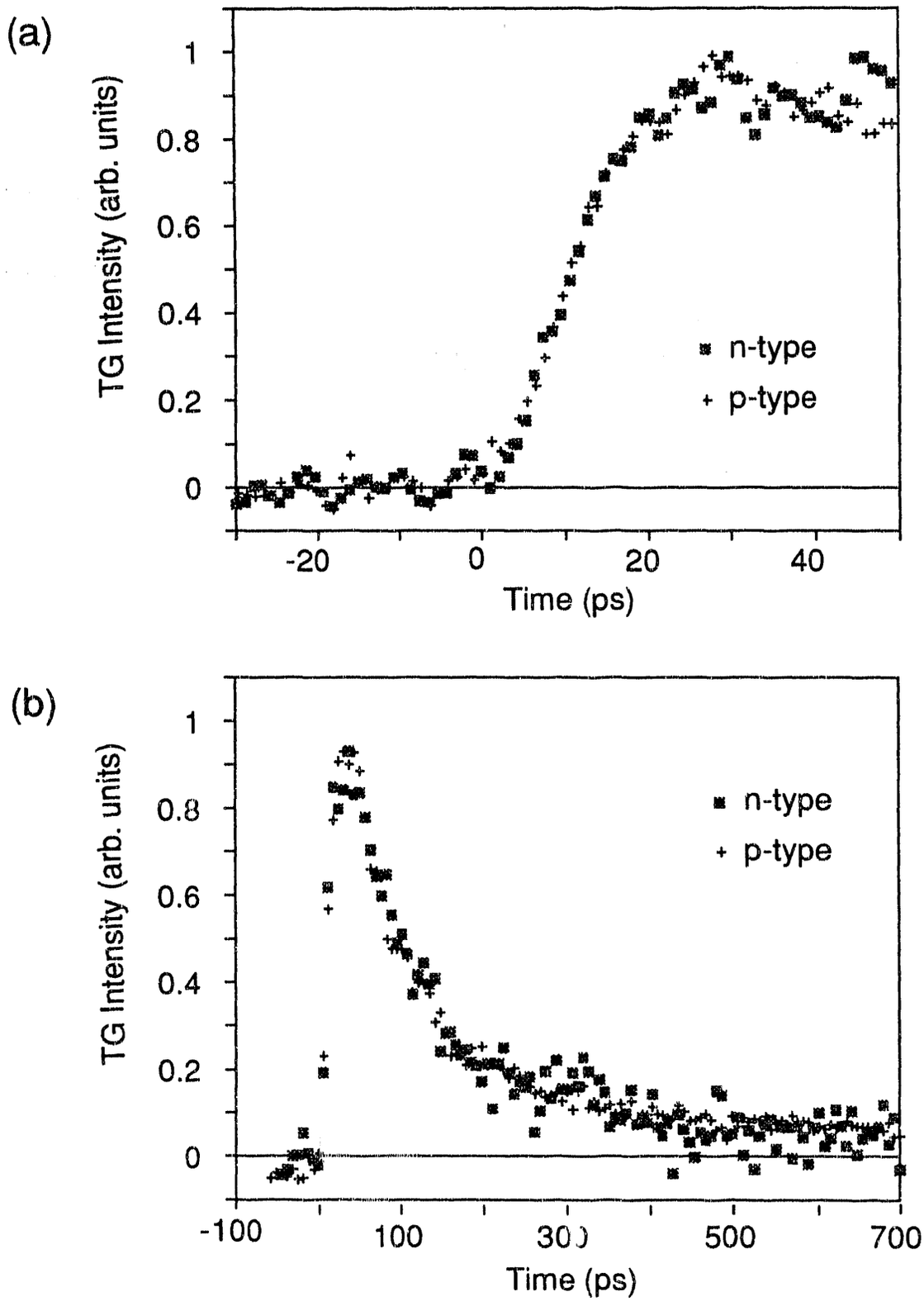
(a)
TG Intensity (arb. units)
1
0.8
0.6
0.4
0.2
0
-20
0
20
40
Time (ps)
n-type
p-type
(b)
TG Intensity (arb. units)
1
0.8
0.6
0.4
0.2
0
-100
100
300
500
700
Time (ps)
n-type
p-type

the optically induced carrier density corroborate these results.[69,73] We did not observe a significant change (i.e., > 7%) in the either the rise or decay constants of our signal as the dopant type and concentration were changed. Nor did we observe a change in the time dependence of the signal as the excitation density was varied over an order of magnitude.

We also do not observe any measurable change in the time-dependence of the signal by simultaneously rotating the polarization of the excitation pulses (Fig. 4.2). Since the light and heavy hole bands are not perfectly isotropic, optical transitions from these states give rise to an anisotropic momentum distribution, the decay of which is polarization dependent. Thus an electronically derived signal should be affected by the incident light polarization.[30,47] The above results confirm our belief that the phenomena observed is truly thermomechanical in nature.

Figure 4.2 Transient grating (TG) diffraction intensity versus probe delay time is plotted for data taken on a p-type (Zn, 6×10^{18} cm^{-3}) GaAs(100) sample at 300 °K. Part (a) shows the diffracted signal with the excite and probe beams of like polarization. Part (b) shows the diffracted signal with the excite and probe beams polarized perpendicular to each other. Differences in the data are within the experimental noise, verifying that electronic state filling is not influencing the signal.

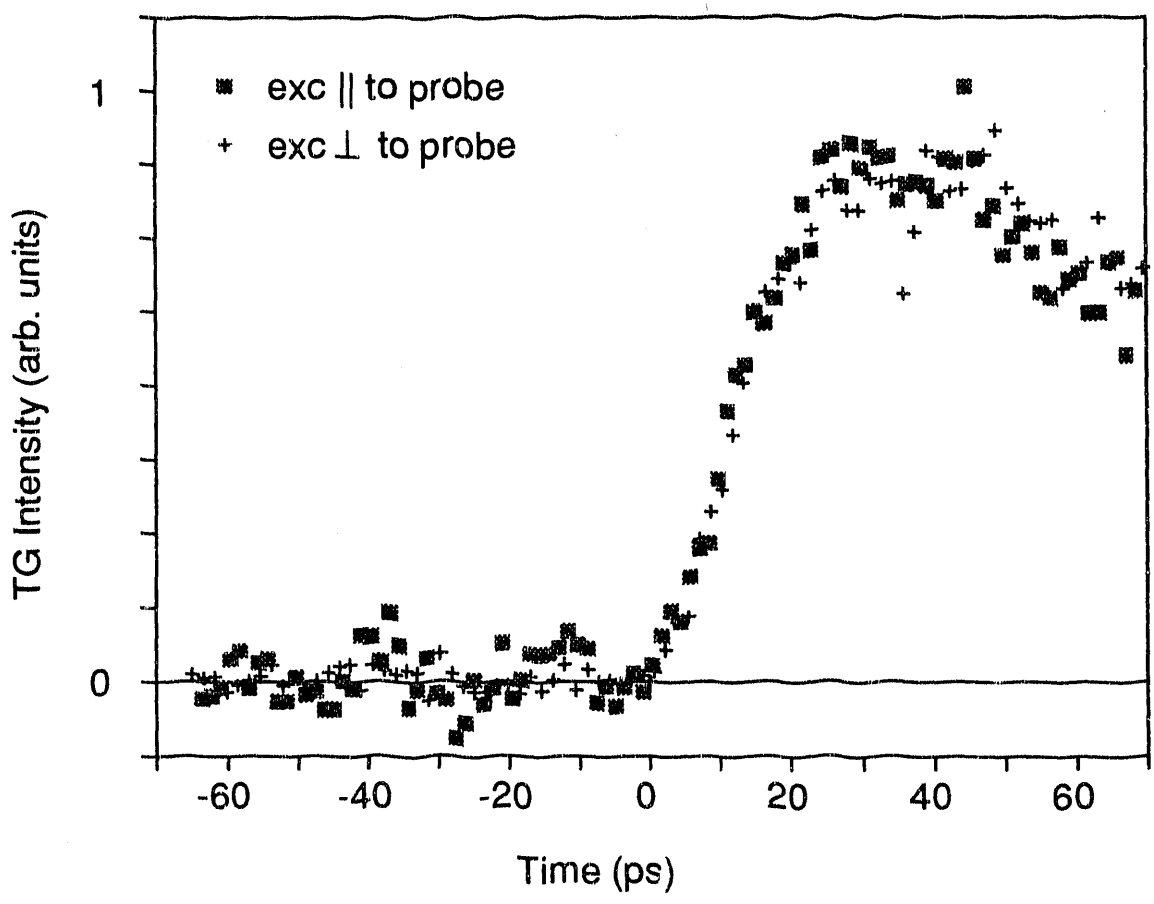
exc || to probe
exc ⊥ to probe
TG Intensity (arb. units)
1
0
-60
-40
-20
0
20
40
60
Time (ps)

4.2 Signal Contributions

The diffracted signal is composed of four components: thermal expansion of the surface and heat flow away from the surface into the bulk, and expansion and diffusion of heat in the plane of the surface. We can estimate the magnitude of the parallel and perpendicular contributions to the signal using simple back-of-the-envelope type calculations. As discussed in Chapter 2, the effective rising edge can be approximated as $(1 - e^{-t/\tau_{eff}})$, where τ_{eff} is the effective time constant. The contributions from the perpendicular and parallel components are $\tau_{\perp}$ and $\tau_{\parallel}$ respectively. The effective time constant due to both can thus be written as

$$\tau_{eff} = \frac{1}{\sqrt{\tau_{\perp}^{-2} + \tau_{\parallel}^{-2}}} . \qquad (4.1)$$

This is experimentally determined to be 15 ps, corresponding to the 1/e point in the rise. The time constant for the expansion contribution perpendicular to the surface can be estimated from the expression

$$\tau_{\perp} = (\alpha_{exc}\, v_s)^{-1} = 14 \text{ ps.} \qquad (4.2)$$

Again, this corresponds to the 1/e point in the rise. The parallel expansion is expected result in to a rising edge with a time constant of

$$\tau_{\parallel} = f/2v_s = 37 \text{ ps.} \qquad (4.3)$$

A comparison of the individual contributions indicates that the signal is dominated by the perpendicular expansion in the 5-10 μm fringe spacing range. The parallel contribution contributes less than 7% to the overall rise.

The decay constant corresponding to the 1/e point in the decay is experimentally determined to be 156 ps for diffusion of heat into the surface. The corresponding parallel

thermal flow would be expected to lead to a 3 ns $\left(= \frac{(f/2\pi)^2}{D} \right)$ decay of the signal. As can be seen from the data, the rise and fall are both dominated by the effect of phenomena perpendicular to the surface. Because of the large fringe spacing used in these experiments, we expect the influence of the parallel expansion component to be negligible. This is illustrated in Fig. 4.3. The effect of parallel phenomena is observable because the movement of the surface or of heat perpendicular to the grating fringe spacing washes out the grating structure on a particular time scale. The mean thermal diffusion distance in GaAs is 1 μm, thus on the time scale of our measurements the heat will have propagated only one fifth of the way to the next grating fringe, reducing the contribution of the parallel thermal expansion to the diffracted signal to less than 5%. This was verified by performing experiments over a range of grating fringe spacings (5-10 μm) with no measurable effect on the signal.

In many materials it would be possible to measure the parallel expansion of the surface. To resolve this, the grating fringe spacing must be on the order of or less than the skin depth of the excitation beams. In GaAs this requires a fringe spacing of << 1 μm. This unfortunately leads to a signal decay due to thermal diffusion in the plane of the sample on the order of the thermal expansion rise time, making the parallel versus perpendicular expansion difficult to resolve in GaAs. In general, this limitation is not present in all materials, and the prediction of using transient gratings to time resolve parallel versus perpendicular expansion should be possible. This would also require a more thorough theoretical approach, namely expanding the analysis to three dimensions.

It is interesting to note that there is no evidence of acoustic waves in our data. When the lattice responds to the deposition of heat, thermal expansion occurs simultaneously with the launching of acoustic waves throughout the lattice. In a transient grating experiment these acoustics appear as a periodic sinusoidal pattern superimposed on the diffracted signal. Given the parameters of our experiment, we would expect to see

Figure 4.3 The mean thermal diffusion distance in GaAs is 1 μm on the time scale of our experiments. For large fringe spacing, the heat will not propagate far enough to wash out the adjacent fringes of the grating. Thus the transient grating diffraction signal will be dominated by perpendicular expansion and thermal diffusivity. At small fringe spacings however, the grating signal will have contributions from phenomena occurring both parallel and perpendicular to the fringes.

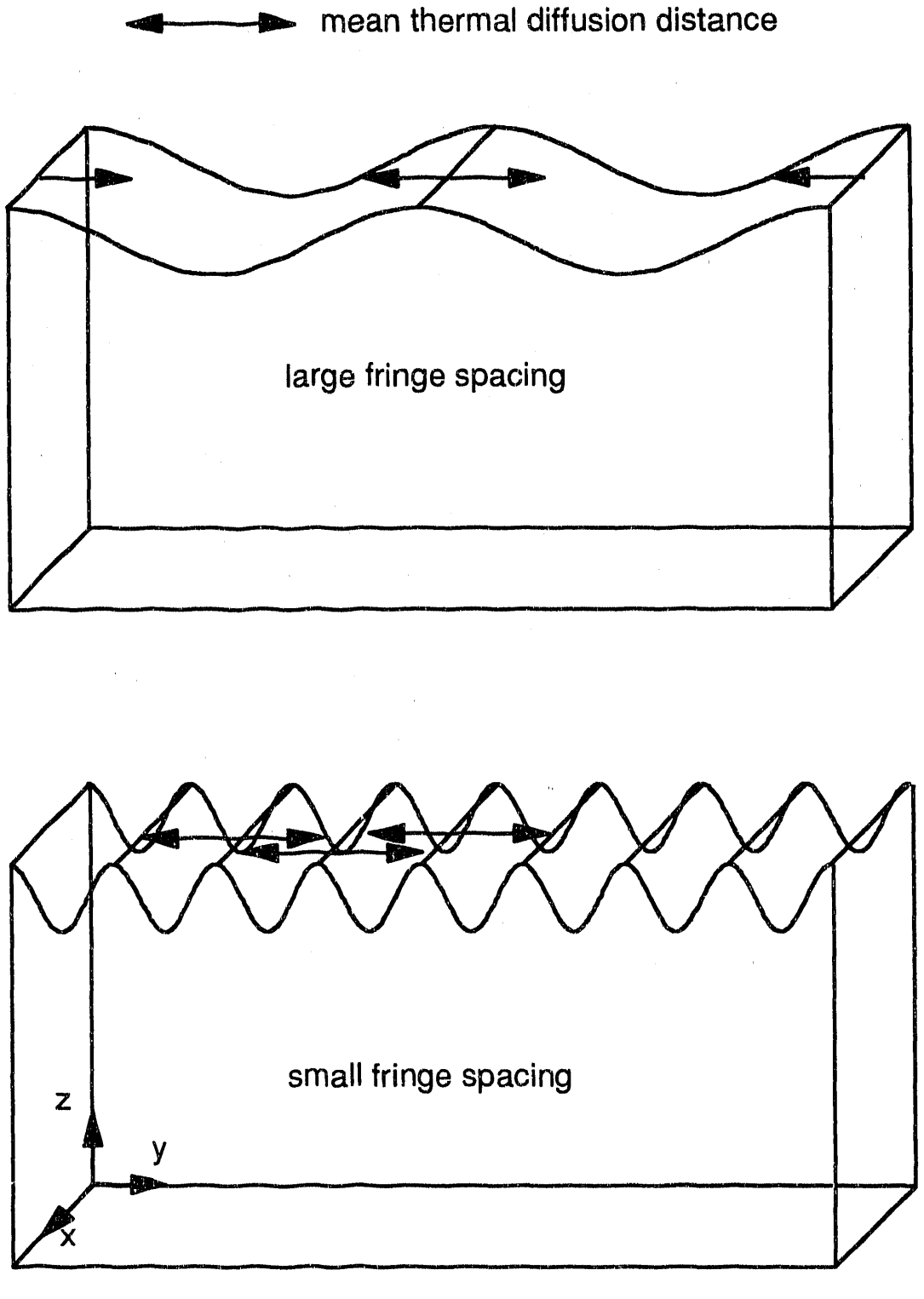
mean thermal diffusion distance
large fringe spacing
small fringe spacing
z
y
x

acoustics with a period $\tau_{ac} = f/2v_s = 500$ ps. The absence of acoustic oscillations indicates we are not exciting coherent acoustic wave guide modes in the sample. This is probably due to poor overlap of the acoustic modes of the sample with the excitation profile.[13]

It is commonly believed that acoustic oscillations are the signature of a thermally-induced signal. However, the absence of these oscillations has recently been observed by others.[32] It has been shown that one can make a smooth transition from a region where there is significant acoustic amplitude to a region where there is virtually no acoustic amplitude to the transient grating thermal signal by varying the grating fringe spacing. This is due to a change in the spatial overlap between the acoustic pattern and the grating excitation profile. In this case, Marshall et. al. found that by signal averaging for several hours, minute acoustic oscillations did become discernible. This is probably the case for our experiments as well, but we were unable to verify the existence of acoustics. This was partially because our signal was over two orders of magnitude smaller than theirs. Also, in order to resolve such small scale oscillations a delay line of sufficient length to observe several acoustic periods is required.

4.3 Data Modeling

Figure 4.4 shows a representative data set for n-type GaAs (Si, 1×10^{18} cm^{-3}) with a one adjustable parameter least squares fit to the data using the detailed model described in Chapter 2. The insert in Fig. 4.4 shows a high resolution data scan of the rising edge taken immediately after the long time scan shown in the main part of the figure. Both data sets were taken on the same sample on the same spot, with the same fringe spacing and laser excitation density, in order to assure their comparability. The rising edge was determined to be solely due to thermal expansion.

Figure 4.4 Transient grating (TG) diffraction intensity versus probe delay time is plotted for data taken on a p-type (Zn, 6×10^{18} cm^{-3}) GaAs(100) crystal at 300 °K. The smooth line through the data is a one adjustable parameter fit to the data using the model described in Chapter 2 and parameters in Tables 4.1 and 4.2. The insert shows a high resolution scan of the rising edge due to thermal expansion with the same theoretical fit. The single adjustable parameter in the fit is $\alpha_{exc} = 1.5 \times 10^5$ cm^{-1}, the optical absorption coefficient at the excitation wavelength.

(a)

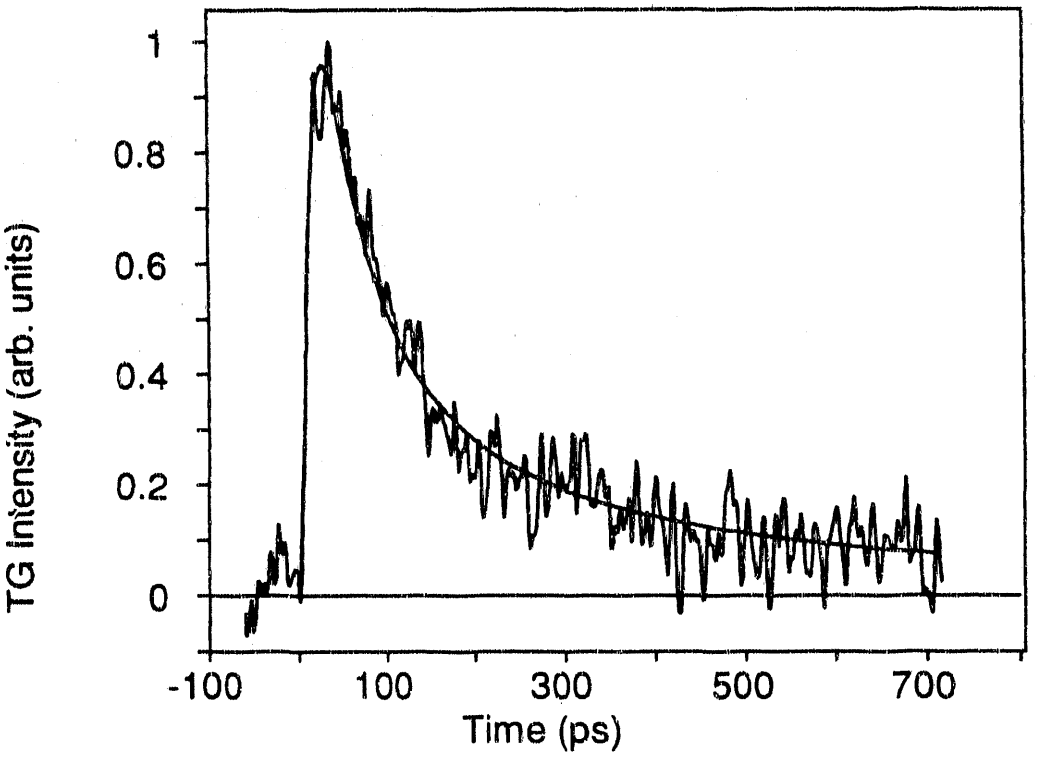
TG Intensity (arb. units)
1
0.8
0.6
0.4
0.2
0
-100
100
300
500
700
Time (ps)

(b)

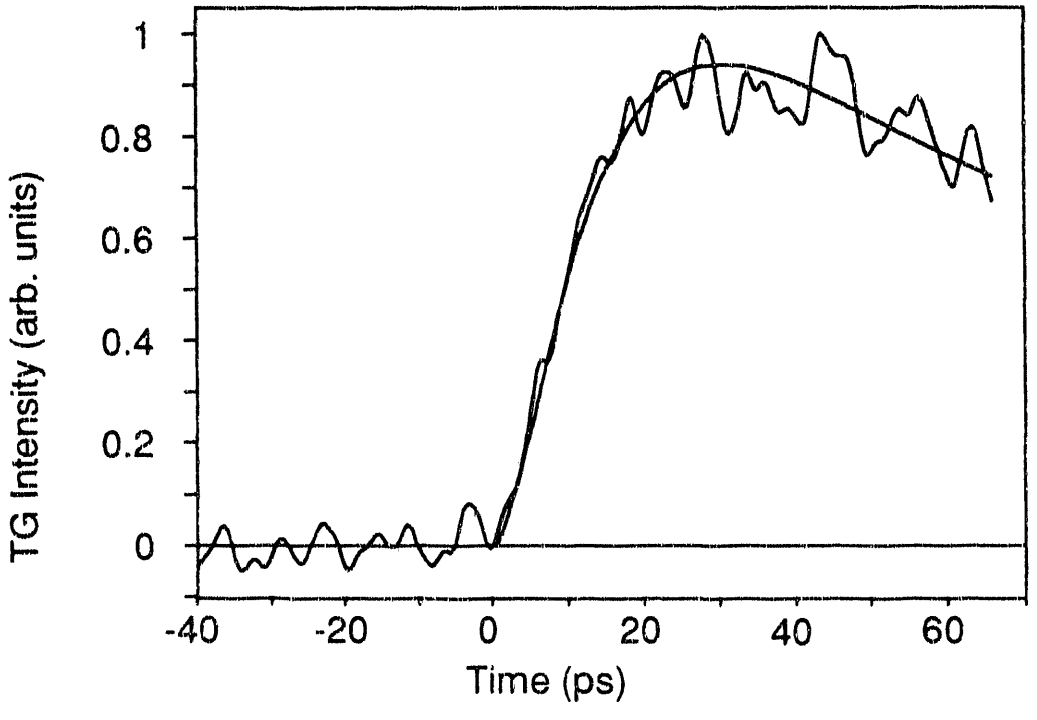
TG Intensity (arb. units)
1
0.8
0.6
0.4
0.2
0
-40
-20
0
20
40
60
Time (ps)

Table 4.1 Selected physical constants for GaAs at 300 °K. Note that some properties are quite rapid functions of temperatures. The numbers listed below are specific for 300 °K.

Lattice constant	5.65325	Å	74
Molecular weight	144.642	g	43
Crystal density, ρ	5.3174	g/cm^3	75
Velocity of sound, v_s (in (100) longitudinal wave propagation direction)	4.731	10^5cm/s	76
Bulk modulus, B	75.5	10^{10} dyn/cm^2	43
Melting temperature, T_m	1513	°K	77
Effective Debye temperature, θ_d	360	°K	78,79
Linear expansion coefficient, γ	6	10^{-6}/°K	75
Specific heat at constant pressure, C_p	0.327	J/g°K	43
Lattice thermal conductivity, κ	0.455	W/cm°K	79
Static dielectric constants, ε_0	12.85		80
and ε_∞	10.9		
Index of refraction at 620 nm, n_{exc}	3.878		80
Index of refraction at 310 nm, n_p	3.601		80
Normal-incidence reflectivity at 620 nm, R	34%		80
Direct intrinsic band gap energy, E_g	1.43		43

Table 4.2 Comparison of the experimental parameters used to model the transient grating diffraction efficiency in Figures 4.4, 4.6, and 4.7,and the corresponding literature values calculated from parameters given in the references listed. Dashed lines indicate the 300 °K value was used in the calculation.

	Temperature			Reference
	300 °K	50 °K	20 °K	
Bulk Thermal Diffusivity in literature (D_b, cm^2/s)	0.4 -0.75	8 - 20	75 - 188	[81, 82, 83]
Surface Thermal Diffusivity used in calculation, (D_s, cm^2/s)	1.0	19.9	3.7	This work
Excitation absorption constant in literature (α_{exc}, cm^{-1})	4.3×10^4	---	---	[80]
Excitation absorption constant in calculation (α_{exc}, cm^{-1})	1.4×10^5	1.4×10^5	1.4×10^5	This work
Probe absorption constant (α_p, cm^{-1})	7.78×10^5	---	---	[80]

The theoretical fits shown for both data sets were calculated using identical parameters. Constants used in the calculation for GaAs at 300 °K are shown in Tables 4.1 and 4.2. The theoretical calculations were performed on a UNIX based DEC 3100 RISC workstation with 16 MB of memory using the computer codes in the Appendix of this thesis. The code consists of a numerical integration routine which calculates the transient grating diffracted signal intensity using the equations developed in Chapter 2. The solution of the temperature profiles in the sample as a function of time and absorption depth into the sample are calculated analytically using Eqn. 2.33. The absorption profiles was used in calculating the theoretical fit to the data in Fig. 4.4 are shown in Fig. 4.5. A single theoretical fit and the associated heat profiles can be produced using the code HFCALC2A.C. This is a numerical integration routine that calculates the transient grating experimental observable. To find the best possible parameter set for the data, an interactive fitting routine HEATFIT.C was developed. The fitting routine calculates a least squares fit for up to five parameters. The normalized height of the curve is always one of these parameters. Calculations were performed varying the thermal diffusivity, the optical absorption constant of both the excite and probe beams, and the magnitude of the acoustic amplitude, individually and simultaneously in different combinations.

The phenomena we are probing is due to absorption at the excite wavelength. Thus variation of the probe optical absorption coefficient has essentially no effect on the calculated diffracted signal. Variation of the thermal diffusion constant primarily influences the signal decay. This is important as our analysis is based on the assumption that the expansion signal is fast relative to the diffusion of the heat away from the surface. The absorption coefficient at the excite wavelength, however, has a pronounced effect on the signal rise, as well as a somewhat less dramatic influence on the decay. A large α_{exc} results in a sharp rising edge, which decays with a much slower time constant. The effect of varying α_{exc} on the decay is subtly different than a change in the diffusion

Figure 4.5 Spatial thermal profiles used to calculate the theoretical curve in Fig. 5.2. Increase in temperature above the equilibrium value in the grating peaks is plotted versus absorption depth in the sample. The six curves correspond to delay times of 12, 92, 172, 332, 492, and 652 ps after the initial thermal excitation.

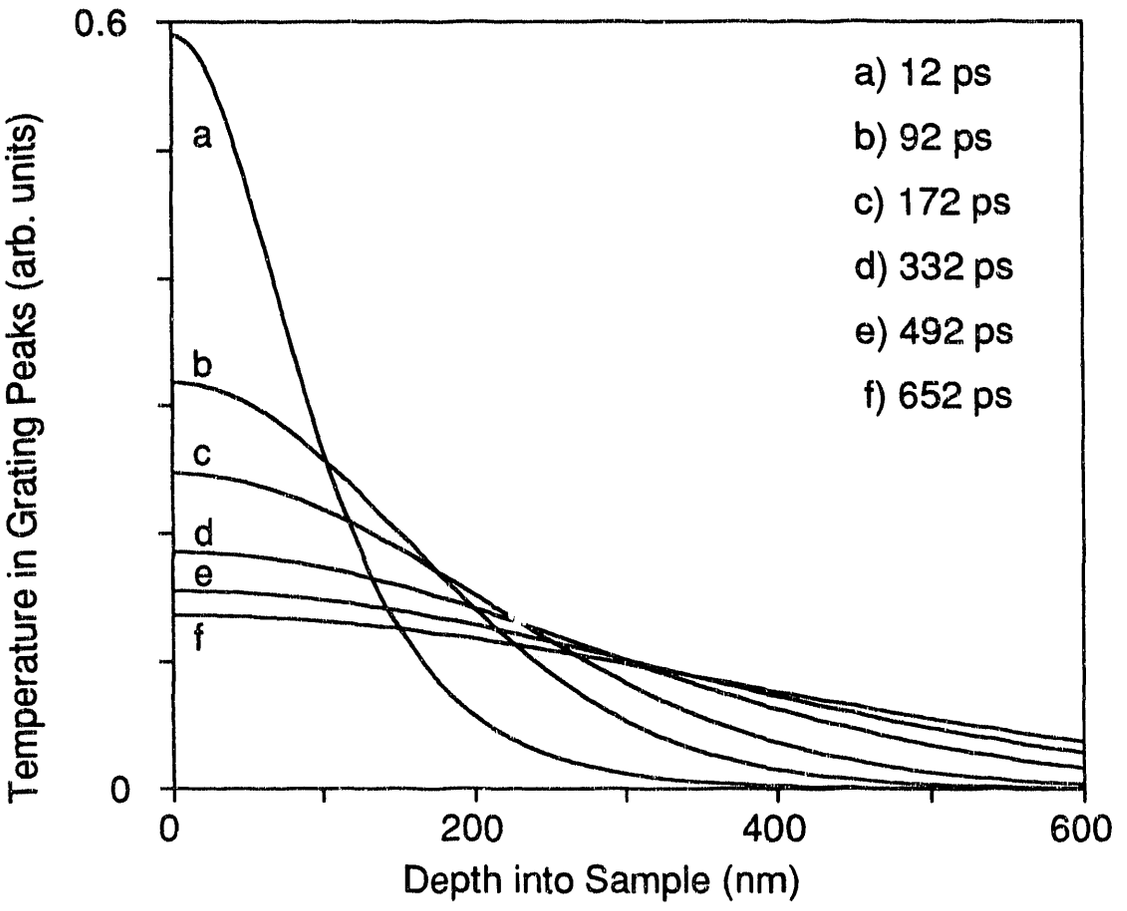
0.6
0
Temperature in Grating Peaks (arb. units)
a) 12 ps
b) 92 ps
c) 172 ps
d) 332 ps
e) 492 ps
f) 652 ps
a
b
c
d
e
f
0
200
400
600
Depth into Sample (nm)

constant. While D actually changes the shape, or inflection, of the decay curve, α_{exc} simply raises or lowers the height of the calculated decay relative to the data, without significantly changing the shape. Attempts to model the expansion and thermal diffusion separately resulted in values of D and α_{exc} over an order of magnitude larger than literature values at room temperature. Thus, in order to fit the data accurately, both parameters must be varied simultaneously.

The final parameter varied was the acoustic amplitude, A_{ac}, given in Eqn. 2.24. This represents the magnitude of the acoustic contribution to the time-dependent strain in Eqn. 2.22. The parameter was normalized with respect to the overall equation, then the value was varied between zero and one. For all the calculations presented here, the acoustic amplitude was set to zero ($A_{ac} = 0$). This is consistent with the lack (or minute amplitude) of acoustic oscillations in the data. Attempts use a non zero amplitude resulted in a several hundred femtosecond component of the rising edge, which is clearly inconsistent with our experimental observations.

In order to obtain a good match to the data, it was necessary to use a value for the surface diffusivity, D_s, slightly above the upper limit of the range of literature values for the bulk diffusivity, D_b. The other adjustable parameter in the fit was the absorption coefficient at the excitation wavelength, $\alpha_{exc} = 1.5 \times 10^5$ cm^{-1}. This value is four times larger than the literature value for pure bulk GaAs. The experimentally determined value of α_{exc} results in an optical absorption depth of 65 nm at the pump wavelength, while the probe penetrates to only 13 nm. In order to evaluate the magnitude of the surface selectivity it is useful to define an effective grating depth for the surface component of the signal. The excitation is initially deposited with a Beer's absorption depth profile, which equilibrates with sufficient rapidity to appear uniform to the probe. The grating excitation can therefore be assumed to be uniform, i.e., $\Delta\varepsilon(z) \approx \Delta\varepsilon_0$, where $\Delta\varepsilon_0$ is a constant. The effective grating surface probe depth (at the 50% absorption point) can then be defined as the center of mass in the z-direction of the reflected grating signal:

$$z\delta^2 = \frac{|\sqrt{\eta_z}|^2}{\eta} \quad . \tag{4.4}$$

Here η is the reflected diffraction efficiency of the probe. Substituting $\Delta\varepsilon_0$ into Eqn. 2.7 and solving for η yields[35]

$$z\delta^2 = \frac{\lambda}{4\pi\sqrt{n^2 + k^2}} \quad . \tag{4.5}$$

Thus the reflected diffracted signal is essentially generated within the first 6 nm of the surface, i.e., the first 10 atomic layers.

Figure 4.5 shows an example of the absorption of the excitation beams as a function of time and depth into the surface. The rough estimate of the maximum temperature rise of the lattice associated with this absorption, which in turn gives rise to our expansion signal, is given by

$$T = \frac{E}{A\,\delta\,\rho\,C} \approx 100\ ^\circ\text{K}. \tag{4.6}$$

Here E is the absorbed laser energy, A is the spot size, δ is the literature value for the optical absorption depth at the excite wavelength, ρ is the density, and C is the specific heat at constant pressure. The maximum temperature corresponds to a maximum *net* perpendicular displacement of the surface of

$$T\,\gamma\,\delta \approx 1\ \text{Å}, \tag{4.7}$$

where $\gamma = 6 \times 10^{-6}/^\circ\text{K}$ is the linear expansion coefficient for bulk GaAs. Assuming this displacement is uniformly distributed throughout the optical excitation absorption depth, this corresponds to an average displacement per atomic layer of (1 Å/400 atomic layers) = 0.002 Å, or 0.04%. It is the sum of these individual displacements which gives rise to the overall net displacement calculated in Eqn. 4.7. This is of course an average

estimate, as the surface atomic layers are expected to have a larger displacement than those 400 layers into the bulk.

4.4 Temperature-Dependent Results

Temperature-dependent data was taken for a p-type sample with a Zn dopant concentration of 6×10^{18} cm^{-3}. This sample was chosen because literature values exist for the bulk diffusivity as a function of temperature for GaAs with this dopant type and concentration.[81] Figure 4.6 shows data taken at 300, 50, and 20 °K. The solid lines through the data are theoretical fits calculated using the model in Chapter 2 with the parameters appropriately adjusted for temperature. These parameters are given in Tables 4.1 and 4.2. The material band gap energy increases approximately 35 meV as the temperature decreases to several degrees Kelvin. Because the excite wavelength is approximately 500 meV above the band edge, the effective absorption is not expected to change significantly as a function of temperature. The low temperature data is thus fit using the value of α_{exc} obtained at room temperature, and varying the diffusivity until a reasonable match with the data was obtained.

The rising edge becomes faster (33 ps $\rightarrow$ 25 ps) as the temperature decreases to 50 °K, but begins to slow down again by 20 °K. The change in the expansion rate may be related in to the fact that the linear expansion coefficient becomes negative between 12 and 56 °K, corresponding to a region of contraction rather than expansion. The sign of the expansivity is linked to that of $\frac{d\zeta}{dT}$, where ζ is the Grüneisen parameter, which is influenced by anharmonicity terms in the lattice energy.[84]

The experimental values given for D_S at 300 and 50 °K in Table 4.2 are close to or within the range reported in the literature for the bulk diffusivity. However, the surface diffusion constant required to fit the data at 300 °K is slightly larger ($\approx$ 25%) than

Figure 4.6 Transient grating (TG) diffraction intensity versus probe delay time is plotted for data taken on a p-type (Zn, 6×10^{18} cm^{-3}) GaAs(100) crystal at 20, 50, and 300 °K. The smooth lines through the data are theoretical fits calculated using the model described in Chapter 2 and the parameters in Tables 4.1 and 4.2.

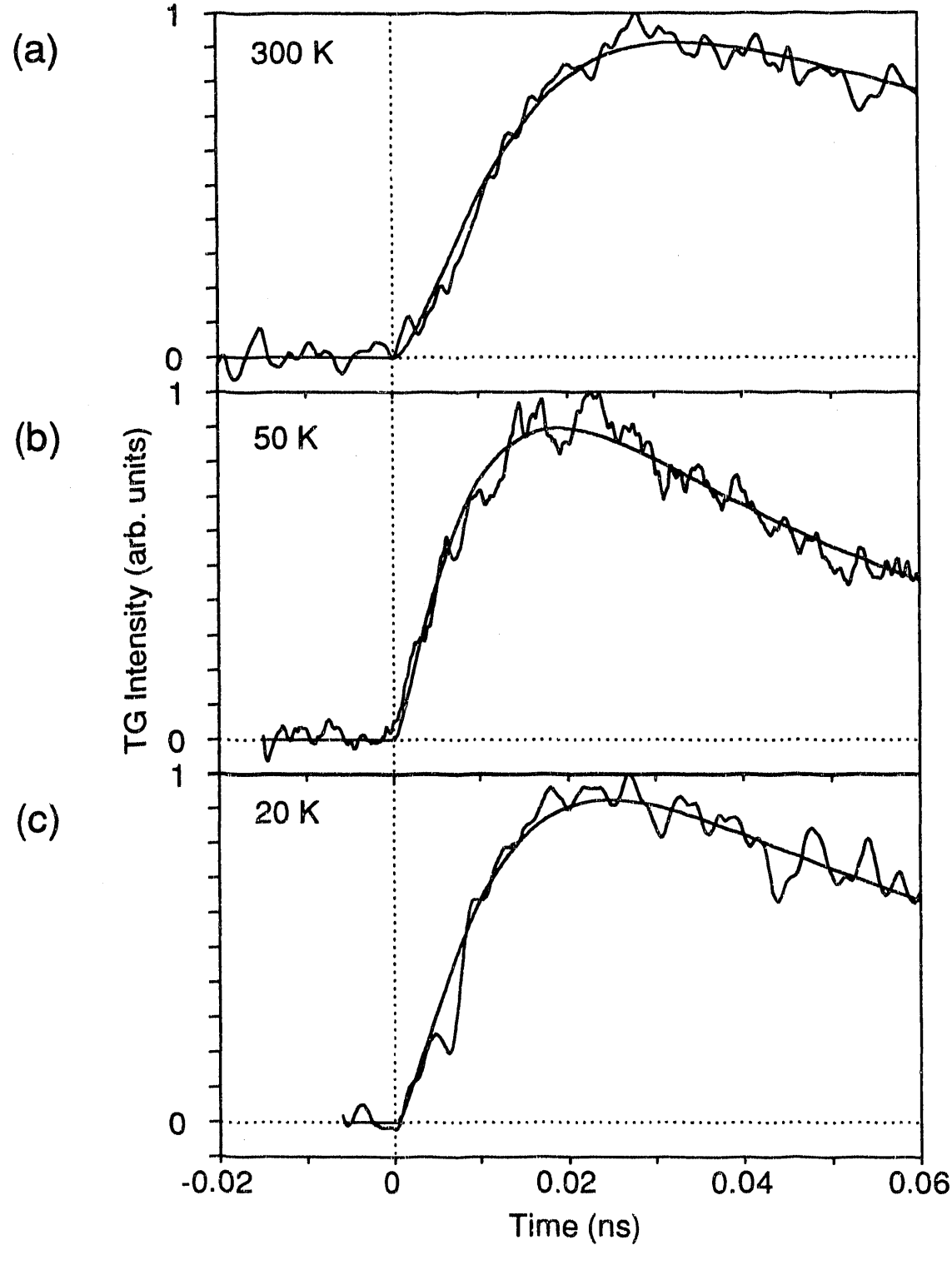
(a)
(b)
(c)
300 K
50 K
20 K
1
0
1
0
1
0
TG Intensity (arb. units)
-0.02
0
0.02
0.04
0.06
Time (ns)

the average literature value for crystalline bulk GaAs.[81-83] This is not unexpected as the electronic and vibrational properties of the surface region are known to be similar to, but not identical with the bulk ones. Furthermore, it has been suggested that higher order terms in the heat conduction equation can be important as laser powers become greater than 1 MW/cm^2.[85] At 20 °K however, the experimental value for D_S is smaller than the bulk value by more than an order of magnitude. The theoretical fit in Fig. 4.7 demonstrates our ability to fit diffusional flow away from the surface with a high degree of accuracy. This tends to confirm that the surface diffusivity is decidedly different than the bulk value at low temperatures.

At low temperature it can be difficult to bring all parts of a system into equilibrium simultaneously. While the thermal diffusivity increases overall as the temperature decreases, it does not increase to the point predicted by bulk measurements. As the surface atoms are, in general, less bonded than the bulk atoms we expect that their structure and dynamics will be more sensitive to variations in temperature than in the bulk of the crystal. The rate of energy transfer from the electrons to the phonons decreases, causing the surface to reach equilibrium more slowly than the bulk.

A qualitative explanation can be obtained by considering the processes required for equilibration of the lattice at low temperature. Near room temperature conduction of heat through the lattice is dominated by phonon-phonon scattering and is independent of impurity effects. As the temperature is reduced below 100 °K, electron-phonon scattering increasingly begins to contribute to thermal equilibration. As a result, the diffusivity is highly dependent on the dopant concentration, which explains the large spread in literature values for D at low temperatures. Immediately after the absorption of light the electrons are not in a state of equilibrium with the lattice. This produces stress derived from an electronic contribution to the strain associated with the deformation potential of the lattice and phonon contribution, which replaces the isotropic thermal stress term $3B\gamma\Delta T_O$ in Eqn. 2.11. At short times (< 1 ps), the time evolution of the

Figure 4.7 Transient grating (TG) diffraction intensity versus probe delay time is plotted for data taken on p-type (Zn, 6 x 10^{18} cm^{-3}) GaAs(100) at 20 °K. The signal rises to a maximum at 25 ps and decays to the 1/e point within 120 ps. The smooth line through the data is a theoretical fit calculated using the model described in Chapter 2 and the parameters given in Tables 4.1 and 4.2.

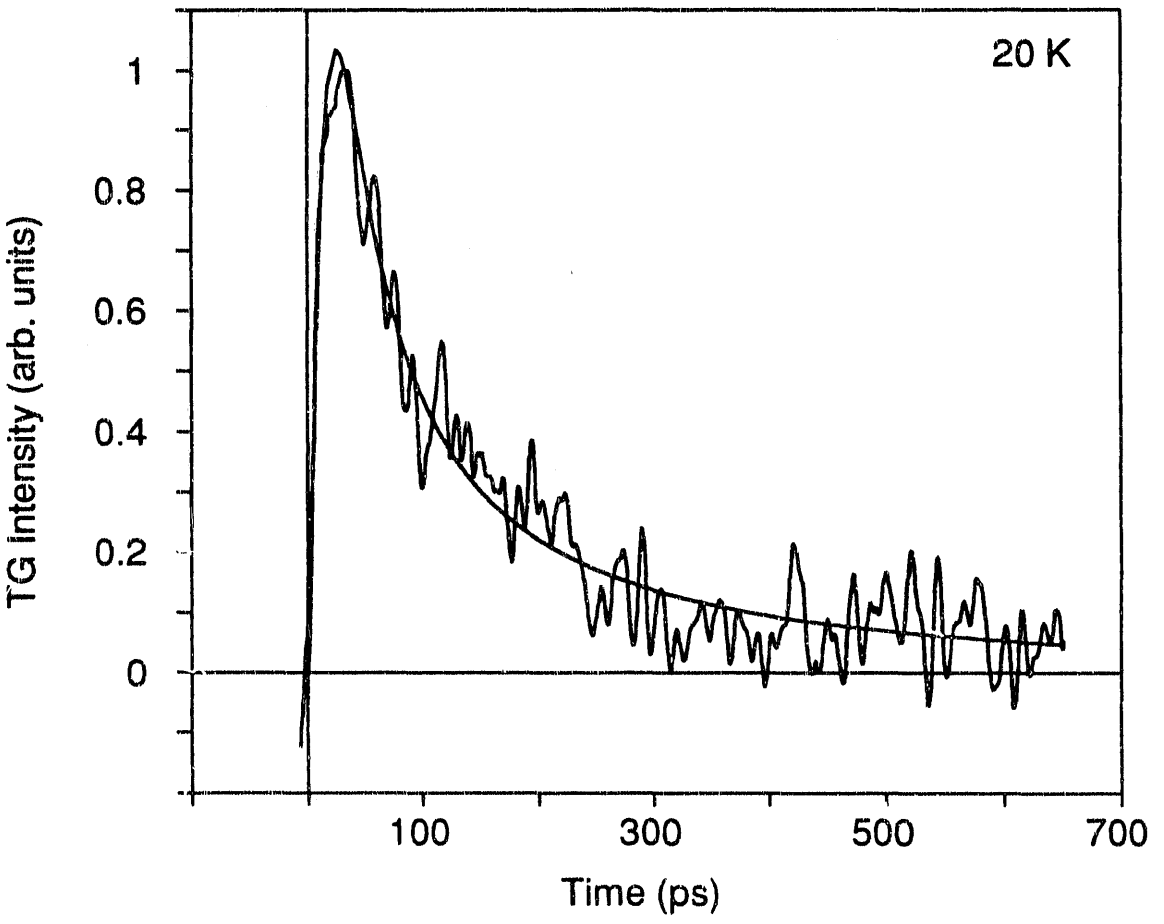
20 K
TG intensity (arb. units)
1
0.8
0.6
0.4
0.2
0
100
300
500
700
Time (ps)

electron and lattice temperature distributions are described by the set of coupled differential equations (Eqns. 2.34 and 2.35), rather than by the heat conduction equation (Eqn. 2.28).[57] The electron and lattice temperatures are coupled through the electron-phonon coupling constant which is independent of temperature. Since the electronic heat capacity depends linearly on the electron temperature, the effect of an increased electronic temperature is an increased thermal relaxation time. The hot electrons also have a much larger thermal diffusivity than in the case of equilibrium thermal transport. Thus the distance over which the energy is distributed is larger than the absorption length, δ, and the acoustic wave launched by the thermal expansion is broadened. The effect of these processes on the solution to the acoustic field equations, should generally be negligible at room temperature. However, since the time required for the optical phonons to equilibrate increases to greater than 10 ps at 10 °K, the thermal diffusivity at low temperature could be measurably affected.

The surface diffusivity, increases steadily as the temperature drops, though not as fast as the value for the bulk diffusivity. This is most likely due to an increased scattering rate at defect sites near the surface. Phonons are the major source of heat conduction in GaAs below room temperature. A high phonon scattering rate reduces the ability of the phonons to efficiently conduct heat throughout the lattice, resulting in a lower thermal diffusivity. At low temperatures, near 4 °K in pure samples, the phonons are primarily scattered by crystal boundaries. As the temperature is increased, the thermal conductivity increases, goes through a maximum and then decreases again. For a sample with a 2.6×10^{18} cm^{-3} Zn dopant concentration, this maximum occurs at approximately 30 °K.[81] Large numbers of impurities can introduce strains in the lattice, and these strains can act as scattering centers.[86] Near the maximum, impurities are the most effective phonon scatterers. Above the maximum, three-phonon normal and Umklapp processes are the prime phonon scatterers. Thus it would appear that the low diffusivity value observed for our sample at 20 °K is most likely the result of scattering

from the crystal boundary. Because the surface represents a much larger boundary area than normally encountered in the bulk, it not unreasonable that the scattering rate should be an order of magnitude larger than observed for the bulk. This would result in the lower surface diffusivity we observe at 20 °K. The values at higher temperatures are relatively unaffected as impurity and phonon-phonon scattering are approximately equivalent in the bulk and at the surface.

4.5 Anomalous Optical Absorption

The largest uncertainty in the application of our model at high temperatures comes not from the diffusivity, but from the value used for the optical absorption coefficient. The value required to fit the data is substantially larger (≈ 4 times) than the literature value for crystalline GaAs. It should be noted that there is a significant variation (a factor of at least 2) in the values reported for the absorption coefficient in the literature, due to the influence of surface preparation on this measurement.[80] Also, a survey of the literature has shown that similar absorption phenomena has commonly been observed in ultrafast experiments without a definitive explanation.[87-92]

We have considered a number of theories which could phenomenologically explain an increase in optical absorption. The most likely theory is that the ultrafast electronic excitation causes a transient change in the complex index of refraction which artificially reduces the optical absorption depth in the material. This is consistent with other ultrafast experiments performed on GaAs and other materials. Another possibility is that the ultrafast deposition of heat produces a thermally-induced change in the complex index of refraction, which results in the increased absorption we observe. If the incident pulse length is sufficiently short compared to the electron-phonon transfer time, then a nonequilibrium electron-lattice temperature will exist. Since the electronic heat capacity is much less than the lattice heat capacity, it is possible to produce transient

electron temperatures far in excess of the lattice temperature. The electron heat capacity depends linearly on the electron temperature, thus the effect of an increased electronic temperature is an increased thermal relaxation time. This could also result in the long time scale transient absorption changes commonly observed in GaAs.[69,73]

Another result of high electron temperature is an increase in the collision frequency of the electron distribution. This can create a high temperature solid density electron-hole plasma at the surface which increases absorption. Increased collisional absorption affects both s and p polarizations, which is consistent with our observations. Previous measurements in the premelting regime report a gradual increase in the reflectivity as the pump fluence rises, attributed to the dense free-carrier plasma.[89] The presence of a plasma at the surface can affect the dielectric constant through the depopulation of the valence states or through the dielectric response of the plasma itself. Depopulation effects would produce smooth gradual changes with increasing fluence. However, a power dependence study showed the expansion signal to be linear in the intensity of each of the excitation and probe beams over one and a half orders of magnitude in signal intensity, which is inconsistent with depopulation effects. This result also eliminates two-photon excitation effects. As the plasma exceeds a critical density (1.9×10^{23} cm^{-3}), enough energy is transferred to the lattice to cause melting.[89] The maximum excitation energy in our experiments was approximately $E = 4$ mJ/cm^2. This corresponds to a plasma density of

$$N = 4n\alpha_{exc}E/\hbar\ \omega_{exc}(n+1)^2 = 4 \times 10^{20}\ \text{cm}^{-3}, \tag{4.8}$$

where E is the energy per cm^2 at the excite frequency ω_{exc}. Since both the plasma and energy densities for our experiments are below the *surface* melting threshold of GaAs (30 mJ/cm^2),[88,89] it is unlikely that the absorption increase we observe is a plasma-induced phenomena.

Another possible cause of the high absorption observed is ultrafast surface disordering. Recent studies of the ultrafast disordering and melting of the lattice, propose that when deposition occurs within 100 fs, coupling to phonons may not occur sufficiently fast to prevent the excited ions from disordering directly by electronic excitation.[88] This conclusion is based on the disappearance of the surface second harmonic signal due to transformation of the surface to a centrosymmetric state at fluences near the melt threshold (0.1 J/cm^2). It is estimated that high electronic excitation may remove the restoring forces on the ions, allowing them to move greater than half the original bond length in 0.5 ps. While this type of disorder is certainly possible, it is inconsistent with our observations. We see evidence that motion of this magnitude occurs not in 0.5 ps, but on a 3-30 ps time scale as the surface responds to the deposition of heat in the acoustic phonons of the lattice. This corresponds to an energy density of 0.6 kJ/cm^3 using the value of α_{exc} from our calculations, compared to a latent heat of melting of 2.85 kJ/cm^3. Our results indicate that ionization is minimal below the melt threshold surface.

It is still possible that we are observing a premelting phenomenon which is unrelated to plasma formation. There is strong evidence that some layers near the surface are already in a liquid-like state at temperatures below the melting temperature. This phenomena is called the effect of premelting, and is defined in terms of the Lindemann criterion.[93] This states that a solid melts when the vibrational amplitudes of the atoms reach a critical fraction of the nearest neighbor distance, approximately 10%. If we consider the average displacement of each surface atomic layer, which was determined to be $\approx$ 0.04%, it is clear we are below this fraction. However, the vibrational amplitudes of the atoms are significantly larger at the top layers of the surface of crystals than further into the bulk. Consider surface atoms that are vibrating perpendicular to the surface. When moving inward, they collide with the atoms of the second layer, and the repulsive part of the crystal potential causes them to reverse their

motion. When moving outward, they don't collide with any other atoms, but the motion is again reversed, this time by the attractive part of the potential. Due to the asymmetry of the attractive and repulsive parts of the crystal potential, there is an additional outward shift of the mean position of the atoms at the surface, over the thermal expansion in the bulk. Since the vibrational amplitudes of the atoms are significantly larger at the top few layers of the surface than further into the bulk, it is possible that the top layers of the surface might meet Lindemann's criterion. Thus there is a possibility that the surface is already in a liquid-like state below the melting temperature, and that the disorder which accompanies that state could be responsible for the increased absorption.

4.6 Validity of the Theoretical Model

We have used the simplest model possible to analyze our results while still retaining the essential features of the data. Overall, the model developed in Chapter 2 describes the thermal expansion and diffusion processes observed reasonably well. However, while the increased absorption is at least partly phenomenological, we must also consider the validity of our theoretical model. One possibility for the discrepancy is the assumption in Eqn. 2.26 that the diffusion of heat out of the surface region is slow on the time scale of the expansion signal. While this is a valid assumption to first order, the two phenomena *are* interrelated; changing the value of α_{exc} primarily influences the rising edge, while the falling edge is dependent on both D_s and α_{exc}. Also, our calculations have been restricted to heat flow perpendicular to the surface, assuming an exponentially weighted heat source to account for optical absorption. A more rigorous model would be obtained by solving the acoustic field equations for the strain assuming a finite impulsive deposition of heat, rather than treating it as a step function. In order to describe the low temperature data, it may also be necessary to include the effects of electron and phonon scattering in the model as well. This would require replacing the

standard heat conduction equation (Eqn. 2.28) with the coupled heat equations (Eqns. 2.34 and 2.35).[57] At a more general level, one could also consider that the light pulse changes the electron and phonon distribution functions of the material, these changes, however,are not expected to alter the overall results of this work.

Another consideration is that our model is based upon equations of motion for the bulk crystal. The force constants of atoms near the surface are assumed to be the same as for those in the bulk, and thus are evaluated with respect to the positions corresponding to uniform thermal expansion throughout the crystal. In reality, the mean-square amplitudes of atoms at the surface of the crystal are significantly larger than in the bulk. Thus in a more general treatment of surface phenomena anharmonic effects should be taken into consideration. It has been suggested that since the disorder at the surface resembles that of a liquid, molecular dynamic simulations might be better suited for the description of surface expansion.[94,95] The liquid-like state created by melting of a surface can be described by the same anharmonicity of the interatomic potential that results in thermal expansion. In molecular dynamic calculations the anharmonicity could be treated without the approximations necessary in our model. The reliable description of the structure and dynamics of surfaces using this method requires a precise knowledge of the particle interactions. However, the main problem in molecular dynamics calculations is finding realistic interaction potentials. The accurate determination of the pair potentials for materials of interest is a matter of considerable difficulty even for the bulk, and the surface problem is much more complicated. Unfortunately, the only group of materials for which the pair potential is well known is that of noble gas solids. However, application of molecular dynamic calculations to the modeling of transient surface motion could be quite useful at some point in the future.

5. SUMMARY

The primary motivation for conducting thermophysical experiments on ultrafast time scales are to extend the measurements of thermophysical and related properties far above the limits of steady-state methods or to make measurements on systems far removed from thermodynamic equilibrium. This thesis has presented the first application of a two-color reflection transient grating technique to the direct measurement of the transient thermal expansion of a GaAs surface. We chose to study thermal expansion in GaAs semiconductors as it plays an important role in determining the residual stresses in solid state devices. Lattice mismatch and biaxial stress due to different rates of thermal expansion between multilayer semiconductor structures can generate dislocations that alter the band structure of the materials and influence carrier relaxation processes, ultimately altering the device performance. In addition to electronic effects, a study of thermal expansion of dielectric mirrors coatings could be most beneficial in understanding the mechanisms responsible for optical damage.

This method also provides a nondestructive, remote sensing method for measuring the thermal diffusivity of the surface. A comparison of our surface diffusivity values to literature values for the bulk diffusivity, shows a slightly higher diffusivity at the surface than the bulk at room temperature. At low temperature, however, the surface diffusivity is smaller than the bulk diffusivity by an order of magnitude. This is explained by increased boundary scattering of the phonons at the surface, which reduces the ability of the phonons to efficiently conduct heat throughout the lattice. Again, this observation has importance implications in the design of multilayer structures.

We have demonstrated that the expansion and diffusion signals can be modeled with reasonable accuracy using a straightforward one-dimensional theory. In this model, the acoustic field equations are solved to find the thermal expansion contribution to the transient grating observable. This expression is combined with the analytic solution to

the heat conduction equation to describe the thermal flow away from the surface. These solutions are then substituted into the diffraction efficiency equation for the reflection grating geometry, which is solved numerically. This provides a theoretical model which simultaneously describes both the thermal expansion and diffusion contributions to the signal.

The ability of the transient grating method to isolate a thermal signal lies in the selection of a probe wavelength that interacts with the material far down the band edge from the excitation wavelength. In this way the probe sees only the effect of the deposition of heat in the medium, without the interference of electronic interactions. The surface selectivity results from the reflection grating geometry used. It is known that this method is sensitive to surface properties when performed in the reflection grating geometry, while transmission studies are dominated by bulk properties. For a weakly absorbing sample the signal arises from a depth $\leq \frac{\lambda}{4\pi n}$ into the surface, provided there is an abrupt change of the dielectric constant at the surface. For high optical density materials (i.e., absorption depth $\leq$ optical wavelength), this corresponds to depth in the sample comparable to one half the Beer's absorption depth. By varying the laser wavelength, one can effectively control the optical sampling depth. As the material becomes more optically dense (i.e., absorption depth << optical wavelength), absorption becomes increasingly shallow, thus both the reflected signal and the transmitted signal are generated progressively closer to the surface. The transmitted signal contributions will become exponentially less as a function of depth into the sample, comparable to the absorption depth. The reflected signal is generated from a depth into the sample comparable to one half the Beer's absorption depth. Thus while the net effect of high optical absorption is to localize all signal generation nearer to the surface, the difference between the regions probed in transmission versus reflection becomes less.

By varying the laser wavelength, one can control the optical sampling depth. The surface can selectively be studied by using a probe wavelength far down the edge of an intense absorption band where the optical density is low, thus creating a large difference between the spatial regions from which the transmitted and reflected signals are generated. As the probe wavelength approaches the absorption band, the difference in the spatial region sampled in reflection and transmission decreases. Predominantly bulk properties can be studied by probing the grating in transmission. Thus by varying the laser wavelength and experimental grating geometry one can selectively probe to different depths in the sample, allowing the investigation of surface, interface, and bulk phenomena. Finally, the experiments in this thesis have demonstrated that by varying the probe wavelength relative to the excite wavelength one can selectively discriminate between electronic and thermomechanical phenomena.

The experiments presented in this thesis were performed at a particular wavelength, determined by the type of laser used. This limited our ability to change spatial depth being probed in the sample. However, given a more tunable laser source, this technique should be quite useful in understanding interfacial thermal dynamics. In order to observe a transient grating signal, there must be sufficient optical absorption in the material at the wavelength of interest to generate the signal. Generally, if there is sufficient energy to generate self-diffraction from the surface, there will be sufficient probe diffraction to be detected. Another requirement for these experiments is a surface of high optical quality, i.e. $\lambda/2$ on the order of the spot size or better.

The transient grating technique is exceptional for studying photothermal and photoacoustic propagation at surfaces and in thin films as it has the advantage of non contact generation and detection of a well-defined heat source at the surface or in the bulk of a sample. We have demonstrated here its sensitivity to minute displacements of the surface and its usefulness in determining surface temperature profiles and expansion dynamics. Unlike other photothermal methods, transient gratings have the ability to

discriminate between signals arising from each of the three crystallographic axes of a sample simply by varying the periodicity of the grating. The results presented here were performed with a large fringe spacing, i.e., fringe spacing >> optical absorption depth. Under these conditions, the resulting signal is primarily due to expansion and contraction perpendicular to the surface region and can be modeled reasonably well with one-dimensional solutions. For small fringe spacing however, this technique is sensitive to the component of expansion in the plane of the surface, provided the thermal diffusivity is long relative to the rate of expansion.

In many materials it would be possible to measure the parallel expansion of the surface. However, this was not the case for GaAs. To resolve this, the grating fringe spacing must be on the order of or less than the skin depth of the excitation beams. In GaAs this requires a fringe spacing of << 1 μm. This unfortunately leads to a signal decay due to thermal diffusion in the plane of the sample on the order of the thermal expansion rise time, making the parallel versus perpendicular expansion difficult to resolve in GaAs. In general, this limitation is not present in all materials, and the prediction of using transient gratings to time resolve parallel versus perpendicular expansion should be possible.

6. REFERENCES

1. I. B. Khaibullin, B. I. Shtyrkov, M. M. Zaripov, R. M. Bayazitov and M. F. Guljautdinov, Radiat. Eff. **36**, 225 (1978).
2. M. Asscher, W. L. Guthrie, T. H. Lin and G. A. Somorjai, Phys. Rev. Lett. **49**, 76 (1982).
3. H. Zacharias, M. M. T. Loy and P. A. Roland, Phys. Rev. Lett **49**, 1790 (1982).
4. T. J. Chang and H. K. Seki, Phys. Rev. Lett. **49**, 382 (1982).
5. F. Träger, H. Coufal and T. J. Chuang, Phys. Rev. Lett. **49**, 1720 (1982).
6. C. Thomsen, H. T. Grahn, H. J. Maris and J. Tauc, Phys. Rev. B **34**, 4129 (1986).
7. R. Haight, J. Bokor, J. Stark, R. H. Storz, R. R. Freeman and P. H. Bucksbaum, Phys. Rev. Lett. **54**, 1302 (1985).
8. R. W. Schoenlein, J. G. Fujimoto, G. L. Eesley and T. W. Capehart, Phys. Rev. Lett. **61**, 2596 (1988).
9. J. H. Bechtel, J. Appl. Phys. **46**, 1585 (1975).
10. M. C. Downer and C. V. Shank, Phys. Rev. Lett. **56**, 761 (1986).
11. J. G. Fujimoto, J. M. Liu, E. P. Ippen and N. Bloembergen, Phys. Rev. Lett. **53**, 1837 (1984).
12. G. L. Eesley, Phys. Rev. B **33**, 2144 (1986).
13. J. S. Meth, C. D. Marshall and M. D. Fayer, J. Appl. Phys. **67**, 3362 (1990).
14. J. E. Rothenberg, Opt. Lett. **13**, 713 (1988).
15. M. Born and E. Wolf, *Principles of Optics* (Pergamon, Oxford, 1975).
16. R. J. Collier, C. B. Burkhardt and L. H. Lin, *Optical Holography* (Academic, New York, 1971).
17. H. J. Eichler, P. Gunter and D. W. Pohl, *Laser-Induced Dynamic Gratings* (Springer-Verlag, Berlin, 1986).

18. P. Debye and F. W. Sears, Proc. Nat. Acad. Sci. **18**, 409 (1932).

19. R. Lucas and P. Biquard, J. Phys. Rad. **3**, 464 (1932).

20. H. J. Eichler, G. Enterlein, P. Glozbach, J. Munschau and H. Stahl, Appl. Opt. **11**, 372 (1972).

21. H. J. Eichler, G. Salje and H. Stahl, J. Appl. Phys **44**, 5383 (1973).

22. D. W. Phillion, D. J. Kuizenga and A. E. Siegman, Appl. Phys. Lett. **27**, 85 (1975).

23. J. R. Andrews and R. M. Hochstrasser, Chem. Phys. Lett. **76**, 207 (1980).

24. R. J. D. Miller, R. Casalegno, K. A. Nelson and M. D. Fayer, Chemical Phys. **72**, 371 (1982).

25. R. J. D. Miller, M. Pierre, T. S. Rose and M. D. Fayer, J. Phys. Chem. **53**, 3021 (1984).

26. G. Eyring and M. D. Fayer, J. Chem. Phys. **81**, 4314 (1984).

27. J. T. Fourkas, T. R. Brewer, H. Kim and M. D. Fayer, J. Chem. Phys. **95**, 5775 (1991).

28. M. D. Fayer, IEEE J. Quantum Electron. **QE-22**, 1437 (1986).

29. K. A. Nelson, R. Casalegno, R. J. D. Miller and M. D. Fayer, J. Chem. Phys. **77**, 1144 (1982).

30. A. L. Smirl, T. F. Boggess, B. S. Wherrett, G. P. Perryman and A. Miller, IEEE J. Quantum Electron. **QE-19**, 690 (1983).

31. C. D. Marshall, I. M. Fishman, R. C. Dorfman, C. B. Eom and M. D. Fayer, Phys. Rev. B in press (May 1, 1992).

32. C. D. Marshall, I. M. Fishman and M. D. Fayer, Phys. Rev. B **43**, 2696 (1991).

33. D. M. Pennington and C. B. Harris, Opt. Lett. submitted (1992); D. M. Pennington and C. B. Harris, IEEE J. Quantum Electron. submitted (1992).

34. I. M. Fishman, C. D. Marshall, J. S. Meth and M. D. Fayer, J. Opt. Soc. Am. B **8**, 1880 (1991).

35. C. D. Marshall, Ph.D. Thesis, Stanford University, 1992.

36. E. Grüneisen, Ann. Phys. (Leipzig) **39**, 257 (1912).

37. J. R. Chelikowski and M. L. Cohen, Phys. Rev. B **14**, 556 (1976).

38. M. Reine, R. Aggarwal, B. Lax and C. Wolfe, Phys. Rev. B **2**, 458 (1970).

39. R. D. Dupuis, P. D. Dapkus, R. M. Kolbas and N. Holonyak, Solid State Commun. **27**, 531 (1978).

40. D. E. Aspnes, Phys. Rev. B **14**, 5331 (1976).

41. W. H. Knox, C. Hirlimann, D. A. B. Miller, J. Shah, D. S. Chemla and C. V. Shank, Phys. Rev. Lett. **56**, 1191 (1986).

42. A. J. Taylor, D. J. Erskine and C. L. Tang, J. Opt. Soc. Am.B **2**, 663 (1985).

43. J. S. Blakemore, J. Appl. Phys. **53**, R123 (1982).

44. V. I. Zemskii, B. P. Zakharchenya and D. N. Mirlin, Pis'ma Zh. Eksp. Teor. Fiz. **24**, 96 (1976).

45. B. P. Zakharchenya, V. I. Zemskii and D. N. Mirlin, Fiz. Tverd. Tela (Leningrad) **19**, 1725 (1977).

46. D. N. Mirlin and I. I. Reshina, Zh. Eksp. Teor. Fiz. **73**, 859 (1977).

47. J. L. Oudar, A. Migus, D. Hulin, G. Grillon, J. Etchepare and A. Antonetti, Phys. Rev. Lett. **53**, 384 (1984).

48. A. Mooradian and G. B. Wright, Solid State Commun. **4**, 431 (1966).

49. C. L. Collins and P. Y. Yi, Phys Rev. B **30**, 4501 (1984).

50. J. L. T. Waugh and G. Dolling, Phys. Rev. **132**, 2410 (1963).

51. A. F. J. Levi, J. R. Hayes, P. A. Platzman and W. Wiegmann, Phys. Rev. Lett. **55**, 2071 (1985).

52. J. A. Kash and J. C. Tsang, Solid-State Electron. **31**, 419 (1988).

53. P. Kocevar, J. Phys. C **5**, 3349 (1972).

54. R. C. Desai, M. D. Levenson and J. A. Barker, Phys. Rev. A **27**, 1968 (1983).

55. H. S. Carslaw and J. C. Jaeger, *Conduction of Heat in Solids* (Oxford University Press, London, 1959).

56. M. D. Fayer, in *Spectroscopy and Excitation Dynamincs of Condensed Molecular Systems*, edited by V. M. Agranovitch and R. M. Hochstrasser (North Holland Press, 1983).

57. S. I. Anisimov, B. L. Kapeliovich and T. L. Perel'man, Zh. Eksp. Teor. Fiz. **66**, 776 (1974).

58. M. I. Kaganov, I. M. Lifshitz and L. V. Tanatarov, Zh. Eksp. Teor. Fiz. **31**, 232 (1956).

59. R. L. Fork, B. I. Greene and C. V. Shank, Appl. Phys. Lett. **38**, 671 (1981).

60. J. A. Valdmanis, R. L. Fork and J. P. Gordon, Appl. Phys. Lett. **38**, 671 (1985).

61. R. L. Fork, C. V. Shank, R. Yen and C. A. Hirlimann, IEEE J. Quantum Electron. **QE-19**, 500 (1983).

62. W. Dietel, Opt. Comm. **43**, 69 (1982).

63. L. F. Mollenauer, R. H. Stolen and J. P. Gordon, Phys. Rev. Lett. **45**, 1095 (1988).

64. F. W. Wise, I. A. Walmsley and C. L. Tang, Opt. Lett **13**, 129 (1988).

65. F. Salin, P. Grangier, G. Roger and A. Brun, Phys. Rev. Lett. **56**, 1132 (1986).

66. W. H. Knox, M. C. Downer, R. L. Fork and C. V. Shank, Opt. Lett. **9**, 552 (1984).

67. W. L. Nighan, T. Gong, L. Liou and P. M. Fauchet, Opt. Comm. **69**, 339 (1989).

68. C. Rulliere, A. Declemy, P. Kottis and L. Ducasse, Chem. Phys. Lett. **117**, 583 (1985).

69. W. Lin, R. W. Schoenlein, J. G. Fujimoto and E. P. Ippen, IEEE J. Quantum Electron. **24**, 267 (1988).

70. D. H. Auston, S. McAfee, C. V. Shank, E. P. Ippen and O. Teschke, Solid State Electron. **21**, 147 (1978).

71. R. J. D. Miller, J. J. Kasinski, L. A. Gomez-Jahn and L. Min, in *Ultrafast Phenomena VI*, edited by T. Yajima, K. Yoshihara, C. B. Harris and S. Shionoya (Springer-Verlag, Berlin, 1988).

72. W. B. Wang, N. Ockman, M. Yan and R. R. Alfano, Solid-State Electron. **32**, 1337 (1989).

73. T. Gong, W. L. Nighan and P. M. Fauchet, Appl. Phys. Lett. **57**, 2713 (1990).

74. C. M. H. Driscoll, A. F. W. Willoughby, J. B. Mullin and B. W. Straughan, *Gallium Arsenide and Related Coumpounds* (Institute of Physics, London, 1975).

75. M. E. Straumanis and C. D. Kim, Acta Crystallogr. **19**, 256 (1965).

76. H. J. McSkimin, A. Jayaraman and P. Andreatch, J. Appl. Phys. **38**, 2362 (1967).

77. B. D. Lichter and P. Sommelet, Trans. Matel. Soc. AIME **245**, 1021 (1969).

78. U. Piesbergen, Z. Naturforsch. A **18**, 141 (1963).

79. R. K. Willardson and A. C. Beer, in *Semiconductors and Semimetals*, edited by R. K. Willardson and A. C. Beer (Academic Press, New York, 1966).

80. D. E. Aspnes and A. A. Studna, Phys. Rev. B **27**, 985 (1983).

81. M. G. Holland, in *Proc. 7th Int. Conf. Phys. Semiconductors*, edited by (Dunod, Paris, 1964).

82. R. Blachnik, W. Kress and O. Madelung, in *Landolt-Bornstein New Series, Vol. III/17a*, edited by O. Madelung (Springer-Verlag, Berlin, 1982).

83. O. Madelung, in *Landolt Bornstein New Series, Vol. III/22a*, edited by O. Madelung (Springer-Verlag, Berlin, 1987).

84. S. I. Novikova, Sov. Phys. Solid State **3**, 129 (1961).

85. B. S. Yilbas, Laser Part. Beams **4**, 275 (1986).

86. P. Carruthers, Phys. Rev. **114**, 995 (1959).

87. C. V. Shank, R. Yen and C. Hirlimann, Phys. Rev. Lett. **50**, 454 (1983).

88. P. Saeta, J. K. Wang, Y. Siegal, N. Bloembergen and E. Mazur, Phys. Rev. Lett. **67**, 1023 (1991).

89. J. M. Liu, A. M. Malvezzi and N. Bloembergen, Appl. Phys. Lett. **49**, 622 (1986).

90. N. Fabricius, P. Hermes and D. von der Linde, Solid State Comm. **58**, 239 (1983).

91. J. M. Moison, F. Barthe and M. Bensoussan, Phys. Rev. B **27**, 3611 (1983).

92. A. Aydinli, H. W. Lo, M. C. Lee and C. Compaan, Phys. Rev. Lett. **46**, 1640 (1981).

93. F. A. Lindemann, Z. Phys. **14**, 609 (1910).

94. W. Schommers, in *Structure and Dynamics of Surfaces I*, edited by W. Schommers and P. von Blanckenhagen (Springer-Verlag, Berlin, 1986).

95. W. Schommers, in *Structure and Dynamics of Surfaces II*, edited by W. Schommers and P. von Blanckenhagen (Springer-Verlag, Berlin, 1987).

7. APPENDIX

7.1. Computer Programs

The programs in this appendix were used in the calculation of the theoretical fits presented in this thesis. All programs are written in the C programming language and are designed to run in a UNIX based environment. The first program, HFCALC2A.C is a numerical integration routine that calculates the transient grating observable using the equations for η (Eqn. 2.7), $\Delta\varepsilon$ (Eqn. 2.), and ΔT (Eqn. 2.) discussed in Sec. 2. A single specified set of parameters are entered for a given data set. This produces three file outputs: the calculated fit, the residual between the fit and data, and an optional file with the heat profiles used to calculate the time-dependent temperature profiles used in the calculation. An example of these profiles is given in Fig. 4.5. This program can be altered in order to calculate the independent contributions of the thermal expansion and thermal diffusion to the diffracted signal intensity as well. HEATFIT.C is a least squares fitting routine that will calculate the best fit to a given data set while varying up to five parameters. The variable parameters are T0, the maximum intensity of the signal, D, the thermal diffusivity, k_exc, the excite wavelength, k_p, the probe wavelength, and ac_amp, the acoustic field amplitude. The program iterates the parameters a specified number of iterations, or until a particular least square deviation has been reached. The sub-programs HEATFUNC.C and HEATFIT.H are required to compile HEATFIT.C. HEATFUNC.C contains the numerical integration routine required to calculate the transient grating observable, while HEATFIT.H is the header file which contains the variable definitions. HEATFIT.C produces three file outputs: the calculated fit, the residual between the fit and data, and a file of the best fit parameters.

The analytic expressions used in calculating the error (erf) and complementary error (erfc) functions in Eqn. 2.32 were taken from the *Handbook of Mathematical*

Functions With Formulas, Graphs, and Mathematical Tables, M. Abramowitz and I. A. Stegun, Eds., National Bureau of Standards Applied Mathematical Series #55, (10th Printing, December, 1972), pg. 299, Sec. 7.1.26. The error and complementary error functions are defined as

$$\text{erf } z = \frac{2}{\sqrt{\pi}} \int_{z}^{\infty} e^{-t^2}\, dt \text{ , and} \tag{7.1}$$

$$\text{erfc } z = \frac{2}{\sqrt{\pi}} \int_{\infty}^{z} e^{-t^2}\, dt = 1 - \text{erf } z \text{ , respectively.} \tag{7.2}$$

The analytical solution used for the error function was:

$$\text{erf } z = 1 - (a_1 t + a_2 t^2 + a_3 t^3 + a_4 t^4 + a_5 t^5)\, e^{-z^2} + \varepsilon(z) \text{ , where} \tag{7.3}$$

$$t = \frac{1}{1 + pz} \quad \text{and} \quad |\varepsilon(z)| \leq 1.5 \times 10^{-7} \text{ .}$$

The variables used in this function are defined below as p and a1 - a5.

7.2. HFCALC2A.C

```
#include <stdio.h>
#include <math.h>
#define PI 3.1415926535
#define  p 0.3275911
#define  a1 0.254829592
#define  a2 -0.284496736
#define  a3 1.421413741
#define  a4 -1.453152027
#define  a5 1.061405429
#define printN 50
/*global variables used in the calculation*/
/*size of the x array*/
 int xnpts = 500 ;
 struct param
{
 double alpha_exc;   /*optical attenuation constant of excitation beams*/
 double alpha_p;   /*optical attenuation constant of probe beam*/
 double D ;      /*perpendicular diffusion constant*/
 double T0 ;     /*initial heat amplitude*/
 double vel_sound ; /*velocity of sound*/
 double tau ;    /*rising edge*/
 double n_exc ;  /*real index of refraction for the excitation beams*/
 double k_exc ;  /*imaginary index of refraction for the excitation beams*/
 double n_p ; /*real index of refraction for the probe beams*/
```

```
 double k_p ; /*imaginary index of refraction for the probe beams*/
 double lambda_exc ;  /*wavelength in vacuum*/
 double lambda_p ;  /*wavelength in vacuum*/
 double delr ;    /*x spacing used in the integrator trap*/
 double fs ;
 int npts ;       /* the number of points in the integrator*/
 int skip_points ; /*number of data points to skip in calculating the fit and residual*/
 double acoustic_amp ; /*acoustic component of signal as a fraction*/
} ;
 double Re_Ar ;   /*real part of the reflection coefficient*/
 double Im_Ar ;   /*Im part of the reflection coefficient*/
 double *Re_intg_refl ;
 double *Im_intg_refl ;
 double *calc_sin ;
 double *calc_cos ;
 double *calc_exp ;
struct data
{
 int npts ;
 double *t, *y ;
} data, fit, res ;
/*t is the time, y is the diffracted signal intensity*/
main(argc, argv)
    int argc ;
    char *argv[] ;
{
 void readf(), writef(), writef_res();
```

```
FILE *outfile ;
double *x, *DeltaT, *Deltasigma ;
/*x is the position into the sample*/
/*DeltaT is the position and time (x and t) dependent Temperature Change*/
double refltrap() ; /*reflection geometry of diffraction*/
                /*trapazoidal rule integrator*/
double neg_erfc() ;
double neta33() ;   /*thermal expansion rate*/
double *dvector() ;
void free_dvector() ;
double chisq() ;
double tmp1, tmp2 ;
struct param par ;
int i, j, n ;
char printTprofile ;
double xmax, ymax ;
if(argc != 18)
  {
   printf("\nUSAGE: %s
[T0][D][n_exc][k_exc][lambda_exc][n_p][k_p][lambda_p]\n[vel_sound][fs][xmax][data]
[fit][residual][s_npts][ac_amp]\n[printTprofile(y/n)]\n", argv[0]) ;
   printf("\nT0 = initial heat amplitude") ;
   printf("\nD = perpendicular diffusion constant") ;
   printf("\nn_exc = excitation real index of refraction") ;
   printf("\nk_exc = excitation imaginary index of refraction") ;
   printf("\nlambda_exc = excitation wavelength in vacuum") ;
   printf("\nn_p = probe real index of refraction") ;
```

```
    printf("\nk_p = probe imaginary index of refraction") ;
    printf("\nlambda_p = probe wavelength in vacuum") ;
    printf("\nvel_sound = velocity of sound") ;
    printf("\nfs = fringe spacing") ;
    printf("\nxmax is the maximum depth\n") ;
    printf("\ns_npts is the the number of points to skip i.e. 2 == use every other point") ;
    printf("\nac_amp is the acoustic amplitude as a fraction of the total thermal+acoustic
signal") ;
    printf("\nprintTprofile is a switch to print the Temperatrue profiles\n\n") ;
    exit(0) ;
   }
/*redefine the command line variable so that they are understandable*/
par.T0 = atof(argv[1]) ;
par.D = atof(argv[2]) ;
par.n_exc = atof(argv[3]) ;
par.k_exc = atof(argv[4]) ;
par.lambda_exc = atof(argv[5]) ;
par.n_p = atof(argv[6]) ;
par.k_p = atof(argv[7]) ;
par.lambda_p = atof(argv[8]) ;
par.vel_sound = atof(argv[9]) ;
par.fs = atof(argv[10]) ;
xmax = atof(argv[11]) ;
/*data filename = argv[12]*/
/*fit filename = argv[13]*/
/*residual filename = argv[14]*/
par.skip_points = atof(argv[15]) ;
```

```
par.acoustic_amp = atof(argv[16]) ;
printTprofile = tolower(argv[17][0]) ;
 /*calculate the other parameters needed for the calculation*/
 par.alpha_exc = 4 * PI * par.n_exc * par.k_exc / par.lambda_exc ;
 par.alpha_p = 4 * PI * par.n_p * par.k_p / par.lambda_p ;
 par.tau = 1/(par.alpha_exc*par.vel_sound) ;
 par.npts = xnpts ;
readf(par,argv[12],&data) ;
/*read in the data file*/
/*define the array sizes*/
 fit.npts = data.npts ;
 fit.t = dvector(0, (data.npts - 1)) ;
 fit.y = dvector(0, (data.npts - 1)) ;
 res.npts = data.npts ;
 res.t = dvector(0, (data.npts - 1)) ;
 res.y = dvector(0, (data.npts - 1)) ;
x = dvector(0, xnpts) ;
DeltaT = dvector(0, xnpts) ;
Deltasigma = dvector(0, xnpts) ;
Re_intg_refl = dvector(0, xnpts) ;
Im_intg_refl = dvector(0, xnpts) ;
calc_sin =  dvector(0, xnpts) ;
calc_cos =  dvector(0, xnpts) ;
calc_exp =  dvector(0, xnpts) ;
for(i=0;i<data.npts;i++)
  {
   fit.t[i] = data.t[i] ;
```

```
   res.t[i] = data.t[i] ;
  }
/*define the x-axis for the calculation*/
for(j = 0; j < xnpts; j++) x[j] = xmax * (double)j / (double)(xnpts - 1) ;
par.delr = x[1] - x[0] ;
/*constants used in refltrap which are defined here once to save computational time*/
Re_Ar = (1 - par.n_p*par.n_p*(1+par.k_p*par.k_p)) / ((1+par.n_p)*(1+par.n_p) +
par.n_p*par.n_p*par.k_p*par.k_p) ;
Im_Ar = -2*par.n_p*par.k_p / ((1+par.n_p)*(1+par.n_p) +
par.n_p*par.n_p*par.k_p*par.k_p) ;
for(i = 0; i < xnpts; i++)
  {
   x[i] = (double)i * par.delr ;
   calc_cos[i] = cos(4*PI*par.n_p*x[i]/par.lambda_p) ;
   calc_sin[i] = sin(4*PI*par.n_p*x[i]/par.lambda_p) ;
   calc_exp[i] = exp(-par.alpha_p*x[i]) ;
   Re_intg_refl[i] = calc_cos[i] * calc_exp[i] ;
   Im_intg_refl[i] = calc_sin[i] * calc_exp[i] ;
  }
/*main loop of the program*/
n = 0 ;
for(i = 0; i < fit.npts; i++) /*time loop*/
  {
   if(fit.t[i]<=0.0)
     {
        fit.y[i] = 0.0 ;
     }
```

```
  else
    {
 if(n == 0 && printTprofile == 'y') printf("time = %lg\n", fit.t[i]) ;
        for(j = 0; j < xnpts; j++) /*position loop*/
          {
            tmp1 = exp( - par.alpha_exc * x[j]+ par.D * par.alpha_exc * par.alpha_exc *
fit.t[i]) ;
            tmp1 = tmp1 * neg_erfc((-x[j] + 2 * par.D * par.alpha_exc * fit.t[i]) / (2 *
sqrt(par.D * fit.t[i])));
            tmp2 = exp( par.alpha_exc * x[j]+ par.D * par.alpha_exc * par.alpha_exc *
fit.t[i]) ;
            tmp2 = tmp2 * neg_erfc((x[j] + 2 * par.D * par.alpha_exc * fit.t[i]) / (2 *
sqrt(par.D * fit.t[i])));
            DeltaT[j] = (tmp1 + tmp2) / 2 ;
            Deltasigma[j] = neta33(par,x[j],data.t[i], DeltaT[j]) ;
                  if(n == 0 && printTprofile == 'y')
        printf("%lg %lg\n", x[j], DeltaT[j]) ;
           /*no comments here will print the heat profiles*/
           /*printf("%lg %lg\n", x[j], Deltasigma[j]) ;*/
           /*no comments here will print the strain profiles*/
          }/*end of position loop*/
         fit.y[i] = refltrap(par, x, Deltasigma) ;  /*call the reflected diffracted signal
integrator*/
        /*end of space loop*/
     }  /*end of else */
   n = n + 1 ;
        if(n == printN && printTprofile == 'y')
```

```
                {
                n = 0 ;
                printf("\n") ;
                }
  } /*end of time loop*/
/*include the  effect of parallel heat flow*/
for(i = 0; i < fit.npts; i++) fit.y[i] = fit.y[i] * exp(-
2*par.D*fit.t[i]*(2*PI/par.fs)*(2*PI/par.fs)) ;
/*find the maximum value of the signal*/
ymax = 0 ;
for(i = 0; i < fit.npts; i++)
  {
   if(fit.y[i]>ymax) ymax = fit.y[i] ;
  }
 for(i = 0; i < fit.npts; i++) fit.y[i] = fit.y[i] * par.T0 / ymax ;
/*calculate the residuals now*/
for(i = 0; i < res.npts; i++) res.y[i] = data.y[i] - fit.y[i] ;
writef(argv[13], &fit) ;
writef_res(argv[14], &res, (chisq(&res)) ) ;
free_dvector(fit.t,0) ;
free_dvector(fit.y, 0) ;
free_dvector(data.t,0) ;
free_dvector(data.y, 0) ;
free_dvector(res.t, 0) ;
free_dvector(res.y, 0) ;
free_dvector(x, 0) ;
free_dvector(DeltaT, 0) ;
```

```
free_dvector(Deltasigma, 0) ;
free_dvector(Re_intg_refl, 0) ;
free_dvector(Im_intg_refl, 0) ;
free_dvector(calc_cos, 0) ;
free_dvector(calc_sin, 0) ;
free_dvector(calc_exp, 0) ;
}
/*end of main*/
/*************************************************************/
double trap(par, y)
    struct param par ;
    double y[] ;
{
 int i ;
 double sum ;
 sum = (y[0] + y[par.npts - 1]) / 2.0 ;
 for(i = 1; i < (par.npts - 1); i++)
   sum = sum + y[i] ;
 sum = sum * par.delr ;
 return(sum) ;
}
/*************************************************************/
double refltrap(par, x, y)
    struct param par ;
    double x[], y[] ;
{
 int i ;
```

```
 double trap() ;
 double real_integral ;
 double im_integral ;
 double integral ;
 double *intg ;
 intg = dvector(0, (par.npts-1)) ;
 for(i = 0; i < par.npts ; i++)
  intg[i] = y[i] * Re_intg_refl[i] ;
 real_integral = trap(par, intg) ;
 for(i = 0; i < par.npts ; i++)
  intg[i] = y[i] * Im_intg_refl[i] ;
 im_integral = trap(par, intg) ;
 integral = real_integral * real_integral + im_integral * im_integral ;
 free_dvector(intg, 0) ;
 return(integral) ;
}
/*********************************************************/
double as_erfc(z)
   double z ;
{
   double t ;
 double twooversqrtpi = 1.12837917 ;
   if(z<1e-6) return(1 - twooversqrtpi * z) ;
   else
     {
/*       return(erfc(z)) ;*/
         t = 1 / (1+p*z) ;
```

```
      return((a1*t+a2*t*t+a3*t*t*t+a4*t*t*t*t+a5*t*t*t*t*t)*exp(-z*z)) ;
     }
  }
/*********************************************************/
double as_erf(z)
    double z ;
{
 double t ;
 double twooversqrtpi = 1.12837917 ;
 if(z<1e-6) return(twooversqrtpi * z) ;
 else
   {
/*     return(erf(z)) ; */
    t = 1 / (1+p*z) ;
    return(1-(a1*t+a2*t*t+a3*t*t*t+a4*t*t*t*t+a5*t*t*t*t*t)*exp(-z*z)) ;
   }
}
/*********************************************************/
double neg_erfc(z)
    double z ;
{
 double as_erf() ;
 double as_erfc() ;
/*printf("%lg\n", z) ;*/
 if(z<0) return(1+as_erf(-z)) ;
 else    return(as_erfc(z)) ;
}
```

```
/*****************************************************/
double neta33(par,x,t,delT)
struct param par ;
double x ;
double t ;
double delT ;
{
double tmp ;
double sgn() ;
        tmp = delT*(1 - (1-par.acoustic_amp)*exp(-t/par.tau)) - par.acoustic_amp*exp(-
fabs(par.alpha_exc*x - t/par.tau))*sgn(x - par.vel_sound*t);
        return(tmp) ;
}
/*****************************************************/
double sgn(a)
double a;
{
if(a<0) return(-1.0) ;
else return(1.0) ;
}
/*********************************************************************/
void writef(fname, xy)
char fname[] ;
struct data *xy ;
{
 int i ;
 FILE *outfile ;
```

```
 if((outfile = fopen(fname, "w+")) == (NULL))
   {
    printf("\nCan't open file #%s#\n", fname) ;
    exit(0) ;
   }
 for(i = 0; i < (*xy).npts; i++)
   fprintf(outfile, "%lg    %lg\n", (*xy).t[i], (*xy).y[i]) ;
 fclose(outfile) ;
}
/*****************************************************************/
void writef_res(fname, xy, CHISQ)
char fname[] ;
struct data *xy ;
double CHISQ ;
{

 int i ;
 FILE *outfile ;
 if((outfile = fopen(fname, "w+")) == (NULL))
   {
    printf("\nCan't open file #%s#\n", fname) ;
    exit(0) ;
   }
 for(i = 0; i < (*xy).npts; i++)
   fprintf(outfile, "%lg    %lg\n", (*xy).t[i], (*xy).y[i]) ;
 fclose(outfile) ;
 printf("\nfilename= %s  chisq= %lg\n", fname, CHISQ) ;
```

```
}
/*****************************************************************/
void readf(par, fname, xy)
struct param par ;
char fname[] ;
struct data *xy ;
{
 int i, j, tmpnpts ;
 FILE *infile ;
 double *dvector() ;
 char buf[100] ;
 (*xy).npts = 0 ;
 if((infile = fopen(fname, "r+")) == (NULL))
   {
    printf("\nCan't open file #%s#\n", fname) ;
    exit(0) ;
   }
 while(fgets(buf, 100, infile) != (NULL))
  (*xy).npts = (*xy).npts + 1 ;
 fclose(infile) ;
 (*xy).t = dvector(0, (*xy).npts) ;
 (*xy).y = dvector(0, (*xy).npts) ;
 if((infile = fopen(fname, "r+")) == (NULL))
   {
    printf("\ncan't open file %s\n", fname) ;
    exit(0) ;
   }
```

```
 for(i = 0; i < (*xy).npts; i++)
    fscanf(infile, "%lf    %lf", &(*xy).t[i], &(*xy).y[i]) ;
 fclose (infile) ;
if(par.npts  < 1)
        {
        printf("\n\nthe numer of points to skip >= 1\n\n") ;
        exit(0) ;
        }
/*use every n'th point*/
j = 0 ;
 for(i = 0; i < (*xy).npts; i=i+par.skip_points)
        {
        (*xy).t[j] = (*xy).t[i] ;
        (*xy).y[j] = (*xy).y[i] ;
        j = j + 1 ;
        }
/* redefine the new number of points*/
(*xy).npts = j ;
}
/*****************************************************************************/
double *dvector(nl, nh)
int nl, nh ;
{
 double *v ;
 v = (double *)malloc((unsigned)(nh - nl + 1) * sizeof(double)) ;
 if(!v)
   {
```

```
    printf("\nalloc error..help\n") ;
    exit(0) ;
   }
 return(v - nl) ;
}
/*************************************************************/
/*frees memory allocated by dvector*/
void free_dvector(v, nl)
int nl ;
double *v ;
{
 free((char *)(v + nl)) ;
}
/*************************************************************/
double chisq(xy)
struct data *xy ;
{
 int i ;
 double sum ;
 sum = 0.0 ;
    for(i = 0; i < res.npts; i++)
        {
         sum = sum + res.y[i] * res.y[i] ;
        }
   return(sum / res.npts) ;
}
```

7.3. HEATFIT.C

```
/*heatfit.c*/
/*program fits raw transient grating data with up to 5 parameters*/
/*must use heatfunc.c and heatfit.h to compile the program*/
#include "heatfit.h"
main(argc, argv)
int argc ;
char *argv[] ;
{
 struct param par ;
 int i, j, max_iter ;
 void readf(), writef(), writef_res(), cut_data(), free_dvector() ;
 double oldchi, newchi, fitroutine(), pdiff(), tol, heatfit(), *dvector() ;
 double delta_chisq ;
 double ss[9] ;
 FILE *outfile ;
 if(argc != 25)
   {
    printf("USAGE: heatfit [datafile][T0][D][n_exc][k_exc][lambda_exc][n_p][k_p]\n")
;
    printf("[lambda_p][vel_sound][fs][xmax][skip_npts][max_iter][tol][fit_file]\n") ;

printf("[res_file][ss(T0)][ss(D)][ss(k_exc)][ss(vel_sound)][ss(ac_amp)][fit_par][ac_amp]
\n") ;
   printf("\nT0 = initial heat amplitude") ;
```

```
    printf("\nD = perpendicular diffusion constant") ;
    printf("\nn_exc = excitation real index of refraction") ;
    printf("\nk_exc = excitation imaginary index of refraction") ;
    printf("\nlambda_exc = excitation wavelength in vacuum") ;
    printf("\nn_p = probe real index of refraction") ;
    printf("\nk_p = probe imaginary index of refraction") ;
    printf("\nlambda_p = probe wavelength in vacuum") ;
    printf("\nvel_sound = velocity of sound") ;
    printf("\nfs = fringe spacing") ;
    printf("\nxmax is the maximum depth\n") ;
    printf("\nskip_npts is the the number of points to skip i.e. 2 == use every other
point") ;
    printf("\nac_amp is the acoustic amplitude as a fraction of the total thermal+acoustic
signal\n\n") ;
    printf("\nT0, D, k_exc, k_p, ac_amp are being fit\n") ;
    printf("\nwith initial step sizes ss(T0) thru ss(ac_amp) respectively") ;
    printf("\nin ss percent of the initial value of that parameter\n") ;
    printf("\nthe units are Ang. and ns\n") ;
    exit(0) ;
   }
  par.T0 = atof(argv[2]) ;       /*initial data height*/
  par.D = atof(argv[3]) ;        /*diffusion constant*/
  par.n_exc = atof(argv[4]) ;
  par.k_exc = atof(argv[5]) ;
  par.lambda_exc = atof(argv[6]) ;
  par.n_p = atof(argv[7]) ;
  par.k_p = atof(argv[8]) ;
```

```
 par.lambda_p = atof(argv[9]) ;
 par.vel_sound = atof(argv[10]) ;
 par.fs = atof(argv[11]) ;
 par.xmax = atof(argv[12]) ;
 par.skip_npts = atoi(argv[13]) ;
 max_iter = atoi(argv[14]) ;    /*maximum number of interations in the fitting routine*/
 tol = atof(argv[15]) ;         /*tolerance of the fit*/
/*fit file = argv[16]*/
/*res file = argv[17]*/
 ss[0] = atof(argv[18]) ;
 ss[1] = atof(argv[19]) ;
 ss[2] = atof(argv[20]) ;
 ss[3] = atof(argv[21]) ;
 ss[4] = atof(argv[22]) ;
/*parameter file = argv[23]*/
 par.acoustic_amp = atof(argv[24]) ;
printf("this routine will fit %d iterations\n", max_iter) ;
printf("or until a convergence of %lg is reached for chi squared\n\n", tol) ;
readf(par, argv[1], &data) ;
 if((outfile = fopen(argv[23], "w+")) == NULL)
   {
    printf("\ncant open file\n") ;
    exit(0) ;
   }
  fprintf(outfile, "\n") ;
  fclose(outfile) ;
 /*define the array sizes*/
```

```
 fit.npts = data.npts ;
 fit.t = dvector(0, (data.npts - 1)) ;
 fit.y = dvector(0, (data.npts - 1)) ;
 res.npts = data.npts ;
 res.t = dvector(0, (data.npts - 1)) ;
 res.y = dvector(0, (data.npts - 1)) ;
 f_par.npar = 5 ;
/*fit the following 5 parameters*/
 f_par.par[0] = par.T0 ;
 f_par.par[1] = par.D ;
 f_par.par[2] = par.k_exc ;
 f_par.par[3] = par.vel_sound ;
 f_par.par[4] = par.acoustic_amp ;
/*start with ss% initial steps*/
 f_par.step[0] = f_par.orig_step[0] = f_par.par[0] * ss[0] / 100 ;
 f_par.step[1] = f_par.orig_step[1] = f_par.par[1] * ss[1] / 100 ;
 f_par.step[2] = f_par.orig_step[2] = f_par.par[2] * ss[2] / 100 ;
 f_par.step[3] = f_par.orig_step[3] = f_par.par[3] * ss[3] / 100 ;
 f_par.step[4] = f_par.orig_step[4] = f_par.par[4] * ss[4] / 100 ;
/*note: set these step sizes to zero if you do not wish to fit these parameters*/
 delta_chisq = 10000000.0 ;
 oldchi = 10000000.0 ;
 i = 0 ;
 while(delta_chisq > tol && i < max_iter)
   {
    printf("del_chisq = %lg iter # = %d\n", delta_chisq, i) ;
    newchi = heatfit(par, argv[23]) ;
```

```
    delta_chisq = pdiff(oldchi, newchi) ;
/*parameter output file test*/
    if((outfile = fopen(argv[23], "a")) == NULL)
        {
         printf("\ncan't open file\n") ;
         exit(0) ;
        }
    fprintf(outfile, "iter = %d chisq = %lg delta chisq = %lg\n", i, newchi, delta_chisq) ;
    fprintf(outfile, "T0=%lg D=%lg k_exc=%lg k_p=%lg
ac_amp=%lg\n\n",f_par.par[0], f_par.par[1], f_par.par[2], f_par.par[3], f_par.par[4]) ;
    fclose(outfile) ;
    i = i + 1 ;
    oldchi = newchi ;
   }
  writef(argv[16], &fit) ;
  writef_res(argv[17], &res) ;
  printf("\nend of fitting procedure\n") ;
free_dvector(fit.t, 0) ;
free_dvector(fit.y, 0) ;
free_dvector(res.t, 0) ;
free_dvector(res.y, 0) ;
free_dvector(data.t, 0) ;
free_dvector(data.y, 0) ;
}
/*end of main*/
double pdiff(p1, p2)
double p1, p2 ;
```

```
 {
 if(p1 == 0.0 && p2 == 0.0)
  return(0.0) ;
 else if(p1 == 0.0 && p2 != 0.0)
  return(10.0) ;
 else
  return(fabs((p1 - p2) * 100.0 / p1)) ;
}
double *dvector(nl, nh)
int nl, nh ;
{
 double *v ;
 v = (double *)malloc((unsigned)(nh - nl + 1) * sizeof(double)) ;
 if(!v)
  {
   printf("\nalloc error..help\n") ;
   printf("\n dvector(%d,%d)\n", nl, nh) ;
  }
 return(v - nl) ;
}
/*frees memory allocated by dvector*/
void free_dvector(v, nl)
int nl ;
double *v ;
{
 free((char *)(v + nl)) ;
}
```

```
double chisq(par)
struct param par ;
{
 int i ;
 double sum ;
 void heatfunc() ;
 par.T0 = f_par.par[0] ;
 par.D = f_par.par[1] ;
 par.k_exc = f_par.par[2] ;
 par.vel_sound = f_par.par[3] ;
 par.acoustic_amp = f_par.par[4] ;
 heatfunc(par) ;
 sum = 0.0 ;
    for(i = 0; i < data.npts; i++)
        {
         res.y[i] = data.y[i] - fit.y[i] ;
         sum = sum + res.y[i] * res.y[i] ;
        }
 return(sum / data.npts) ;
}
double heatfit(par, fname)
struct param par ;
char fname[] ;
{
 int   i, j, k;
 int   iterations_per_param;
 double chisq();
```

```
 double step, chsq1, chsq2, chsq3, chsq_new ;
 double fit_change1, fit_change2, fit_change3;
 FILE *outfile ;
 for(i = 0; i < f_par.npar; ++i)  /* loop through each fit parameter */
   {
    step = f_par.step[i];
    if(step == 0.0)
     continue;  /* fixed parameter -> return to top of for-loop */
    chsq1 = chisq(par) ;
    iterations_per_param = 0;
/*
    if((outfile = fopen(fname, "a")) == NULL)
        {
         printf("\ncant open file\n") ;
         exit(0) ;
        }
fprintf(outfile, "T0=%lg D=%lg k_exc=%lg vel_sound=%lg ac_amp=%lg chisq1 =
%lg\n",f_par.par[0],f_par.par[1],f_par.par[2],f_par.par[3],f_par.par[4], chsq1) ;
fclose(outfile) ;
*/

    /* loop until get a change in sum of residuals */
    do
     {
        f_par.par[i] += step;
        chsq2 = chisq(par);
/*
```

```
    if((outfile = fopen(fname, "a")) == NULL)
      {
       printf("\ncant open file\n") ;
       exit(0) ;
      }
fprintf(outfile, "T0=%lg D=%lg k_exc=%lg vel_sound=%lg ac_amp=%lg chisq2 =
%lg\n",f_par.par[0],f_par.par[1],f_par.par[2],f_par.par[3],f_par.par[4], chsq2) ;
fclose(outfile) ;
*/
          fit_change2 = chsq2 - chsq1;
          if(fit_change2 == 0.0)
            step = -(step + step);
      }
    while(fit_change2 == 0.0);
    /* loop while fit improving */
    do
      {
          if(fit_change2 > 0.0) /* last fit worse -> change "direction" */
            {
              step = -step;
              f_par.par[i] += step;
              chsq2 = chsq1;
              fit_change2 = -fit_change2;
            }
          ++iterations_per_param;
          f_par.par[i] += step;
          chsq3 = chisq(par) ;
```

```
/*
    if((outfile = fopen(fname, "a")) == NULL)
     {
      printf("\ncant open file\n") ;
      exit(0) ;
     }
fprintf(outfile, "T0=%lg D=%lg k_exc=%lg vel_sound=%lg ac_amp=%lg
chisq3=%lg\n",f_par.par[0],f_par.par[1],f_par.par[2],f_par.par[3],f_par.par[4], chsq3) ;
fclose(outfile) ;
*/
          fit_change1 = chsq3 - chsq2;
          if(fit_change1 < 0.0)
            {
             fit_change2 = fit_change1;
             chsq2 = chsq3;
            }
      }
    while(fit_change1 < 0.0);
    fit_change2 = fit_change1 - fit_change2;
    f_par.par[i] -= step*(0.5 + fit_change1/fit_change2);
    step = fabs(step);
    f_par.step[i] = step * iterations_per_param/3.0;
    }
  /* end of loop through each fitting parameter */
  /* find residual for final fit of this iteration */
  chsq_new = chisq(par) ;
  return(chsq_new);
}
```

7.4. HEATFUNC.C

```
#include "heatfit.h"
void heatfunc(par)
    struct param par ;
{
 double *x, *DeltaT, *Deltasigma ;
 /*x is the position into the sample*/
 /*DeltaT is the position and time (x and t) dependent Temperature Change*/
 double refltrap() ; /*reflection geometry of diffraction*/
 /*trapazoidal rule integrator*/
 double neg_erfc() ;
 double neta33() ;   /*thermal expansion rate*/
 int xnpts = 500 ;
 double *dvector() ;
 void free_dvector() ;
 double chisq() ;
 double tmp1, tmp2 ;
 int i, j ;
 double ymax ;
 /*calculate the other parameters needed for the calculation*/
 par.alpha_exc = 4 * PI * par.n_exc * par.k_exc / par.lambda_exc ;
 par.alpha_p = 4 * PI * par.n_p * par.k_p / par.lambda_p ;
 par.tau = 1/(par.alpha_exc*par.vel_sound) ;
 par.npts = xnpts ;
 /*define the array sizes*/
```

```
fit.npts = data.npts ;
x = dvector(0, xnpts) ;
DeltaT = dvector(0, xnpts) ;
Deltasigma = dvector(0, xnpts) ;
Re_intg_refl = dvector(0, xnpts) ;
Im_intg_refl = dvector(0, xnpts) ;
calc_sin =  dvector(0, xnpts) ;
calc_cos =  dvector(0, xnpts) ;
calc_exp =  dvector(0, xnpts) ;
for(i=0;i<data.npts;i++)
  {
   fit.t[i] = data.t[i] ;
   res.t[i] = data.t[i] ;
  }
/*define the x-axis for the calculation*/
for(j = 0; j < xnpts; j++) x[j] = par.xmax * (double)j / (double)(xnpts - 1) ;
par.delr = x[1] - x[0] ;
/*constants used in refltrap which are defined here once to save computational time*/
Re_Ar = (1 - par.n_p*par.n_p*(1+par.k_p*par.k_p)) / ((1+par.n_p)*(1+par.n_p) +
par.n_p*par.n_p*par.k_p*par.k_p) ;
Im_Ar = -2*par.n_p*par.k_p / ((1+par.n_p)*(1+par.n_p) +
par.n_p*par.n_p*par.k_p*par.k_p) ;
for(i = 0; i < xnpts; i++)
  {
   x[i] = (double)i * par.delr ;
   calc_cos[i] = cos(4*PI*par.n_p*x[i]/par.lambda_p) ;
   calc_sin[i] = sin(4*PI*par.n_p*x[i]/par.lambda_p) ;
```

```
    calc_exp[i] = exp(-par.alpha_p*x[i]) ;
    Re_intg_refl[i] = calc_cos[i] * calc_exp[i] ;
    Im_intg_refl[i] = calc_sin[i] * calc_exp[i] ;
   }
 /*main loop of the program*/
 for(i = 0; i < fit.npts; i++) /*time loop*/
   {
    if(fit.t[i]<=0.0)
        {
         fit.y[i] = 0.0 ;
        }
    else
        {
         for(j = 0; j < xnpts; j++) /*position loop*/
           {
             tmp1 = exp( - par.alpha_exc * x[j]+ par.D * par.alpha_exc * par.alpha_exc *
fit.t[i]) ;
             tmp1 = tmp1 * neg_erfc((-x[j] + 2 * par.D * par.alpha_exc * fit.t[i]) / (2 *
sqrt(par.D * fit.t[i])));
             tmp2 = exp( par.alpha_exc * x[j]+ par.D * par.alpha_exc * par.alpha_exc *
fit.t[i]) ;
             tmp2 = tmp2 * neg_erfc((x[j] + 2 * par.D * par.alpha_exc * fit.t[i]) / (2 *
sqrt(par.D * fit.t[i])));
             DeltaT[j] = (tmp1 + tmp2) / 2 ;
             Deltasigma[j] = neta33(par,x[j],data.t[i], DeltaT[j]) ;
             /*    printf("%lg %lg\n", x[j], DeltaT[j]) ;*/
             /*no comments here will print the heat profiles*/
```

```
            /*    printf("%lg %lg\n", x[j], Deltasigma[j]) ;*/
            /*no comments here will print the strain profiles*/
           }
        fit.y[i] = refltrap(par, x, Deltasigma) ;  /*call the reflected diffracted signal
integrator*/
        /*end of space loop*/
       }  /*end of else */
  }  /*end of time loop*/
 /*include the  effect of parallel heat flow*/
 for(i = 0; i < fit.npts; i++) fit.y[i] = fit.y[i] * exp(-
2*par.D*fit.t[i]*(2*PI/par.fs)*(2*PI/par.fs)) ;
 /*find the maximum value of the signal*/
 ymax = 0 ;
 for(i = 0; i < fit.npts; i++)
  {
   if(fit.y[i]>ymax) ymax = fit.y[i] ;
  }
 for(i = 0; i < fit.npts; i++) fit.y[i] = fit.y[i] * par.T0 / ymax ;
 free_dvector(x, 0) ;
 free_dvector(DeltaT, 0) ;
 free_dvector(Deltasigma, 0) ;
 free_dvector(Re_intg_refl, 0) ;
 free_dvector(Im_intg_refl, 0) ;
 free_dvector(calc_cos, 0) ;
 free_dvector(calc_sin, 0) ;
 free_dvector(calc_exp, 0) ;
}
```

```
/*end of main*/
/*************************************************************/
double trap(par, y)
    struct param par ;
    double y[] ;
{
 int i ;
 double sum ;
 sum = (y[0] + y[par.npts - 1]) / 2.0 ;
 for(i = 1; i < (par.npts - 1); i++)
  sum = sum + y[i] ;
 sum = sum * par.delr ;
 return(sum) ;
}
/*************************************************************/
double refltrap(par, x, y)
    struct param par ;
    double x[], y[] ;
{
 int i ;
 double trap() ;
 double real_integral ;
 double im_integral ;
 double integral ;
 double *intg ;
 intg = dvector(0, (par.npts-1)) ;
 for(i = 0; i < par.npts ; i++)
```

```
  intg[i] = y[i] * Re_intg_refl[i] ;
 real_integral = trap(par, intg) ;
 for(i = 0; i < par.npts ; i++)
  intg[i] = y[i] * Im_intg_refl[i] ;
 im_integral = trap(par, intg) ;
 integral = real_integral * real_integral + im_integral * im_integral ;
 free_dvector(intg, 0) ;
 return(integral) ;
}
/*********************************************************/
double as_erfc(z)
   double z ;
{
   double t ;
 double twooversqrtpi = 1.12837917 ;
   if(z<1e-6) return(1 - twooversqrtpi * z) ;
   else
     {
/*       return(erfc(z)) ;*/
         t = 1 / (1+p*z) ;
      return((a1*t+a2*t*t+a3*t*t*t+a4*t*t*t*t+a5*t*t*t*t*t)*exp(-z*z)) ;
     }
  }
/*********************************************************/
double as_erf(z)
   double z ;
{
```

```
 double t ;
 double twooversqrtpi = 1.12837917 ;
 if(z<1e-6) return(twooversqrtpi * z) ;
 else
   {
/*     return(erf(z)) ; */
    t = 1 / (1+p*z) ;
    return(1-(a1*t+a2*t*t+a3*t*t*t+a4*t*t*t*t+a5*t*t*t*t*t)*exp(-z*z)) ;
   }
}
/*************************************************************/
double neg_erfc(z)
   double z ;
{
 double as_erf() ;
 double as_erfc() ;
/*printf("%lg\n", z) ;*/
 if(z<0) return(1+as_erf(-z)) ;
 else    return(as_erfc(z)) ;
}
/*************************************************************/
double neta33(par,x,t,delT)
struct param par ;
double x ;
double t ;
double delT ;
{
```

```
double tmp ;
double sgn() ;
        tmp = delT*(1 - (1-par.acoustic_amp)*exp(-t/par.tau)) - par.acoustic_amp*exp(-
fabs(par.alpha_exc*x - t/par.tau))*sgn(x - par.vel_sound*t);
        return(tmp) ;
}
/*************************************************/
double sgn(a)
double a;
{
if(a<0) return(-1.0) ;
else return(1.0) ;
}
/*********************************************************************/
void writef(fname, xy)
char fname[] ;
struct data *xy ;
{
 int i ;
 FILE *outfile ;
 if((outfile = fopen(fname, "w+")) == (NULL))
   {
    printf("\nCan't open file #%s#\n", fname) ;
    exit(0) ;
   }
 for(i = 0; i < (*xy).npts; i++)
   fprintf(outfile, "%lg    %lg\n", (*xy).t[i], (*xy).y[i]) ;
```

```
 fclose(outfile) ;
}
/*********************************************************************/
void writef_res(fname, xy)
char fname[] ;
struct data *xy ;
{
 int i ;
 FILE *outfile ;
 if((outfile = fopen(fname, "w+")) == (NULL))
   {
    printf("\nCan't open file #%s#\n", fname) ;
    exit(0) ;
   }
 for(i = 0; i < (*xy).npts; i++)
   fprintf(outfile, "%lg    %lg\n", (*xy).t[i], (*xy).y[i]) ;
 fclose(outfile) ;
}
/*********************************************************************/
void readf(par, fname, xy)
struct param par ;
char fname[] ;
struct data *xy ;
{
 int i, j, tmpnpts ;
 FILE *infile ;
 double *dvector() ;
```

```
 char buf[100] ;
 (*xy).npts = 0 ;
 if((infile = fopen(fname, "r+")) == (NULL))
  {
    printf("\nCan't open file #%s#\n", fname) ;
    exit(0) ;
  }
 while(fgets(buf, 100, infile) != (NULL))
  (*xy).npts = (*xy).npts + 1 ;
 fclose(infile) ;
 (*xy).t = dvector(0, (*xy).npts) ;
 (*xy).y = dvector(0, (*xy).npts) ;
 if((infile = fopen(fname, "r+")) == (NULL))
  {
    printf("\ncan't open file %s\n", fname) ;
    exit(0) ;
  }
 for(i = 0; i < (*xy).npts; i++)
    fscanf(infile, "%lf    %lf", &(*xy).t[i], &(*xy).y[i]) ;
 fclose (infile) ;
if(par.skip_npts  < 1)
        {
        printf("\n\nthe numer of points to skip >= 1\n\n") ;
        exit(0) ;
        }
/*use every n'th point*/
j = 0 ;
```

```
 for(i = 0; i < (*xy).npts; i=i+par.skip_npts)
        {
        (*xy).t[j] = (*xy).t[i] ;
        (*xy).y[j] = (*xy).y[i] ;
        j = j + 1 ;
        }
/* redefine the new number of points*/
(*xy).npts = j ;
}
```

7.5. HEATFIT.H

```
/*must use heatfunc.c and heatfit.c to compile the program*/
#include <stdio.h>
#include <math.h>
#define PI 3.1415926535
#define  p 0.3275911
#define  a1 0.254829592
#define  a2 -0.284496736
#define  a3 1.421413741
#define  a4 -1.453152027
#define  a5 1.061405429
#include <ctype.h>
/*global variables used in the calculation*/
  struct param
{
  double alpha_exc;    /*optical attenuation constant of excitation beams*/
```

```
double alpha_p;   /*optical attenuation constant of probe beam*/
double D ;      /*perpendicular diffusion constant*/
double T0 ;     /*initial heat amplitude*/
double vel_sound ; /*velocity of sound*/
double tau ;    /*rising edge*/
double n_exc ;  /*real index of refraction for the excitation beams*/
double k_exc ;  /*imaginary index of refraction for the excitation beams*/
double n_p ; /*real index of refraction for the probe beams*/
double k_p ; /*imaginary index of refraction for the probe beams*/
double lambda_exc ;  /*wavelength in vacuum*/
double lambda_p ;  /*wavelength in vacuum*/
double delr ;   /*x spacing used in the integrator trap*/
double fs ;
int npts ;      /* the number of points in the integrator*/
int skip_npts ; /*number of data points to skip in calculating the fit and residual*/
double acoustic_amp ; /*acoustic component of signal as a fraction*/
double xmax ;
double mint ;
double maxt ;
} ;
double Re_Ar ;  /*real part of the reflection coefficient*/
double Im_Ar ;  /*Im part of the reflection coefficient*/
double *Re_intg_refl ;
double *Im_intg_refl ;
double *calc_sin ;
double *calc_cos ;
double *calc_exp ;
```

```
/* fitting parameters and step sizes */
struct fit_par
{
 int npar ;
 double par[9], step[9], orig_step[9], min_ratio[9] ;
} f_par ;
struct data
{
 int npts ;
 double *t, *y ;
} data, fit, res ;
```

END

DATE FILMED

8/31/92